Studies on electrorefining and electroreduction processes for nuclear fuels in molten chloride systems

2010

Masatoshi Iizuka

Contents

Chapter 1 Introduction

1.1 Metallic fuel cycle

Development of innovative nuclear fuel cycle technology is strongly required to serve for both the environmental sustainability and the increasing energy demand. Under a such circumstance, the metallic fuel cycle has been proposed. As shown in Fig. 1-1, the metallic fuel cycle is a combination of the metal fuel fast reactor, the pyrometallurgical reprocessing and the injection casting fuel fabrication. Because of its excellent advantages in economic, safety and proliferation resistance aspects [1], the metallic fuel cycle has been attracting increasing attention as one of the most promising options in the nuclear fuel cycle technologies for the next generation [2-5].

The schematic view of the metallic fast reactor fuel pin is shown in Fig. 1-2, compared with that of the oxide fast reactor fuel. The metallic fast reactor fuel is normally U-Zr binary or U-Pu-Zr ternary alloys that contains about 10 wt% of zirconium. The alloys casted into a rod-shape, which is called a fuel slug, are piled up to attain the required fuel length. Stainless steel is used as the cladding material as well as in the oxide fuel. Sodium bonding between the fuel slug and the cladding is adopted to improve the heat transfer to the coolant taking advantage of the fine compatibility between the fuel alloys and sodium. The metallic fuel alloys themselves have much higher thermal conductivities than the oxide fuel. These characteristics of the metallic fuel result in sufficiently low fuel temperature compared with their melting points, and give larger safety margin against the abnormal incidents such as transient overpower. Since the heavy metal density in the metallic fuel is higher than the other fuels, metal-fueled fast reactor core can be designed smaller than that with oxide fuels on the basis of the same generating power. It brings a significant economic advantage because this feature indicates that the metallic fast reactor generates smaller amount of spent fuel per electric output than other types of reactors.

Figure 1-3 shows the schematic view of the injection casting apparatus for metallic fuel fabrication and its operation procedure. The lower end of the bundle of quartz mold tubes is dipped into the fuel alloy melted under vacuum. Then the argon gas is quickly introduced in the apparatus to the atmospheric pressure, and the alloy is casted into the molds. The injection casting is a much simpler method than the pellet fabrication process for the oxide fuels. It has to be also noted that more than a hundred fuel slugs can be produced in a several hours operation. The simplicity and high throughput of the injection casting step greatly contribute to the large reduction on the fuel cycle cost. At Argonne National Laboratory (ANL) in U.S., five casting furnaces

have been operated to fabricate approximately17,000 binary and 1,000 ternary fuel slugs during about thirty years from the preparation of initial loading to EBR-II in 1962 to its termination in 1994 [6]. During this long-term experience, fabrication of over 30,000 recycled pins from the EBR-II irradiated fuels should specially mentioned from a viewpoint of its excellent suitability to the remote operation.

1.2 History of research and development on pyrometallurgical technologies

The studies on the nuclear fuel reprocessing in molten salt media were already initiated in 1950's [7]. The electrochemical winning/refining of the actinides and measurement of their fundamental properties in molten salt/liquid metal systems were also conducted widely in many countries [8-14]. The early EBR-II irradiated fuels were reprocessed in a simple metallurgical step called melt-refining method [15] that utilized the precipitation of the chemically active fission products in the melted irradiated fuel alloy by reaction with ZrO_2+CaO crucible. Development of the metallic fuel and pyrometallurgical processes in ANL once went into a decline since UO_2 was selected as the most favorable nuclear fuel material for the commercial use at that time. Those activities, however, revived along with the beginning of the Integral Fast Reactor (IFR) program [16]. The IFR is a system that consists of a fast reactor that uses metallic fuel and sodium cooling, coupled with a co-located pyrometallurgical spent fuel reprocessing, and with processes for preparing wastes for disposition. Although the IFR program was terminated in 1995, the research and development on the pyrometallurgical processes in U.S. are being continued in ANL and Idaho National Laboratory (INL). In INL, the conditioning of the EBR-II spent fuels for long-term disposition has been steadily progressed in a near-practical scale.

In Japan, the researches on the metallic fuel cycle was started in Central Research Institute of Electric Power Industry (CRIEPI) later in 1980's in parallel with that on the pyropartitioning of high level liquid waste generated in the PUREX process for the LWR fuels. These activities are presently conducted mainly in CRIEPI [3] and Japanese Atomic Energy Agency (JAEA). Recently, Korea [4] and India [5] have been accelerating the metallic fuel cycle technology development.

1.3 Pyrometallurgical reprocessing of metallic fast reactor fuel

A typical process flow sheet of the pyrometallurgiccal reprocessing for metallic fuel is shown in Fig. 1-4. The spent metallic fuel dismantled from the reactor is disassembled after an adequate cooling period. The irradiated fuel pins are mechanically chopped into 5 – 10 mm in length. Distillation for removal of the

bonding sodium and volatile fission products (cesium, iodine, etc.) would be done after the chopping at the option of the process design. The chopped fuel pins are then sent to the molten salt electrorefining step where the actinides are decontaminated from the fission products (FPs) and recovered. The cathode products taken out from the electrorefining apparatus are accompanied by the solvents (chlorides and cadmium metal). In the high temperature distillation step, called cathode processing, those solvents are distilled off, and the cathode products are consolidated into dense metal ingots at the same time. The products of the cathode processing step are adequately blended with other product and supplementary zirconium to make the fuel composition, and then sent to the injection casting step to fabricated the recycled fuel slug.

As described above, the main part of the pyrometallurgical reprocessing is very simple and the number of the required steps is much smaller than PUREX process. The restriction in the apparatus design from the viewpoint of criticality is milder since the pyrometallurgical processes do not use water, which is an excellent moderator of neutrons, as a solvent. The dimension of the process equipment per its capacity would be consequently smaller. The elimination of organic solvents that are more damageable by irradiation is also advantageous from the standpoint the process waste reduction. All these characteristics indicate the excellent economical potential of the pyrometallurgical reprocessing for remarkable reduction in the plant volume.

In the pyrometallurgical reprocessing, as shown below, plutonium is always recovered with uranium, minor actinides (neptunium, americium and curium) and a little amount of lanthanide FPs. These impurities impact neither the homogeneity of the fuel fabricated by the injection casting nor the performance of the fast reactor loaded with recycled fuel [17, 18]. Taking the lower accessibility and the difficulties in diversion due to the “dirtiness of products” into consideration, the low decontamination property of the pyrometallugical reprocessing could be an advantage from the viewpoint of proliferation resistance.

1.4 Electrorefining in molten salt electrolyte

The main step in the pyrometallurgical reprocessing for the metallic fuel is molten salt electrorefining, where most part of the actinide elements are recovered and decontaminated from the FPs. Fig. 1-5 shows a schematic flow of the normal operation of the electrorefining step. The chopped spent metallic fuel is loaded in a steel basket, and anodically dissolved in molten lithium chloride/potassium chloride (LiCl-KCl) eutectic mixture. The chemically active FPs such as alkali, alkaline earth, and rare earth metals exchange with the actinide chlorides in the electrolyte and accumulate in

the form of chlorides. The noble metal FPs are left in the anode basket because they are much less stable as chlorides than the actinide elements. Because zirconium, which is one of the constituents of the metallic fuel alloy, has the next higher electrode potential than uranium in the spent fuel [19, 20], its behavior sensitively depends on the conditions of anodic dissolution. Two kinds of cathodes are used to obtain different streams of products. One is a solid cathode made of iron for the blanket material production, and the other is a liquid cadmium cathode (LCC) for the driver fuel material production. At the solid cathode, uranium is selectively collected due to its higher standard electrode potential than those of other actinide elements [21]. In the LCC, on the other hand, the free energy changes of the actinide chlorides come close to each other because the transuranium elements are stabilized due to their very low activity coefficients in liquid cadmium [22, 23]. Therefore, plutonium is always collected at the LCC together with uranium and minor actinides. A small amount of lanthanide FPs also comes into the LCC product since their activities are lowered in liquid cadmium as well as those of transuraniums.

The basic behavior of major elements in the electrorefining step, such as electrode reactions of the actinides and separation performance of FPs, has been clarified. For example, the standard redox potentials of the actinide and lanthanide elements in LiCl-KCl, that principally determine the order of chloride formation among them, have been nearly completed [21]. The activity coefficients of those elements in liquid cadmium, that affect the their distribution between the molten salt and liquid cadmium, have been also measured [22, 23]. The distribution equilibrium among the actinide and lanthanide elements can be easily calculated using the separation factors [24, 25], that put the influence of the standard potentials and the activity coefficients together in a number specific to individual element. On contrast to the electrochemical and thermodynamic data, the kinetic data such as the diffusion coefficients in the molten salt and in liquid cadmium are not sufficient.

The fundamental feasibility of the electrorefining, such as the anodic dissolution of U-Zr alloy and the recovery of uranium [26] and recovery of plutonium into LCC [27], have been demonstrated. The current activities are mainly focused on the optimization of the operation conditions and engineering subjects, such as improvement of the processing rate and development of larger scale equipments applicable to practical use.

1.5 Electroreduction of oxide fuels

In order to link the metallic fuel cycle to the present LWR fuel cycle as shown

in Fig. 1-1, either the LWR spent fuels or the UO_2-PuO_2 mixed oxide (MOX) products from the PUREX fuel reprocessing must be reduced to metals. For this purpose, the electrochemical reduction method (Fig. 1-6) has been currently studied for reduction of oxide nuclear fuels. This method applies the innovative titanium production process [28] to the conversion of nuclear material. In this process, the oxides are immersed in molten LiCl electrolyte as a cathode and electrochemically reduced to metals. The oxygen ion generated at the cathode is anodically oxidized to evolve oxygen gas. When consumable carbon anode is used, carbon oxides are generated at the anode instead.

The electrochemical reduction process eliminates the troublesome handling of lithium metal required in the direct chemical reduction of the actinide oxides by addition of lithium metal [29, 30]. Another advantage of the electrochemical reduction is that the oxide ions produced at the cathode are simultaneously consumed at the anode. It means that the concentration of oxide ions in the electrolyte can be maintained at a desired low level, while it gradually accumulates in the lithium reduction process. This nature of the process is very favorable because low oxide ion concentration thermodynamically pushes the reaction towards complete reduction of the actinide elements. Since concentration of oxide ion in the electrolyte does not increase, the amount of the electrolyte and the volume of the equipment, in consequence, can be reduced.

The electrochemical reduction in molten $CaCl_2$ or LiCl has been investigated with UO_2 [31] and with MOX [32]. Although the complete reduction of these materials has been confirmed by scanning electron microscope (SEM) observation, the electrochemically optimum conditions for the reduction and the cause for decrease of plutonium concentration in the reduction product are not yet clear

1.6 Objectives of this thesis

As described above, the fundamental feasibility of the electrorefining and electroreduction processes, such as the recovery of the actinides at both the solid and liquid cadmium electrodes and conversion of UO_2 and MOX to metals, has been clarified. The basic electrochemical and thermodynamic data that govern the distribution equilibrium among the actinide and lanthanide elements in molten LiCl-KCl/liquid cadmium system have been obtained.

For advanced evaluation of those processes, the investigation on the process rate should be carried out using sufficient kinetic data like diffusion coefficients in the molten salt. To establish the engineering and practical feasibility based on the technical

and economical evaluation, it is also needed to understand the quantitative relation between the operation conditions and the important performance such as processing rate, recovery rate and decontamination factors. In addition, it is necessary to predict the process performance in the electrorefining step by developing proper models in order to design the practical equipments and process flow sheet with satisfactory accuracy and reliability.

On the backgrounds mentioned above, the following six studies are carried out in this thesis for quantitative understanding of the relation between the operation conditions and the performance of the electrorefining and electroreduction processes, and for reliable prediction of electrorefining behavior based on the fundamental data and experimental findings.

In chapter 2, diffusion coefficients of cerium and gadolinium in molten LiCl-KCl are determined using electrochemical method. The error in defining the surface area of the working electrode is minimized by improvement of the experimental device and by extension of the conventional electrochemical equation. Discussion is also carried out on the relationship between the diffusion property of the lanthanides in molten chloride and their ionic structures.

In chapter 3, electrochemical methods for recovery of actinides from molten LiCl-KCl/liquid metal system are investigated. The attainable performance and the optimal operating conditions are quantitatively discussed.

In chapter 4, behavior of plutonium and americium at liquid cadmium cathode in molten LiCl-KCl electrolyte is studied. The adequate condition for smooth recovery, such as plutonium concentration in the electrolyte and cathodic current density, is also discussed.

In chapter 5, anodic behavior of U-Zr or U-Pu-Zr alloys during electrorefining in molten LiCl-KCl is modeled taking account of recent findings. Validation of the model is carried out using the results of the previous electrorefining tests. Some exploratory calculations are also conducted to investigate the effect of the operating conditions on the anodic dissolution rate and zirconium dissolution ratio.

In chapter 6, applicability of two electroanalytical methods to on-line monitoring of actinide concentrations in molten LiCl-KCl is investigated using uranium, plutonium and neptunium for use in the pyrometallurgical processes.

In chapter 7, behavior of plutonium is quantitatively investigated by electrochemical reduction experiment in molten LiCl and $CaCl_2$ electrolytes using UO_2-PuO_2 mixed oxides (MOX). Favorable conditions for the electrochemical reduction of those materials are also discussed.

Finally in chapter 8, the conclusions of those studies are summarized.

References

[1] T. Inoue, T. Yokoo and T. Nishimura, “Assessment of advanced technologies for the future nuclear fuel cycle,” *Proc. Int. Conf. on Future Nuclear Systems (Global’99)*, Jackson Hole, WY, Aug. 29-Spt. 3, 1999.

[2] T. Koyama, Y. Sakamura, T. Ogata and H. Kobayashi, "Pyroprocess and metal fuel development for closing actinide fuel cycle with reduced waste burden", *Proc. GLOBAL 2009*, Paris, France, Sep. 8-11, 2009.

[3] T. A. Todd, L. K. Felker, J. D. Vienna, J. Bresee and S. Lesica, "The advanced fuel cycle initiative separations and waste campaign: Accomplishments and strategy", *ibid*.

[4] Hansoo Lee, Jin-Mok Hur, Do-Hee Ahn, In-Tae Kim and Jong-Hyun Lee", Development of pyroprocessing technology at KAERI", *ibid*.

[5] K. V. Govindan Kutty, P. R. Vasudeva Rao and Baldev Raj, "Current status of the development of the fast reactor fuel cycle in India", *ibid*.

[6] C. E. Stevenson, “The EBR-II Fuel Cycle Story”, Am. Nucl. Soc. (1987).

[7] Argonne National Laboraoty, “Reactor Fuel Processing – A Review of Recent Development”, V4(1)-V9(3), 1961-1966.

[8] Niedrach, Glamm, “Electrorefining for Removing Fission Products from Uranium Fuels”, *Ind. Eng. Chem.*, **48**, 977-981 (1956).

[9] D. Inman, G. J. Hills, L. Young and J. O'M. Bockris, “Electrode reactions in molten salts: the uranium + uranium trichloride system”, *Trans. Faraday Soc.* ,**55**, 1904-1914 (1959).

[10] D. L. Hill, J. Perano and R. A. Osteryoung, “An Electrochemical Study of Uranium in Fused Chlorides”, *J. Electrochem. Soc.*, **107**, 698-705 (1960).

[11] G. Chauvin, M. Coriou, P. Jabot and A. Laroche, “Production d'uranium de haute purete par electroraffinage en bains de sels fondus”, *J. Nucl. Mater.*, **11**, 183-192 (1964).

[12] O. V. Skiba, M. V. Smirnov and T. F. Khazemova, Electrochemistry of Molten and Solid Electrolytes, vol. 2, ed. M. Smirnov (Authorized Russian Translation, Consultants Bureau, New York, 1964), p.7-11.

[13] F. Caligara, I. Martinot and G. Duyckaerts, “Chronopotentiometric determination of U(III), U(IV), UO_2(VI) and Np(IV) in molten LiCl-KCl eutectic”, *J. Electroanal. Chem.*, **16**, 335-340 (1968).

[14] M. Kanno and S. Yamagami, “Electrochemical Behavior of U (III) and U (IV)

in Molten LiCl-KCl Eutectic", *Denki Kagaku*, **43**, 253-257 (1975), *in Japanese*.

[15] D. C. Hampson, R. M. Fryer, J. W. Rizzie, "Melt Refining of EBR II Fuel", *Nucl. Met.*, **15**, 57-76 (1969).

[16] Y.I.Chang, "Integral Fast Reactor", Nucl. Technol., 88, p.129(1989).

[17] M. Kurata, A, Sasahara, T. Inoue, M. Betti, J. Babelot, J. Spirlet and L. Koch, *Proc. of Int. Conf. on Future Nuclear Systems (Global '97)*, Yokohama, Japan, Oct. 5-10, 1997.

[18] T. Yokoo, T. Ogata and K. Ohta, "A design study on the FBR metal fuel and core for commercial applications", *J. Nucl. Sci. Technol.*, **37**, 636-645 (2000).

[19] T. Suzuki, "Equilibrium Between Zirconium and Its Chlorides in LiCl-KCl Eutectic Melt", *Denki Kagaku*, **39**, 864-867 (1971).

[20] R. Baboian, D. L. Hill and R. A. Bailey, "Electrochemical studies on zirconium and hafnium in molten LiCl-KCl eutectic", *J. Electrochem. Soc.*, **112**, 1221-1224 (1965).

[21] J. Roy, L. Grantham, D. Grimmett, S. Fusselman, C. Krueger, T. Storvick, T. Inoue, Y. Sakamura and N. Takahashi, "Thermodynamic properties of U, Np, Pu, and Am in molten LiCl-KCl eutectic and liquid cadmium", *J. Electrochem. Soc.*, **143**, 2487-2492 (1996).

[22] I. Johnson, M. G. Chasanov and R. M. Yonco, "Pu-Cd system : Thermodynamics and partial phase diagram", *Trans. Metallurg. Soc. AIME*, **233**, 1408-1414 (1965).

[23] Y.Sakamura, T.Inoue, T.S.Storvick and L.F.Grantham, *Proc. Global '95*, Verseilles, France, Sep. 11-14, 1995

[24] M. Kurata, Y. Sakamura, T. Hijikata and K. Kinoshita, "Distribution behavior of uranium, neptunium, rare-earth elements (Y, La, Ce, Nd, Sm, Eu, Gd) and alkaline-earth metals (Sr, Ba) between molten LiCl-KCI eutectic salt and liquid cadmium or bismuth", *J. Nucl. Mater.*, **227**, 110-121 (1995)

[25] T. Koyama, T. R. Johnson, D. F. Fischer, "Distribution of Actinides between Molten Salt/Cadmium Metal Systems", *J. Alloys and Compounds*, **189**, 37-44 (1993).

[26] T. Koyama, M. Iizuka, Y. Shoji, R. Fujita, H. Tanaka, T. Kobayashi, M. Tokiwai, "An experimental study of molten salt electrorefining of uranium using solid iron cathode and liquid cadmium cathode for development of pyrometallurgical reprocessing," *J. Nucl. Sci. Technol.*, **34**, 384–393 (1997).

[27] Annual Technical Report for 1993, Chemical Technology Division, Argonne

National Laboratory Report ANL-94/15 (1994), p. 89.

[28] G. Z. Chen, D. J. Fray and T. W. Farthing, "Direct electrochemical reduction of titanium dioxide to titanium in molten calcium chloride", *Nature*, **407**, 361-364 (2000).

[29] T. Usami, M. Kurata, T. Inoue, H. E. Sims, S. A. Beetham and J. A. Jenkins, "Pyrochemical reduction of uranium dioxide and plutonium dioxide by lithium metal," *J. Nucl. Mater.*, **300**, 15-26 (2002).

[30] T. Usami, T. Kato, M. Kurata, T. Inoue, H. E. Sims, S. A. Beetham and J. A. Jenkins, "Lithium reduction of americium dioxide to generate americium metal," *J. Nucl., Mater.*, **304**, 50-55 (2002).

[31] Y. Sakamura, M. Kurata and T. Inoue, "Electrochemical Reduction of UO_2 in Molten $CaCl_2$ or LiCl," *J. Electrochem. Soc.*, **153**, D31-D39 (2006).

[32] M. Kurata, T. Inoue, J. Serp, M. Ougier and J. P. Glatz, "Electro-chemical reduction of MOX in LiCl," *J. Nucl. Mater.*, **328**, 97-102 (2004).

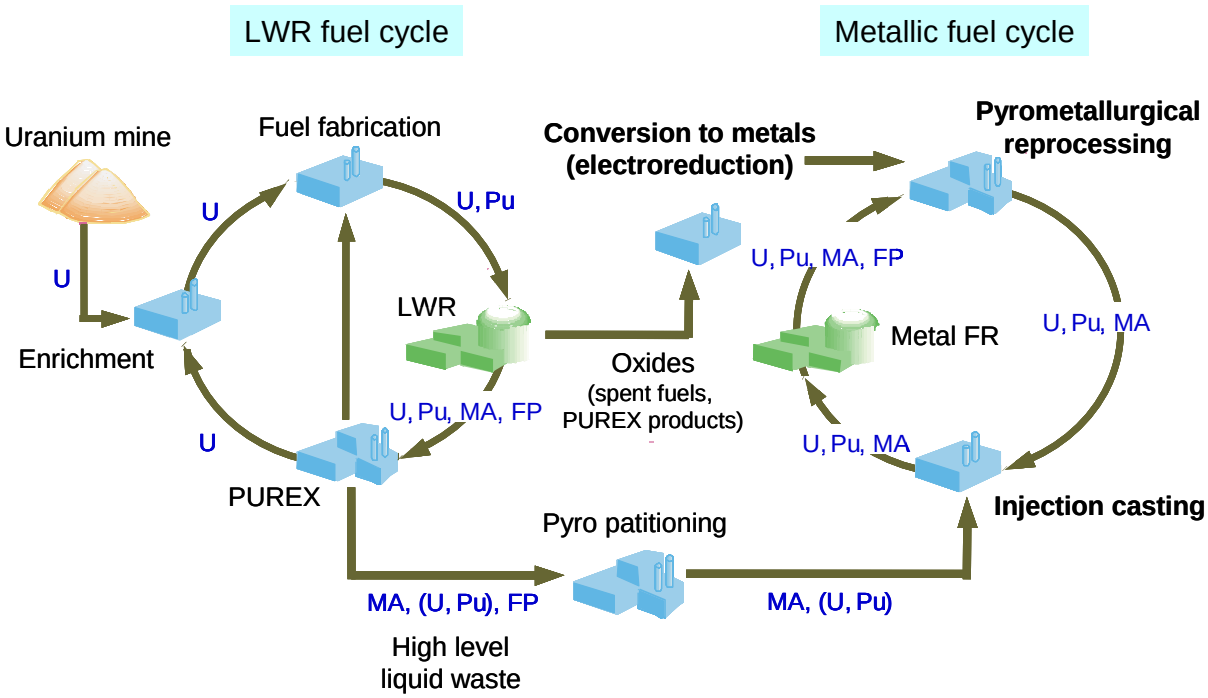

Fig. 1-1 Concept of metallic fuel cycle

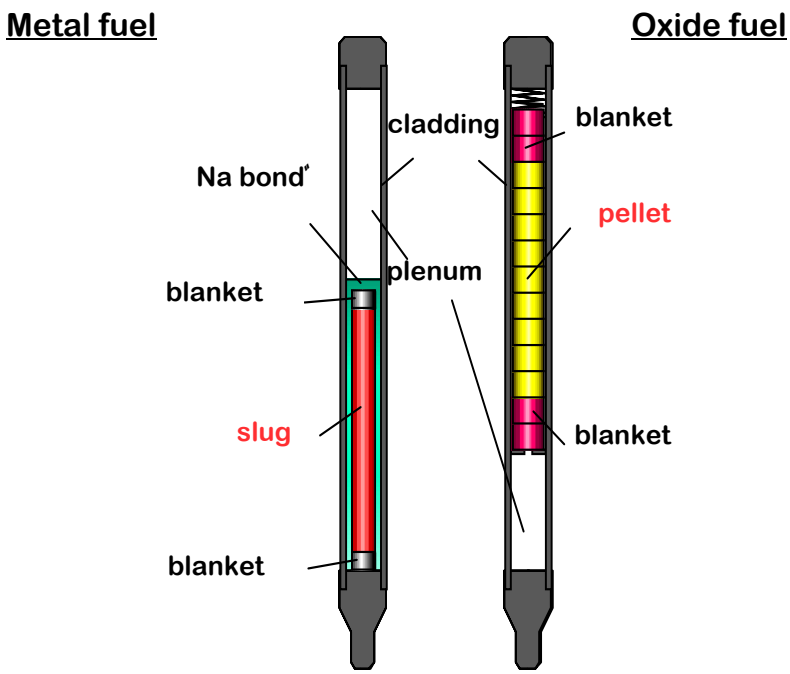

Fig. 1-2 Concept of Meta fuel

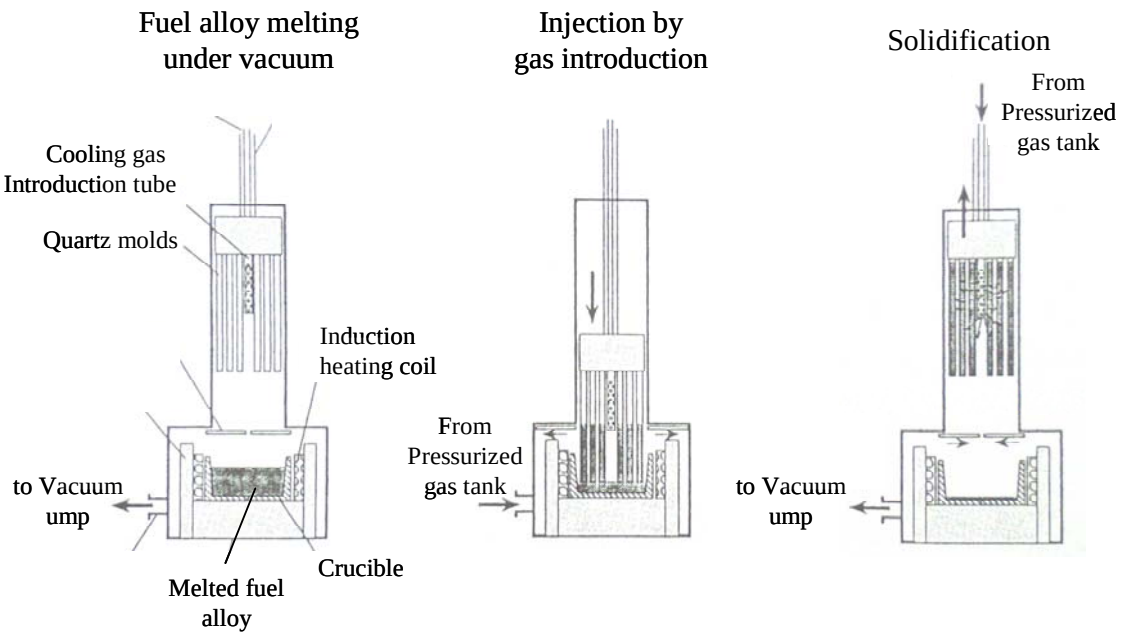

Fig. 1-3 Schematic view of injection casting furnace and operation procedure

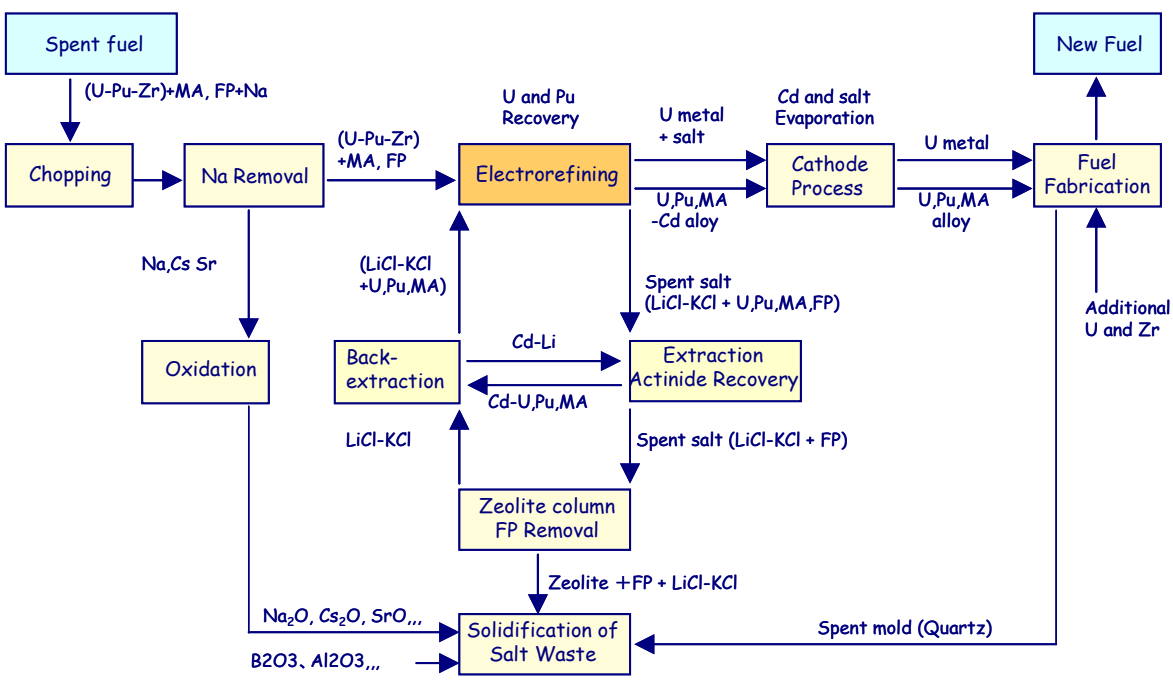

Fig. 1-4 Process flow sheet of pyrometallurgical reprocessing for metallic fuel

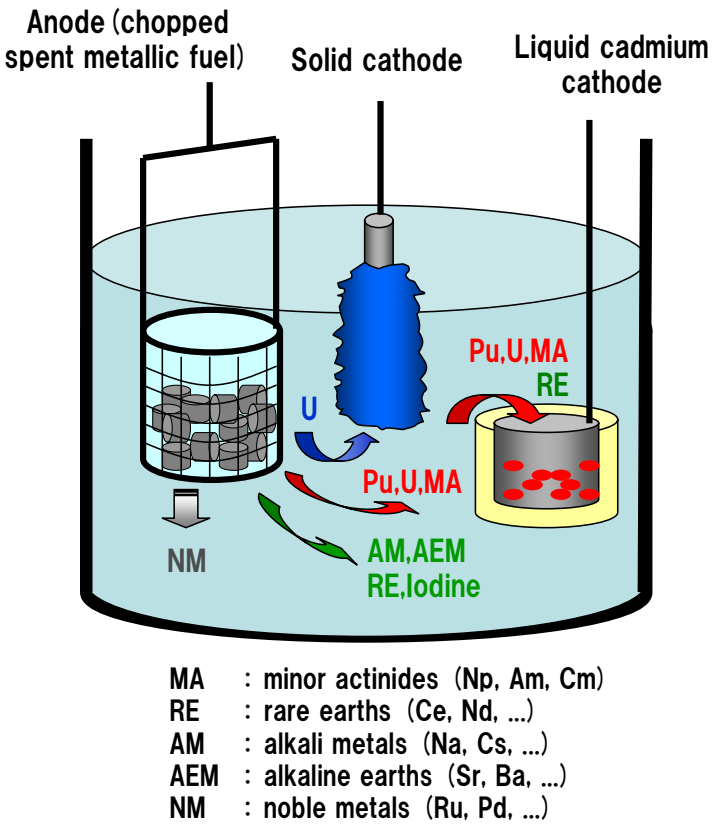

Fig. 1-5 Schematic flow of normal operation of electrorefining step

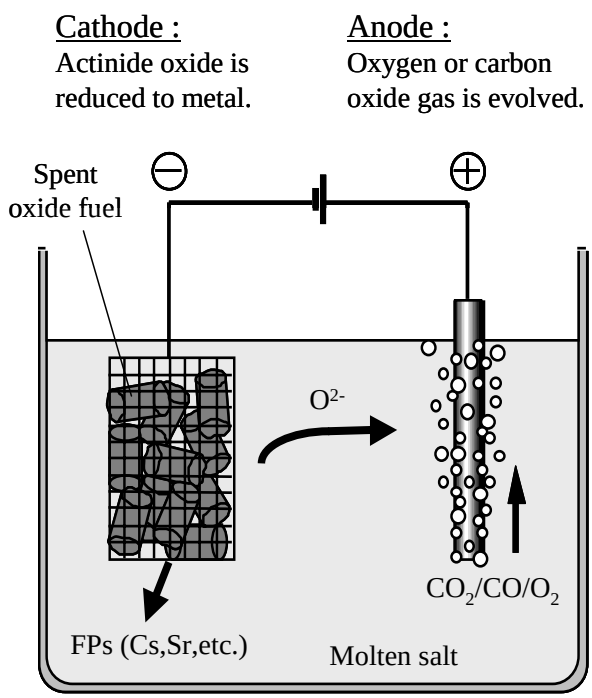

Fig. 1-6 Schematic flow of electroreduction step

Chapter 2 Diffusion coefficients of cerium and gadolinium in molten LiCl-KCl

2.1 Background and objectives

As described in Chapter 1, the most important step in the pyrometallurgical reprocessing is the electrorefining in molten chlorides [1, 2]. In this step, spent metal fuel is anodically dissolved into LiCl-KCl eutectic melt and the actinides are selectively recovered at the cathodes due to the differences among the redox potentials of the elements, while fission products remain in the anode and in the electrolyte salt. The principles of the electrorefining step have already been demonstrated [3, 4, 5] and major thermodynamic data have also been collected [6, 7, 8].

In order to maximize the processing rate of the electrorefining step, it is necessary to analyze and predict kinetic behavior of the elements in the electrorefiner. For this purpose, we have developed an electrorefining simulation code based on the diffusion layer model at the interface between the electrodes and the molten salt electrolytes [9]. Diffusion data of various elements in spent metal fuel are needed to simulate material transport precisely by this code. For the actinide elements, diffusion coefficients in LiCl-KCl have been reported [10-22]. However, there are few data for lanthanide elements [23, 24] which are the most difficult fission product elements to separate from actinides due to their similar chemical properties.

In this chapter, diffusion coefficients of cerium and gadolinium tri-valent ions were determined by chronopotentiometry in LiCl-KCl in the temperature range between 673 and 823 K.

2.2 Theoretical treatment

In conventional chronopotentiometric studies, diffusion coefficients have been determined from the Sand equation [25] :

$$\frac{i\tau^{1/2}}{C} = \frac{nFAD^{1/2}\pi^{1/2}}{2} \qquad (2\text{-}1)$$

where

i	:	current passed through the working electrode (A)
τ	:	transition time (s)
C	:	bulk concentration of the reactant (mol/cm^3)
n	:	number of the electrons involved in the reaction
F	:	Faraday constant (C/equiv.)

A : surface area of the working electrode (cm^2)

D : diffusion coefficient of the reactant (cm^2/s)

In this method, it is always difficult to define the surface area of the working electrode exactly in the molten salt due to (i) wetting between the electrode and the salt, and (ii) lack of suitable insulator materials which have a enough thermal strength and comparable thermal expansion coefficients with the electrode materials [26]. When lanthanides are reduced to their metals at the electrode, it becomes more difficult to use insulator material due to the chemical reactions between the lanthanide metals and the insulator. In this study, a method was devised to minimize the error in defining the effective surface area of the working electrode without any insulator material in the molten salt.

When the concentration of a reactant in a solution, the current passed through the working electrode, and the temperature of the system are kept constant, the transition time should be a function of the surface area of the working electrode alone.

$$\tau^{1/2} = f(A) = \frac{nFCD^{1/2}\pi^{1/2}}{2i} \cdot A \qquad (2\text{-}2)$$

Under such conditions, the change of the square root of the transition time is proportional to the change of the surface area of the working electrode.

$$d\tau^{1/2} = \frac{nFCD^{1/2}\pi^{1/2}}{2i} \cdot dA \qquad (2\text{-}3)$$

Then, the diffusion coefficient can be determined from the slope of $\tau^{1/2}$-A plot obtained by changing the surface area of the working electrode in an adequate way, even if the absolute value of the surface area can not be defined.

$$D^{1/2} = \frac{2i}{nFC\pi^{1/2}}\left(\frac{d\tau^{1/2}}{dA}\right) \qquad (2\text{-}4)$$

2.3 Experimental

2.3.1 Apparatus

All the measurements were carried out in a high purity argon atmosphere

glove box. Oxygen and moisture in the atmosphere were kept lower than 1 ppm during the experiments. Fig. 2-1 shows the schematic view of the experimental apparatus. The primary and secondary crucibles were made of high purity (> 99.9 %) alumina and steel, respectively. They were positioned in the steel outer vessel and heated with the electric furnace. The measurements were made at 673 to 823 K and the temperature was kept within ± 1 K by a PID controller.

2.3.2 Electrodes

A tungsten rod of 4 mm in diameter was used as the working electrode. The surface of the rod was polished with #2000 emery paper. Then it was washed in diluted nitric acid and in distilled water with an ultrasonic cleaner. The washed rod was attached at the end of a steel extension rod and immersed into the molten salt. The length of the immersed portion of the working electrode was adjusted with spacers of various sizes attached to a fixture on the lid of the reaction vessel. The smallest surface area made with the longest spacer was taken as the zero point, and relative change in the surface area was calculated from the length of the spacers. After each measurement, the potential of the working electrode was kept at about 100 to 200 mV higher than the initial value for 10 to 30 minutes to remove the lanthanide metal deposit from the surface of the electrode. A small piece of the lanthanide metal under measurement was used as the counter electrode to keep the composition of the electrolyte constant throughout the experiment. A silver / silver chloride (1 wt% in LiCl-KCl) electrode contained in a thin Pyrex tube was used as a reference electrode. The potential difference between the lanthanide metal counter electrodes and the Ag/AgCl reference electrode was recorded before each measurement. This value was very stable throughout the experiments at the constant temperature and the constant concentration of the lanthanides in the molten salt, indicating that the Ag/AgCl reference electrode was enough stable in the temperature range between 673 and 823 K.

2.3.3 Chemicals

The chlorides (LiCl-KCl, $CeCl_3$ and $GdCl_3$) used in this study were purchased from Anderson Physics Laboratory. Their purity was more than 99.99 % and content of moisture was extremely low. Rare earth metals (Ce and Gd) were of high purity (> 99.9 %) and thin films of their oxides on the surface were scratched off in the glove box. Other metals (W, Ta and Ag) were also of high purity (> 99.95 %). They were polished and cleaned in diluted nitric acid before use.

2.3.4 Analytical procedures

Princeton Applied Research EG&G potentio / galvanostat model 273A and EG&G 270/250 Research Electrochemistry Software 4.00 were used in the electrochemical measurement. The transition time was determined from the intersections of the three lines tangent to the plateau and potential-jump portions before and after the plateau in the chronopotentiograms. Concentration of the lanthanide elements in the molten salt was determined by chemical analysis (ICP-AES) of the samples taken at each temperature. Standard error in the results of the chemical analysis was lower than 1 %. Change in the density of the solvent [26] was taken into consideration in calculation of the concentrations.

2.3.5 Determination of the current for the measurements

The equation (2-1) can be applied to semi-infinite linear diffusion. The mass transport towards the working electrode must be diffusion- controlled, and any convective movement has to be excluded. Linearity between square root of the transition time and the reciprocal of the current passed through the electrode is a good indicator for satisfaction of those conditions. Fig. 2-2 shows the relationship between these two quantities obtained for LiCl-KCl-$CeCl_3$ solutions at various temperatures. Fine proportional relation can be observed between $\tau^{1/2}$ and $1/i$ at higher current (or shorter transition time), which indicates that the mass transport of cerium around the working electrode was simply controlled by linear diffusion. At lower current (or longer period), however, the transition time showed upper deviation from the above relation. This deviation indicates that cylindrical diffusion or convection of cerium must be taken into consideration. Too short measurement times should also be avoided to minimize the charging effect. From these results and considerations, the current in all the measurements was adjusted so that consequent transition times would be about 0.3 to 1 second.

2.4 Results

Fig. 2-3 shows typical chronopotentiograms obtained for LiCl-KCl-$CeCl_3$ changing the height of the spacers for the working electrode. The plateau corresponding to reduction of Ce(III) and potential-jump portions before and after the plateau can be clearly defined. The transition time became shorter with decreasing the surface area of the working electrode by raising it with longer spacers. Such relations at various temperatures are plotted in Fig. 2-4(a) to 2-4(d). Square root of the transition time changed linearly to the change in the surface area of the working electrode at all

the temperatures. This result indicates that the Eq. 2-3 certainly applies under these conditions.

Diffusion coefficient of Ce(III) was calculated from the slopes in Fig. 2-4 by Eq. 2-4. This calculation was carried out only for the plots with standard error of less than 3 %. Results are shown in Table 2-1 together with other experimental conditions.

These diffusion coefficients showed a good linearity in the arrhenius plot (Fig. 2-5). Finally, the diffusion coefficient of Ce(III) in LiCl-KCl was formulated as follows :

$$\log D_{Ce} = -2.69\,(\pm 0.145) - \frac{1670\,(\pm 108)}{T} \qquad (D_{\mathrm{Ce}} : \mathrm{cm}^2/\mathrm{s}) \qquad (2\text{-}5)$$

Similar results were obtained for diffusion of Gd(III) in LiCl-KCl. (Table 2-2 and Fig. 2-6). The diffusion coefficient of Gd(III) was formulated as follows :

$$\log D_{Gd} = -2.78\,(\pm 0.128) - \frac{1670\,(\pm 94.3)}{T} \qquad (D_{\mathrm{Gd}} : \mathrm{cm}^2/\mathrm{s}) \qquad (2\text{-}6)$$

2.5 Discussion

2.5.1 The surface area of the working electrode

In previous studies, the surface area of the working electrode has been defined from geometric structure by embedment in glasses [12, 28-30], by calibration in aqueous solution containing species whose diffusion coefficient had already been known [18], or simply by observation of immersed area of the working electrode [31]. These methods possibly cause errors which come from the creep of molten salt into the small gap between the electrode material and the glasses or from differences in wetting behavior in various solvents and at various temperatures.

The working electrode used in this study was a tungsten rod simply immersed into the molten salt, and insulator material which can cause error in defining surface area was not used. The effect of the wetting between the electrode material and the molten salt can not be neglected in any case. But this effect was canceled by comparing the transition time at various immersion depths of the working electrode in the same salt and at the same temperature. The fine linearity in the $\tau^{1/2}$-A plots (Fig. 2-4) shows that the surface area of the working electrode (to be exactly, the change in the surface area) defined in this method was highly accurate and reliable.

2.5.2 Concentration dependence of the diffusion coefficient

The concentration of lanthanides in the molten salt could not be varied very much in this study : 1.3×10^{-5} to 5.1×10^{-5} mol/cm^3 for Ce(III) and 1.0×10^{-5} to 6.3×10^{-5} mol/cm^3 for Gd(III), respectively. The transition time could not be defined accurately in the chronopotentiograms at lower concentrations, and the current became too large to keep consequent transition times within the range mentioned previously at higher concentrations. No concentration dependence was observed in the diffusion behavior of Ce(III) and Gd(III) within the concentration range in this study.

2.5.3 Diffusion behavior in LiCl-KCl and stability of complex ions

Activation energies, ΔH, for diffusion of both Ce(III) and Gd(III), which is calculated from the equation

$$-\frac{\Delta H}{2.3R} = \frac{\partial \log D}{\partial (1/T)} \qquad (2\text{-}7)$$

were 1.8 kJ/mol and independent of the temperature. This value is in good agreement with those for La(III) and Ce(III) obtained by Smirnov [23] and Sokolovskii [24] (Table 2-3). Fig. 2-7 shows the diffusion coefficients of tri-valent lanthanide ions in LiCl-KCl determined in this study together with the data by Smirnov [23] and Sokolovskii [24]. Although there is some discrepancy between D_{Ce}(III) measured by Sokolovskii and D_{Ce}(III) measured in this study, the diffusion coefficients of lanthanides seem to decrease with a decrease of their ionic radii. From these results, it is expected that the interdiffusion in LiCl-KCl eutectic melt largely depends on the characteristics of the diffusing cations, probably the coulombic interaction between the cations and surrounding anions, or stability of the complex ions. Sokolovskii [24] showed linear relations between the diffusion coefficients and ionic potentials of various ions in LiCl-KCl and in NaCl-KCl. The dependence of the diffusion coefficients on ionic radii for the lanthanide ions found in this study is qualitatively identical to Sokolovskii's result.

Inman [30] obtained even better linear correlations between the diffusion coefficients and ionization energies of gaseous metal cations from the viewpoint of redistribution of charge around the cations caused by formation of complex ions. The lanthanide tri-valent ions in LiCl-KCl are expected to exist in a form of octahedral complex ions MCl_6^{3-}. Stability of these complex ions, or bonding between the central

metal cations and chlorine ions, is supposed to be higher according to the decrease in the radii of the central cations, resulting in restraint of the diffusion process of the lanthanide ions. This relation between ionic radii of the lanthanide ions and the stability of their complex ions can also be expected from the thermodynamic data. Table 2-4 shows the activity coefficients of some lanthanide chlorides in LiCl-KCl at 723 K obtained by emf measurements [32]. It can be seen that the smaller the ionic radii the lower the activity coefficients, except for praseodymium, indicating the formation of more stable complex ions.

For more quantitative discussions, diffusion data for other lanthanides and computational studies for the structure and the transport processes in molten salts will be needed.

2.6 Conclusions

The diffusion coefficients of Ce(III) and Gd(III) in lithium chloride-potassium chloride eutectic melt were determined in the temperature range between 673 and 823 K by chronopotentiometry. In order to minimize the error in defining the surface area of the working electrode, the slope of the $\tau^{1/2}$-A plot was substituted into the Sand equation instead of their absolute values. The diffusion coefficients with the temperature dependence were :

$$\log D_{Ce} = -2.69(\pm 0.145) - \frac{1670(\pm 108)}{T} \qquad (D_{\mathrm{Ce}} : \mathrm{cm^2/s})$$

$$\log D_{Gd} = -2.78(\pm 0.128) - \frac{1670(\pm 94.3)}{T} \qquad (D_{\mathrm{Gd}} : \mathrm{cm^2/s})$$

The activation energies for diffusion and the diffusion coefficients of lanthanide ions in LiCl-KCl were discussed in connection with their ionic radii and stability of their complex ions.

References

[1] T. Koyama, R. Fujita, M. Iizuka, and Y. Sumida, “Pyrometallurgical reprocessing of fast reactor metallic fuel — development of a new electrorefiner with a ceramic partition”, *Nucl. Tech.*, **110**, 357-368 (1995).

[2] M. J. Lineberry and H. F. McFarlane, *Proc. Global '95*, Verseilles, France, Sep. 11-14, 1995

[3] T. Koyama, M. Iizuka, H. Tanaka, M. Tokiwai, Y. Shoji, R. Fujita, and T. Kobayashi, “An experimental study of molten salt electrorefining of uranium using solid iron cathode and liquid cadmium cathode for development of

pyrometallurgical reprocessing", *J. Nucl. Sci. Technol.*, **34**, 384-393 (1997).

[4] T. Koyama, M. Iizuka, N. Kondo, R. Fujita, and H. Tanaka, "Electrodeposition of uranium in stirred liquid cadmium cathode", *J. Nucl. Mater.*, **247**, 227-231 (1997).

[5] M. Iizuka, T. Koyama, N. Kondo, R. Fujita, and H. Tanaka, "Actinides recovery from molten salt/liquid metal system by electrochemical methods", *J. Nucl. Mater.*, **247**, 183-190 (1997).

[6] M. Sakata, M. Kurata, T. Hijikata, and T. Inoue, "Equilibrium distribution of rare earth elements between molten KCl-LiCl eutectic salt and liquid cadmium", *J. Nucl. Mater.*, **185**, 56-65 (1991).

[7] C. L. Kruger, T. S. Storvick, J. J. Roy, L. F. Grantham, L. R. McCoy, T. Inoue, H. Miyashiro, and N. Takahashi, "Measurement of the Standard Potential of the Np(III)/Np(0) Couple in LiCl-KCl Eutectic", *J. Electrochem. Soc.*, **138**, 1186-1187 (1991).

[8] Koyama, T. R. Johnson, D. F. Fischer, "Distribution of Actinides between Molten Salt/Cadmium Metal Systems", *J. Alloys and Compounds*, **189**, 37-44 (1993).

[9] T. Kobayashi and M. Tokiwai, "Development of trail, a simulation code for the molten salt electrorefining of spent nuclear fuel", *J. Alloys and Compounds*, **197**, 7-16 (1993).

[10] C. E. Thalmayer, S. Bruckenstein, and D.M.Gruen, "Chronopotentiometric determination of interdiffusion coefficients and heats of interdiffusion in molten salts", *J. Inorg. Nucl. Chem.*, **26**, 347-352 (1964).

[11] D. Nissen, "Electrochemistry of plutonium (III) in molten alkali chlorides", *J. Inorg. Nucl. Chem.*, **28**, 1740-1743 (1966).

[12] L. Martinot and G. Duyckaerts, "Electrochemistry of Pu(III) in Molten LiCl-KCl Eutectic", *Anal. Lett.*, **4**, 1-11 (1971).

[13] L. Martinot, J. C. Spirlet, G. Duyckaerts, and W. Muller, "Chronopotentiometric study of the reaction Am (III) + 3e → Am(0) in molten LiCl-KCl eutectic", *Anal. Lett.*, **6**, 321-326 (1973).

[14] L. Martinot, J. Reul, and G. Duyckaerts, "Chronopotentiometric study of the reduction of trivalent curium in molten (Li-K)Cl eutectic", *Anal. Lett.*, **8**, 233-239 (1975).

[15] P. Masset, D. Bottomley, R. Konings, R. Malmbeck, A. Rodrigues, J. Serp and J-P. Glatz, "Electrochemistry of uranium in molten LiCl-KCl eutectic", J. Electrochem. Soc., 152, A1109-1115 (2005).

[16] B. P. Reddy, S. Vandarkuzhali, P. Venkatesh, “Electrochemical studies on the redox mechanism of uranium chloride in molten LiCl-KCl eutectic”, *Electrochim. Acta*, **49**, 2471-2478 (2004).

[17] S. A. Kuznetsov, H. Hayashi, K. Minato and M. Gaune-Escard, "Electrochemical transient techniques for determination of uranium and rare-earth metal separation coefficients in molten salts", Electrochim. Acta, 51, 2463-2470 (2006).

[18] J. Serp, R. Konings, R. Malmbeck, C. Sheppler and J-P. Glatz, “Electrochemical behaviour of plutonium ion in LiCl-KCl eutectic melts”, *J. Electroanal. Chem.*, **561**, 143-148 (2004).

[19] J. Serp, P. Chamelot, S. Fourcaudot, R. Konings, R. Malmbeck, C. Pernal, J. C. Poignet, J. Rebizant and J-P. Glatz, “Electrochemical behaviour of americium ions in LiCl–KCl eutectic melt”, *Electrochim. Acta*, **51**, 4024-4032 (2006).

[20] O. Shirai, M. Iizuka, T. Iwai and Y. Arai, “Electrode reaction of the Np^{3+}/Np couple in LiCl-KCl eutectic melts”, *J. Appl. Electrochem,* **31**, 1055-1060 (2001).

[21] G. de Cordoba, A. Laplace, J. Lacquement, C. Caravaca, “Electrochemical behavior of Np in the molten LiCl-KCl eutectic”, *J. Electrochem. Soc.*, **154**, F16-F24 (2007).

[22] L. Martinot, G. Duyckaerts, “Chronopotentiometric measurements were used to study the diffusion of U^{3+} in molten eutectic mixtures”, *Anal. Lett.*, **1**, 669-678 (1968).

[23] M. V. Smirnov, Yu. N. Krasnov, V. E. Komarov, and V. N. Alekseev, "Diffusion coefficients of trivalent lanthanum in molten LiCl-KCl and LiCl-KCl+LiF mixtures", Trans. of the Inst. of Electrochem. Urals Academy of Sciences (Engl. Transl.), Vol. 6, 47 (1968).

[24] Yu. S. Sokolovskii, M. V. Smirnov, and O. V. Skiba, Tr. Inst. Elektrokhim., Akad. Nauk SSSR, Ural’sk. Filial, 5 : 41 (1964).

[25] H. J. S. Sand, Phil. Mag., **1**, 45 (1901).

[26] for example, F. Lantelme, D. Inman, and D. G. Lovering, in Molten Salt Techniques vol. 2, R. J. Gale and D. G. Lovering, p. 148, Plenum Press, New York (1984).

[27] G. J. Janz, “Thermodynamic and Transport Properties for Molten Salts : Correlation Equations for Critically Evaluated Density, Surface Tension, Electrical Conductance and Viscosity Data.”, Am. Chem. Soc. and Am. Inst. Phys. (1988).

[28] H. A. Laitinen and W. S. Ferguson, “Chronopotentiometric analysis in fused lithium chloride-potassium chloride”, *Anal. Chem.*, **29**, 4-9 (1957).

[29] S. Sternberg and C. Herdlicka, *Rev. Roumaine Chim.*, **14**, 991 (1969).

[30] D. Inman, Dj. Jovanovic, and S. H. White, “Interdiffusion coefficients in molten Li_2SO_4−K_2SO_4”, *J. Electroanal. Chem.*, **43**, 37-44 (1973).

[31] G. Mamantov and D. L. Manning, “Voltammetry and related studies of uranium in molten lithium fluoride-beryllium fluoride-zirconium fluoride”, *Anal. Chem.*, **38**, 1494-1498 (1966).

[32] D. Yamada, T. Murai, K. Moritani, T. Sasaki, I. Takagi, H. Moriyama, K. Kinoshita and H. Yamana, “Diffusion behavior of actinide and lanthanide elements in molten salt for reductive extraction”, *J. Alloys. Compounds*, **444-445**, 557-560 (2007).

[33] M. R. Bermejo, J. Gomez, J. Medina, A. M. Martinez and Y. Castrillejo, “The electrochemistry of gadolinium in the eutectic LiCl-KCl on W and Al electrodes”, *J. Electroanal. Chem.*, **588**, 253-266 (2006).

[34] Y. Castrillejo, M. R. Bermejo, A. I. Barrado, R. Pardo, E. Barrado and A. M. Martinez, “Electrochemical behavior of dysprosium in the eutectic LiCl-KCl at W and Al electrodes”, *Electrochim. Acta*, **50**, 2047-2057 (2005).

[35] Y. Castrillejo, M. R. Bermejo, R. Pardo and A. M. Martinez, “Use of electrochemical techniques for the study of solubilization processes of cerium-oxide compounds and recovery of the metal from molten chlorides”, *J. Electroanal. Chem*., **522**, 124-140 (2002).

[36] Y. Castrillejo, M. R. Bermejo, E. Barrado and A. M. Martinez, “Electrochemical behavior of erbium in the eutectic LiCl-KCl at W and Al electrodes”, *Electrochim. Acta*, **51**, 1941-1951 (2006).

[37] M. R. Bermejo, J. Gomez, A. M. Martinez, E. Barrado and Y. Castrillejo, “Electrochemistry of terbium in the eutectic LiCl-KCl”, *Electrochim. Acta*, **53**, 5106-5112 (2008).

[38] F. Lantelme, T. Cartailler, Y. Berghoute and M. Hamdani, “Pysicochemical properties of lanthanide and yttrium solutions in fused salts and alloy formation with nickel”, *J. Electrochem. Soc.*, **148**, C604-C613 (2001)

[39] C. Caravaca, G. de Cordoba M. J. Tomas and M. Rosado, “Electrochemical behavior of gadolinium ion in molten LiCl-KCl eutectic”, *J. Nucl. Mater.*, **360**, 25-31 (2007).

[40] G. Cordoba and C. Caravaca, “ An electrochemical study of samarium ions in the molten eutectice LiCl+KCl”, *J. Electroanal. Chem.*, **572**, 145-151 (2004).

[41] Y. Sakamura, T. Hijikata, T. S. Storvick, and L. F. Grantham, “Development of pyrometallurgical partitioning technology of long-lived nuclides”, CRIEPI report T93068 (1994), *in Japanese*

[42] R. D. Shanon, “Revised effective ionic radii and systematic studies of interatomic distances in halides and chalcogenides”, Acta Cryst., A32, 751-767 (1976).

.

Table 2-1 Slopes of $\tau^{1/2}$-A plots and experimental conditions (cerium)

T (K)	$10^5\ C_{Ce}$ (mol/cm^3)	i (A)	$d\tau^{1/2}/dA(\pm$S.E.) (s$^{1/2}$/cm^2)	$10^5\ D_{Ce}$ (cm^2/s)
675	2.98	0.070	0.263 ± 0.0189	—
724	2.59	0.085	0.214 ± 0.0147	—
773	2.38	0.100	0.203 ± 0.00930	—
824	2.80	0.120	0.241 ± 0.0125	—
673	1.33	0.030	0.223 ± 0.00982	—
698	1.34	0.035	0.286 ± 0.00971	0.853
723	1.35	0.030	0.327 ± 0.0217	—
773	1.34	0.040	0.275 ± 0.0112	—
823	1.36	0.040	0.394 ± 0.015	2.03
673	4.64	0.100	0.313 ± 0.00795	0.694
723	4.66	0.120	0.305 ± 0.00725	0.933
773	4.73	0.140	0.339 ± 0.0115	1.53
823	4.45	0.150	0.338 ± 0.00889	1.97
673	5.10	0.070	0.463 ± 0.0118	0.611
724	5.02	0.090	0.462 ± 0.0178	1.04
726	5.06	0.090	0.472 ± 0.00914	1.07
775	4.93	0.100	0.468 ± 0.0100	1.37
823	4.89	0.120	0.421 ± 0.0117	1.62

Table 2-2 Slopes of $\tau^{1/2}$-A plots and experimental conditions (gadolinium)

T (K)	$10^5\ C_{Gd}$ (mol/cm^3)	i (A)	$d\tau^{1/2}/dA(\pm$S.E.) (s$^{1/2}$/cm^2)	$10^5\ D_{Gd}$ (cm^2/s)
676	2.78	0.055	0.297 ± 0.00933	0.526
725	2.76	0.070	0.289 ± 0.00835	0.815
774	2.69	0.090	0.273 ± 0.00351	—
773	2.69	0.075	0.310 ± 0.0107	1.14
824	2.61	0.090	0.299 ± 0.0170	—
675	6.32	0.080	0.492 ± 0.00791	0.590
724	6.20	0.100	0.470 ± 0.00889	0.873
772	6.14	0.120	0.431 ± 0.0204	1.08
770	6.04	0.120	0.460 ± 0.00834	1.27
824	6.00	0.140	0.439 ± 0.00650	1.59
674	1.09	0.020	0.329 ± 0.00778	0.558
723	1.07	0.025	0.283 ± 0.0160	—
824	1.08	0.025	0.329 ± 0.00739	0.887
773	1.06	0.030	0.289 ± 0.00974	1.02
822	1.04	0.035	0.261 ± 0.00853	1.17

Table 2-3 Activation energy ΔH for various species in LiCl-KCl

Species	Temperature (K)	Δ H (kJ/mol)	Ref.
Ag(I)	647-1019	1.4±0.05	10
Cd(II)	668-1082	1.6±0.7	10
Pb(II)	654-1008	1.9±0.2	10
Bi(III)	637-930	2.3±0.2	10
U(IV)	693-894	1.85	10
Pu(III)	673-873	1.6	11
	698-898	2.0 - 2.70	12
La(III)	710-943	1.8	23
Ce(III)	673-824	1.8±0.1	This study
	673-923	1.8	24
Cd(III)	674-824	1.8±0.1	This study

Table 2-4 Activity coefficient of lanthanide chlorides in LiCl-KCl at 723 K

Chloride	Ionic radii [42] (Å)	Activity coefficient
$LaCl_3$	1.032	3.8×10^{-3}
$CeCl_3$	1.01	2.0×10^{-3}
$PrCl_3$	0.99	8.0×10^{-3}
$NdCl_3$	0.983	7.6×10^{-4}
$GdCl_3$	0.938	1.7×10^{-4}
YCl_3	0.900	2.4×10^{-6}

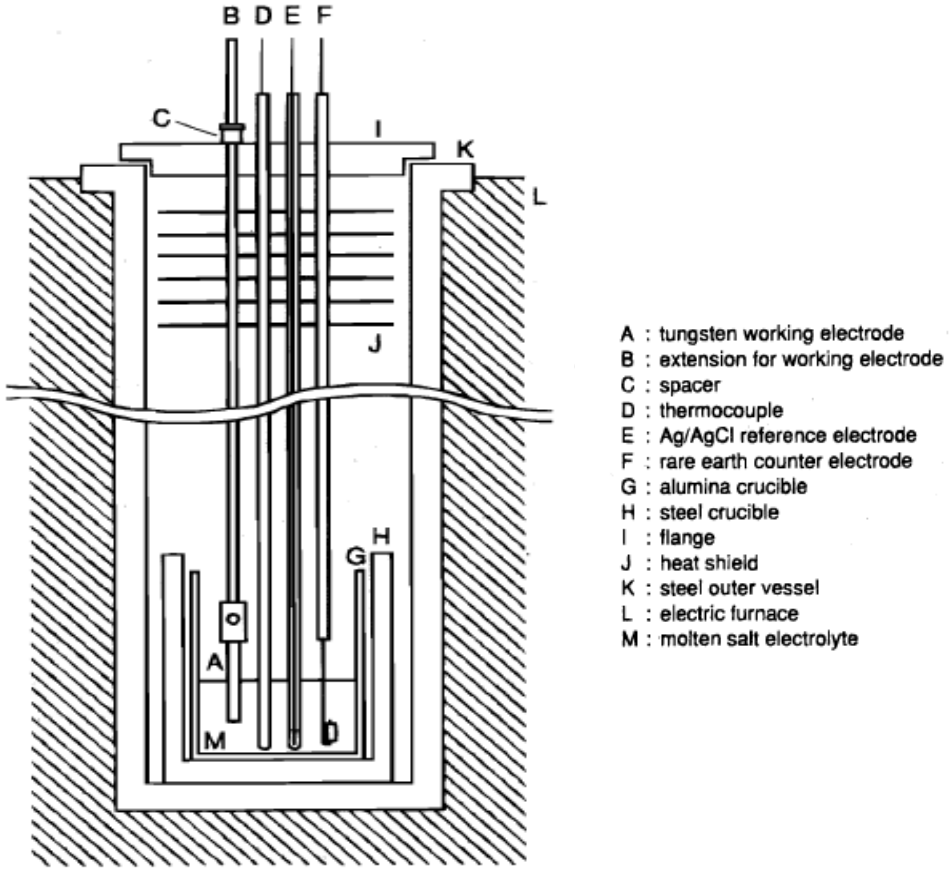

Fig. 2-1 Schematic view of experimental apparatus

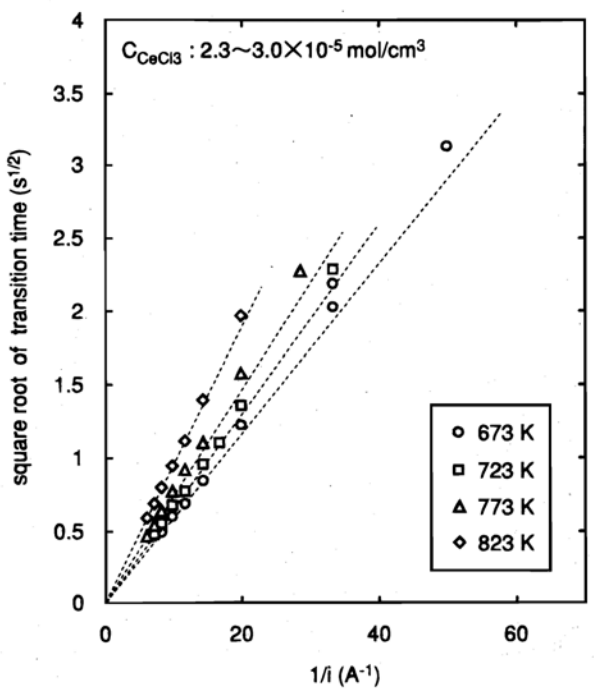

Fig. 2-2 Relation between square root of transition time and current in chronopotentiograms for LiCl-KCl-$CeCl_3$ solutions at various temperatures

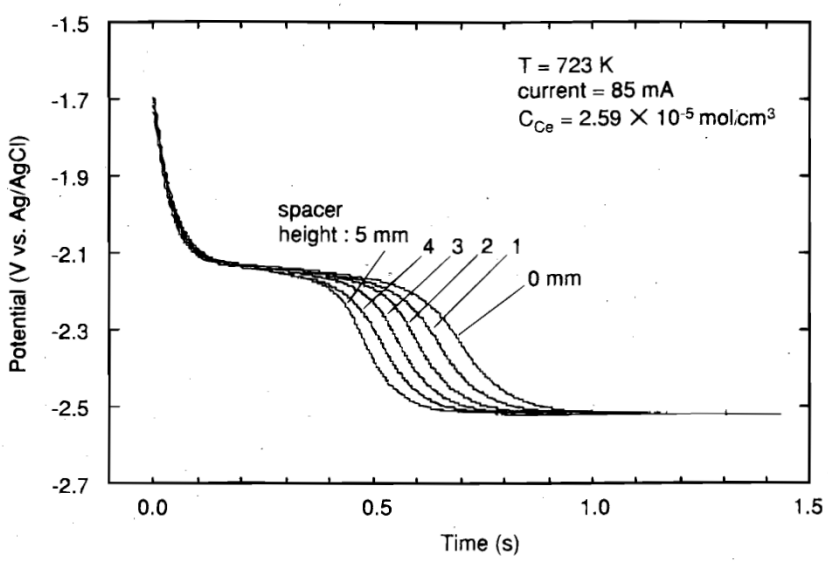

Fig. 2-3 Chronopotentiograms for LiCl-KCl-$CeCl_3$ solutions with various surace areas of working electrodes

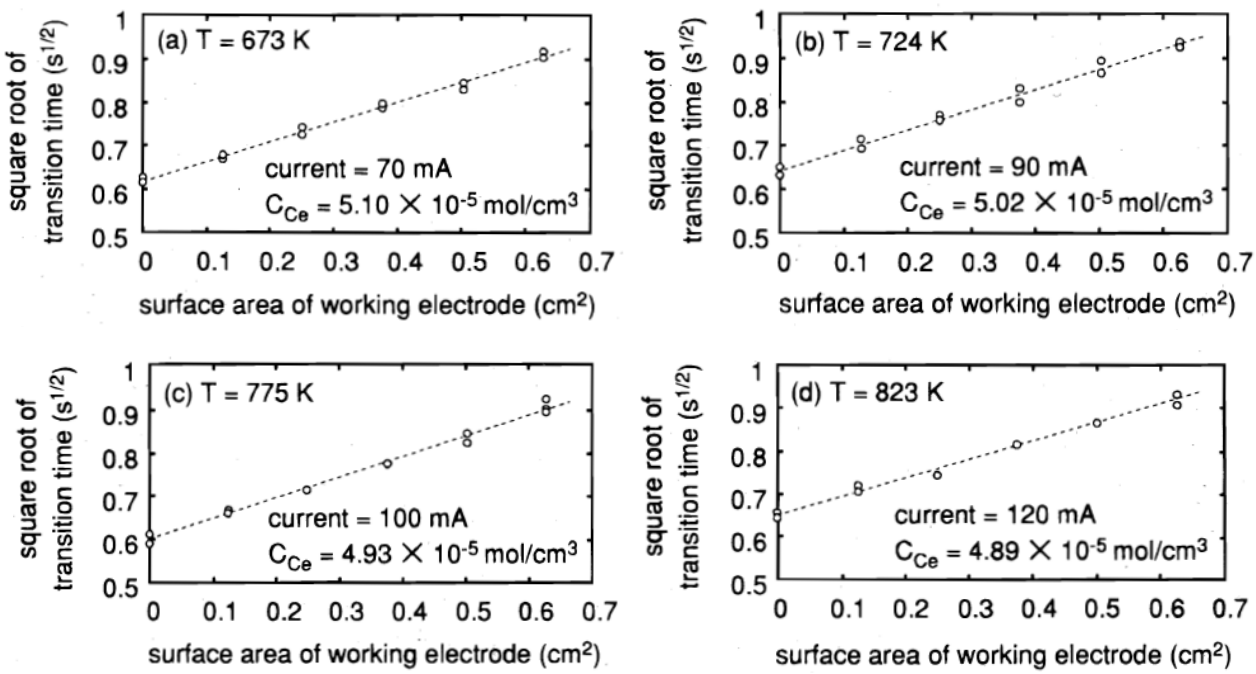

Fig. 2-4 Relation between square root of transition time and surface area of working electrode at various temperatures

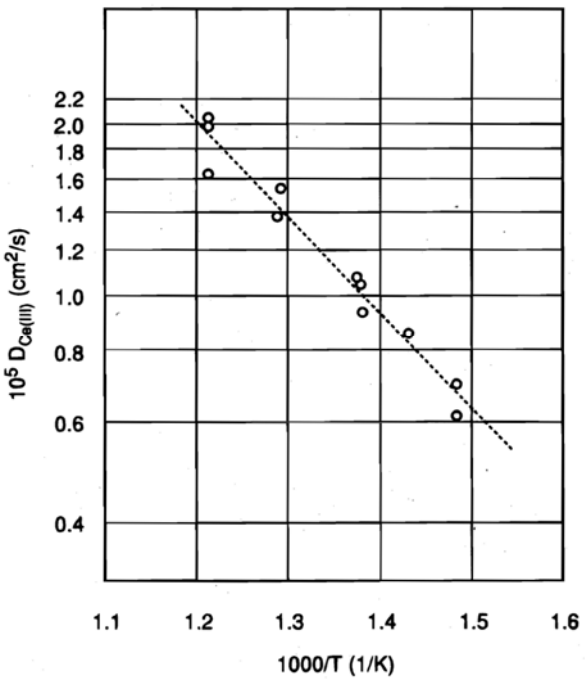

Fig. 2-5 Variation of diffusion coefficient of Ce(III) with temperature in LiCl-KCl

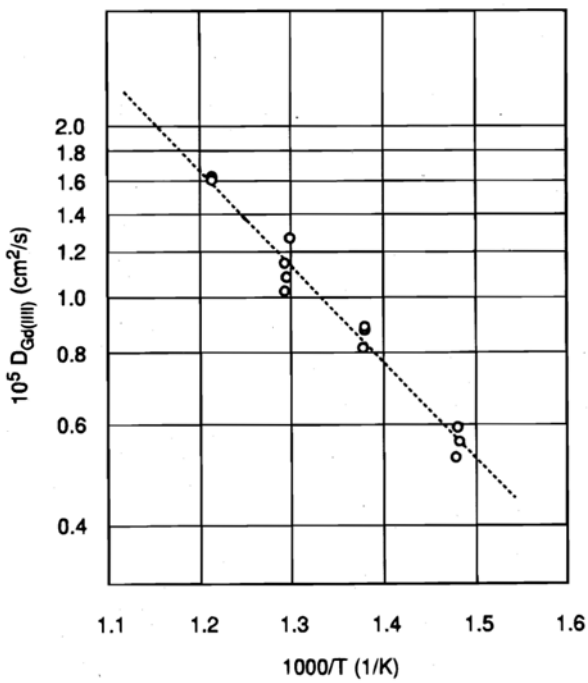

Fig. 2-6 Variation of diffusion coefficient of Gd(III) with temperature in LiCl-KCl

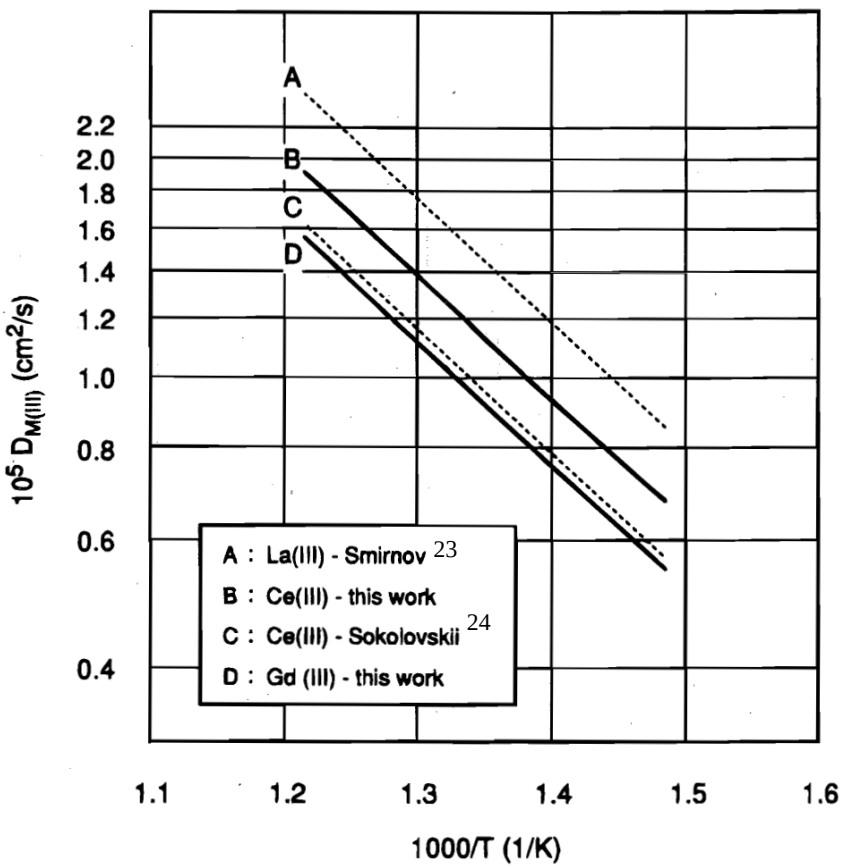

Fig. 2-7 Diffusion coefficients of La(III), Ce(III) and Gd(III) in LiCl-KCl

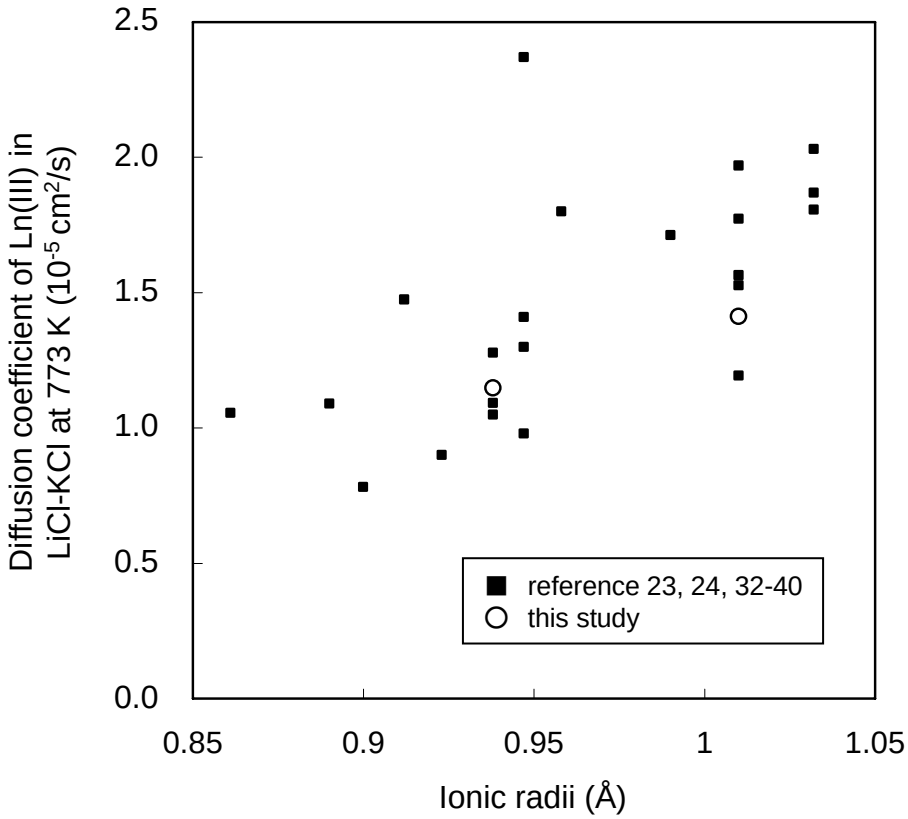

Fig. 2-8 Relation between diffusion coefficient in LiCl-KCl at 773 K and ionic radii of trivalent lanthanide ions

Chapter 3 Actinides recovery from molten salt/liquid metal system by electrochemical methods

3.1 Background and objectives

According to many batches of spent fuel are processed in the electrorefining step, a large amount of fission products (FPs) accumulate in the solvents; noble metal FPs (Ru, Mo, etc.) in the liquid cadmium layer at the bottom of the electrorefiner and chemically more active FPs (Nd, Ba, Cs, etc.) in the molten salt electrolyte. Before these solvents are sent to the waste treatment process, the actinides which also exist in them have to be collected to attain high recovery ratio.

For the recovery of the actinides from these solvents, electrochemical methods have been proposed because they might require less additional equipment. The electrochemical recovery of the actinides from the electrorefiner is considered to be done in two steps : (i) electrotransport of the actinides from liquid cadmium layer, and (ii) electrochemical reduction and recovery of the actinides from molten salt electrolyte. In this report, both methods were experimentally examined and the behavior of uranium and rare earth elements in these processes was investigated.

3.2 Reactions in actinides recovery processes

3.2.1 Electrotransport of actinides from liquid cadmium

The liquid cadmium layer at the bottom of the electrorefiner is made anodic and current is passed between it and a solid steel cathode suspended in the molten salt electrolyte (Fig. 3-1).

At the anode, the actinides and rare earths are anodically dissolved.

$$\mathrm{An}_{\mathrm{inCd}} = \mathrm{An}^{3+}_{\mathrm{insalt}} + 3e^{-} \quad \text{(An : actinides)} \tag{3-1}$$

$$\mathrm{RE}_{\mathrm{inCd}} = \mathrm{RE}^{3+}_{\mathrm{insalt}} + 3e^{-} \quad \text{(RE : rare earths)} \tag{3-2}$$

After these elements are exhausted from the anode, the solvent cadmium would be then dissolved into the salt.

$$\mathrm{Cd} = \mathrm{Cd}^{2+}_{\mathrm{insalt}} + 2e^{-} \tag{3-3}$$

At the cathodes, actinides or rare earths are reduced unless concentrations of these elements are not very low.

$$\mathrm{An}^{3+}_{\mathrm{insalt}} + 3e^{-} = \mathrm{An} \tag{3-4}$$

$$RE^{3+}_{insalt} + 3e^- = RE \quad (3\text{-}5)$$

These reactions are affected by mechanical factors such as the geometric structure of the electrorefiner and the intensity of stirring as well as by electrochemical factors like the composition of the solutions and the current density. Their reaction rates are expected to be estimated approximately by the diffusion layer model using the redox potentials, diffusion coefficients and the effective thickness of the diffusion layers [1]. In Argonne National Laboratory (ANL), this procedure was investigated in the molten salt electrolyte containing 3.4 wt% of uranium and 1.5 wt% of rare earths, and it was found that no rare earths was deposited at the cathode [2].

3.2.2 Electrochemical reduction of actinides from molten salt electrolyte

In the electrochemical reduction of the actinides from the molten salt electrolyte (Fig. 3-2), reductive material like a Cd-Li alloy is used as an anode in order to avoid the evolution of corrosive chlorine gas and to generate a stable oxidation product which does not affect the decontamination at the cathode.

At the anode, direct chemical reduction of the actinides and rare earths in the electrolyte with lithium metal at the anode is expected to occur,

$$An^{3+}_{insalt} + 3Li_{inanode} = An + 3Li^+_{insalt} \quad (3\text{-}6)$$

$$RE^{3+}_{insalt} + 3Li_{inanode} = RE + 3Li^+_{insalt} \quad (3\text{-}7)$$

in addition to anodic dissolution of lithium.

$$Li_{inanode} = Li^+_{insalt} + e^- \quad (3\text{-}8)$$

At the cathode, the actinides and rare earths would be reduced first. After the concentration of these elements gets lower, lithium can be reduced at the cathode.

$$Li^+_{insalt} + e^- = Li \quad (3\text{-}9)$$

ANL named this electrochemical reduction step "draw down", and studied it in the electrolyte containing uranium and plutonium. They reported that the concentration of uranium in the electrolyte could be decreased from 6.68 wt% to 0.015 wt% by draw down operation with Cd-Li alloy anode [3], and indicated that the possibility of direct chemical reaction between Li-Cd alloy and the actinides/rare earths in the electrolyte [4]. In their report, however, no discussions were found on the detail of reaction at the Cd-Li anode nor the electrochemical parameters like the

electrode potentials, although these are significantly important points considering the collection efficiency of the actinides at the cathode.

3.3 Experimental

The experimental apparatus is schematically shown in Fig. 3-3.

All the experiments were carried out in a argon-atmosphere glove box. Oxygen and moisture in the glove box were kept below 20 ppm respectively,

The size of the electrorefiner vessel is 180 mm in diameter and 200 mm in depth. It was heated by an electric furnace to keep the temperature of the electrolyte at 773K. About 3 kg of the electrolyte salt (LiCl-KCl eutectic) and about 6 kg of cadmium metal were loaded into the vessel. The surface area of the liquid cadmium layer was approximately 240 cm^2.

Cd-Li anodes used in the electrochemical reduction tests were prepared in another glove box. Lithium metal was added into liquid cadmium to make about 6 wt% Li-Cd alloy at 973K. The alloy, once cooled, was broken into small pieces. Before use, they are melted in zirconia crucibles and cooled again to be loaded into the electrorefiner. The Steel cathode was 30 mm in diameter and 50 mm in immersed length. It was rotated at about 20 rpm to obtain uniform deposit. A zirconia dish was located under the cathode to collect cathode product which slipped off the cathode. The reference electrode was Ag/AgCl (0.1 wt% AgCl-LiCl-KCl) electrode which was contained in a Pyrex tube.

All the chlorides and metals used in these tests were of more than 99.9% purity. The electrolyte salt (LiCl-KCl) was heated in the electrorefiner vessel to remove trace amount of moisture before it was melted. Cadmium was used after washing with diluted sulfuric acid. Uranium, lanthanum and cerium metal were polished to remove oxides on the surface before use. These metals were at first dissolved into the liquid cadmium layer at the bottom of the electrorefiner. Then they were oxidized by addition of $CdCl_2$ to adjust the initial composition of the liquid cadmium and the electrolyte salt. The electrolyte salt and liquid cadmium layer were agitated with a paddle-shaped stirrer.

During the tests, current was kept to desirable value and anode / cathode potentials were recorded. Samples were taken from the salt and the cadmium phases at an interval of 15 or 30 minutes.

The electrorefining analysis code "TRAIL" which is based on diffusion layer model [1] was used for comparison between experimental and calculation results. Thermodynamic data and parameters used in this report are shown in Table 3-1.

3.4 Results and discussion

3.4.1 Electrotransport of actinides from liquid cadmium layer

Uranium and rare earths in the liquid cadmium layer at the bottom of electrorefiner were electrotransported to solid steel cathode. The initial composition of the salt and the cadmium are shown in Table 3-2. Current density was 0.02 A/cm^2 at the anode and 0.1 A/cm^2 at the cathode, respectively.

The change of the electrode potentials and the composition of the cadmium layer are shown in Fig. 3-4 and Fig. 3-5, respectively. The anode potential rose suddenly about 2.5 hours after the start of the test. By that time, uranium concentration in the cadmium had decreased to about 0.1 wt%. From this result, it is expected that the cadmium anode was polarized due to the exhaustion of uranium. The electrotransport of uranium from the cadmium did not occur after this point because cadmium would be dominantly oxidized on such conditions. The cathode product in this test contained approximately equal amount of uranium as cerium. This ratio is about one third of that in the cadmium anode and more than twenty times larger than that in the salt at the beginning of the test.

The calculated results, which are also shown in Fig. 3-5, indicates that the behavior of uranium, lanthanum and cerium in electrotransport can be well explained by the diffusion layer model.

3.4.2 Electrochemical reduction of actinides from molten salt electrolyte

The Cd-Li anode contained in the zirconia crucible and the steel cathode were used. The anodic current density was changed as a parameter. The initial composition of the salt and the cadmium are shown in Table 3-3 with the anodic current density. Each test was divided into three runs. These three runs were carried out in the same system but the electrorefiner was cooled down after each run.

(1) Electrochemical reduction at higher anodic current density (0.293A/cm^2)

Fig. 3-6 shows the change of the salt composition in the test at higher anodic current density. It can be seen that uranium was removed from the salt at first and then cerium and lanthanum followed it.

The change of the electrode potentials in the same runs are shown in Fig. 3-7. A very low (about -2.5 V) cathode potential in Run 6 and 7 suggests that rare earths or lithium were reduced dominantly after uranium concentration in the salt decreased to about 0.1 wt%. Results from the chemical analysis of the cathode products in these runs (Table 3-4) clearly showed that the major constituent of the cathode deposit

changed from uranium to rare earths. Thus, it was found difficult to recover uranium from the salt by electrochemical reduction at a lower concentration than 0.1 wt% due to the contamination of the cathode product by rare earths. This result agrees exactly with that obtained in ANL indicating that the uranium concentration in the electrolyte salt could be reduced to 0.1 wt% by "draw down" operation without removing significant quantities of rare earths from the electrolyte [5].

Mass balances of uranium, cerium and lanthanum in these runs are shown in Fig. 3-8. Total amounts plotted in Fig. 3-8 are sums of those in the liquid cadmium layer at the bottom of the electrorefiner, in the salt and in the cathode products. It can be seen that the mass balances of these elements were well kept throughout the runs within the range of errors in sampling and chemical analysis.

(2) Electrochemical reduction at lower anodic current density ($0.195 A/cm^2$)

Fig. 3-9 shows the change of the salt composition in the test at lower anodic current density. It can be seen that uranium, cerium and lanthanum in the salt decreased faster than in the case at the higher anodic current density (shown in Fig. 3-6). This is thought to be caused by the direct chemical reduction of these elements at the Cd-Li anode (see below). The composition of the cathode products (Table 3-4) showed that uranium was mainly reduced at the cathode in run 8 and that rare earths and lithium were dominantly reduced in run 9 and 10. Fig. 3-10 shows mass balances of uranium, cerium and lanthanum in these runs. The total amount of uranium was clearly decreased while essentially no changes were found in those of cerium and lanthanum. This is also expected to be due to the direct chemical reduction at the Cd-Li anode.

(3) Direct chemical reduction at the anode

The sum of the amount of uranium, cerium and lanthanum in the salt in the electrochemical reduction tests are plotted in Fig. 3-11. At lower anodic current density, the amount of these elements decreased faster than calculated with the amount of the electric charge (Fig. 3-11(A)). This difference is expected to be caused by the direct chemical reduction with lithium metal at the anode. In fact, a paste-like product which contained high concentrations of uranium was found on the anode crucibles after most of runs. The content of the elements could not determined because those products are easily dispersed in the salt and involved a large amount of the electrolyte salt.

Because of these undesirable characteristics of the anode product, it is preferable to collect actinides only at the cathode. To investigate conditions which

restrain the direct chemical reduction at the anode, the anode potential in the electrochemical reduction tests was compared with a value calculated with Nernst equations with the concentration of uranium in the bulk salt (Fig. 3-12). At a higher anodic current density, the anode potential was higher than the calculated value almost throughout the tests, indicating that uranium tended to be oxidized at the anode. On the other hand, the anode potential was occasionally lower than the calculated value at a lower anodic current density. Under this condition, the direct chemical reduction of uranium at the anode was likely to occur to produce a large amount of anode product.

From these results, the direct chemical reduction of uranium at the anode in electrochemical reduction could be avoided by monitoring the anode potential and keeping it higher than the deposition potential of uranium calculated with the composition of the bulk salt.

3.5 Summary

For recovery of actinides from molten salt / liquid cadmium system, (1) the electrotransport of uranium from a liquid cadmium layer, and (2) the electrochemical reduction of uranium from a molten salt electrolyte were examined. Uranium was successfully recovered from both liquid cadmium and molten salt electrolyte. At a uranium concentration lower than 0.1 wt%, recovery was difficult from either liquid cadmium or molten salt due to the polarization of the anode or contamination of the cathode product by rare earths. A diffusion layer model well explains the behavior of the electrotransport from the liquid cadmium anode. In electrochemical reduction from molten salt, direct chemical reductionoccurred at the anode especially at a lower anode potential higher than the deposition potential of uranium.

References

[1] T. Kobayashi and M. Tokiwai, “Development of TRAIL, A simulation code for molten salt electrorefining of spent nuclear fuel”, J. Alloys and Compounds, V 197, 7-16 (1993)

[2] Annual Technical Report for 1993, Chemical Technology Division, Argonne National Laboratory Report ANL-94/15 (1994), p. 93.

[3] Annual Technical Report for 1992, Chemical Technology Division, Argonne National Laboratory Report ANL-93/17 (1993), p. 116.

[4] Annual Technical Report for 1995, Chemical Technology Division, Argonne National Laboratory Report ANL-96/10 (1996), p. 77.

[5] Annual Technical Report for 1994, Chemical Technology Division, Argonne

National Laboratory Report ANL-95/24 (1995), p. 92.

Table 3-1 Thermodynamic data and parameters used in calculation

	U	Ce	La
Standard potential (V versus Ag/0.1 wt% AgCl–LiCl–KCl)	−1.10	−1.69	−1.71
Activity coefficient in salt (−)	1.00	1.00	1.00
Diffusion coefficient in salt (cm^2/s)	1.00×10^4	1.00×10^4	1.00×10^4
Activity coefficient in cadmium (−)	88.7	1.13×10^{-5}	1.13×10^{-8}
Diffusion coefficient in cadmium (cm^2/s)	1.50×10^{-5}	1.50×10^{-5}	1.50×10^{-5}
	Anode cadmium		Steel cathode
Thickness of diffusion layer (cm)	in salt, 0.020	in Cd, 0.002	in salt, 0.020

Table 3-2 Initial composition of electrolyte salt and cadmium layer in electrotransport tests

	U	Ce	La
Concentration in the salt (wt%)	0.14	2.91	1.48
Concentration in the cadmium (wt%)	0.45	0.17	0.03

Table 3-3 Initial composition of electrolyte salt and cadmium layer in electrochemical reduction tests

Run no.	Anodic current density (A/cm^2)	U		Ce		La	
		in the salt	in the Cd	in the salt	in the Cd	in the salt	in the Cd
5	0.293	0.45	0.16	0.35	< 0.01	0.49	< 0.01
6	0.293	0.12	0.20	0.31	< 0.01	0.48	< 0.01
7	0.293	0.008	0.17	0.20	0.04	0.40	0.03
8	0.195	0.51	0.19	0.39	< 0.01	0.51	< 0.01
9	0.195	0.05	0.25	0.31	0.02	0.46	0.01
10	0.195	0.009	0.23	0.17	O.04	0.34	O.04

Table 3-4 Analytical resutl of cathode products in electrochemical reduction tests

Run No.	Weight (g)	U (wt%)	Ce (wt%)	La (wt%)
5	95.11	14.14	0.38	0.58
6	18.82	1.72	7.50	8.99
7	4.52	1.00	13.69	25.36
8	89.24	8.7	1.00	0.66
9	23.77	0.58	8.49	8.18
10	4.39	0.81	12.46	25.32

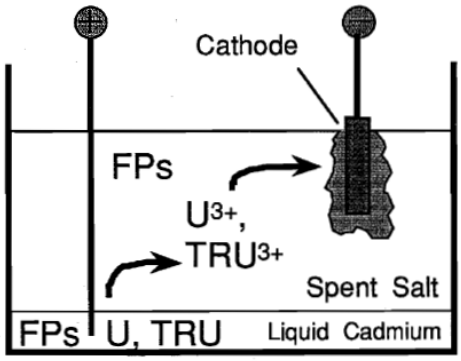

Fig. 3-1 Electrotransport of actinides from liquid cadmium

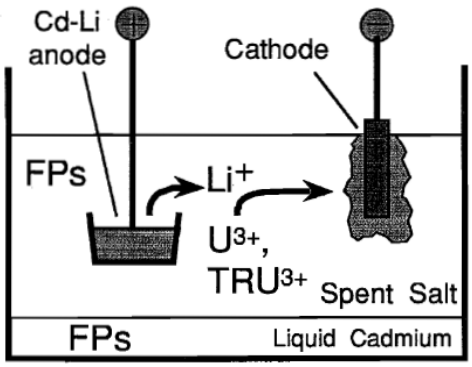

Fig. 3-2 Electrochemical reduction of actinides from molten salt electrolyte

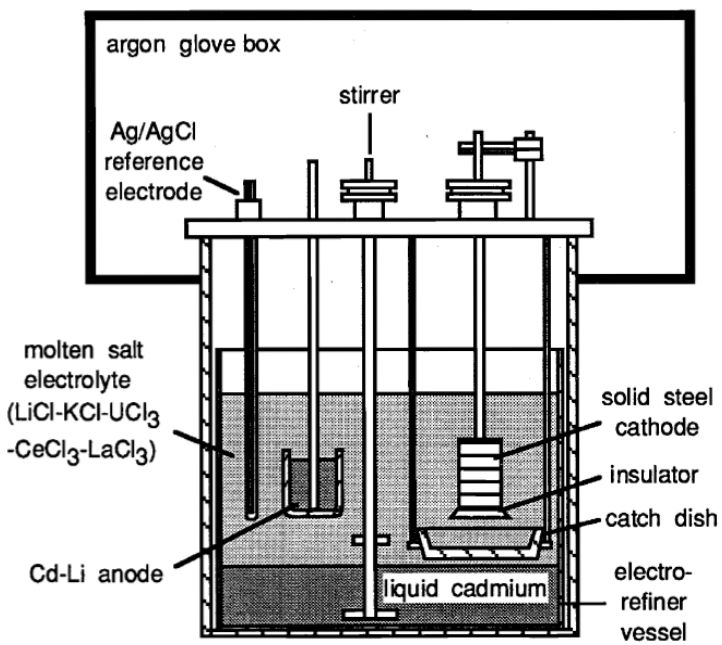

Fig. 3-3 Schematic view of experimental apparatus

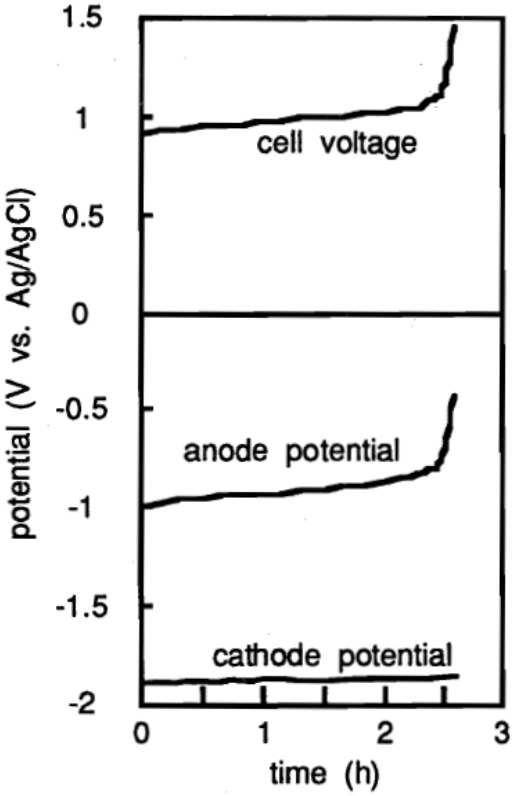

Fig. 3-4 Change of electrode potentials in electrotransport tests

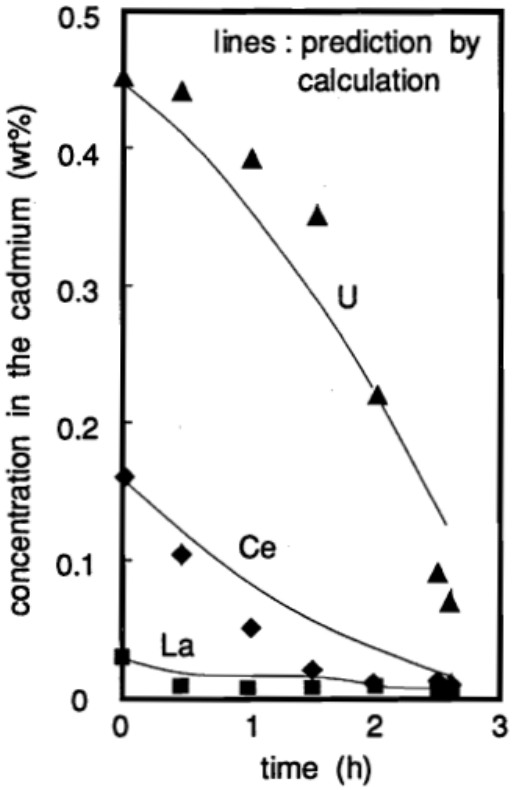

Fig. 3-5 Change of composition of liquid cadmium layer in electrotransport tests

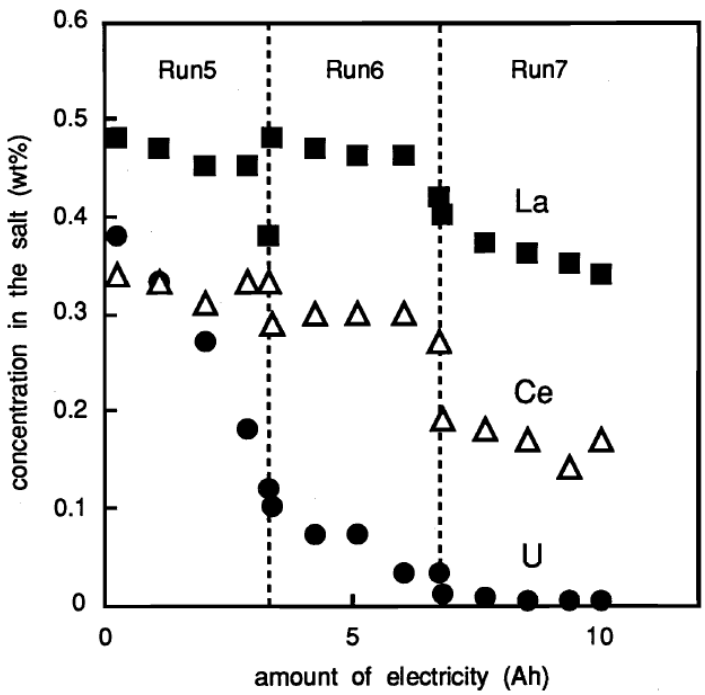

Fig. 3-6 Change of composition of molten salt electrolyte in electrochemical reduction tests (anodic current density = 0.293 A/cm^2)

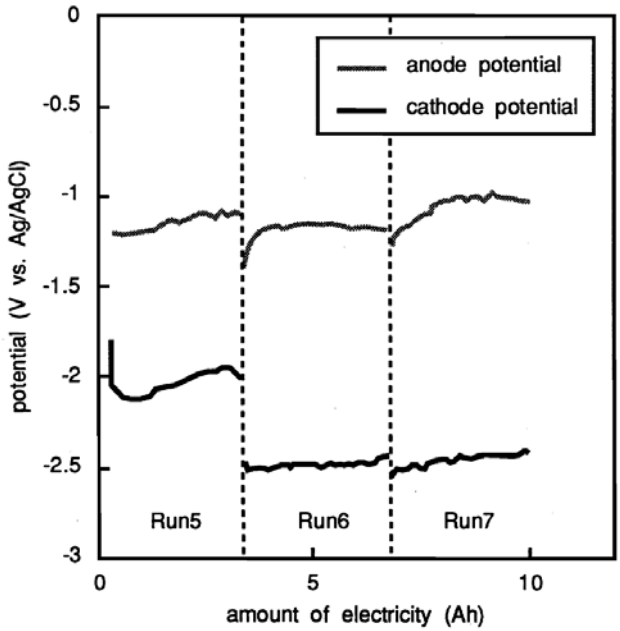

Fig. 3-7 Change of electrode potentials in electrochemical reduction tests (anodic current density = 0.293 A/cm^2)

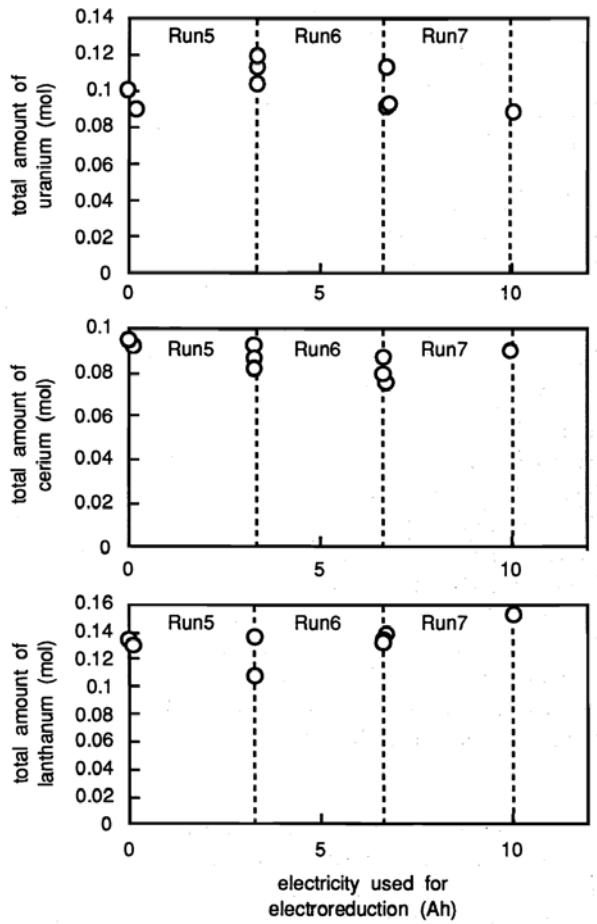

Fig. 3-8 Mass balance of uranium, cerium and lanthanum in electrochemical reduction tests (anodic current density = 0.293 A/cm^2)

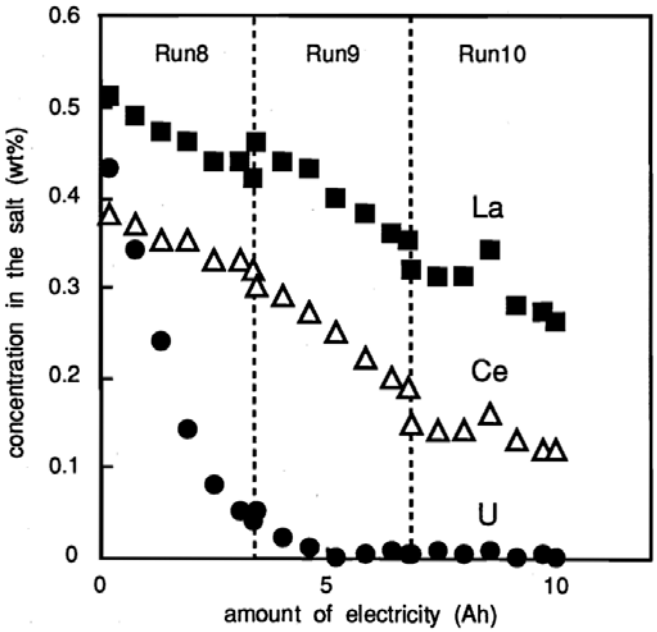

Fig. 3-9 Change of composition of molten salt electrolyte in electrochemical reduction tests (anodic current density = 0.195 A/cm^2)

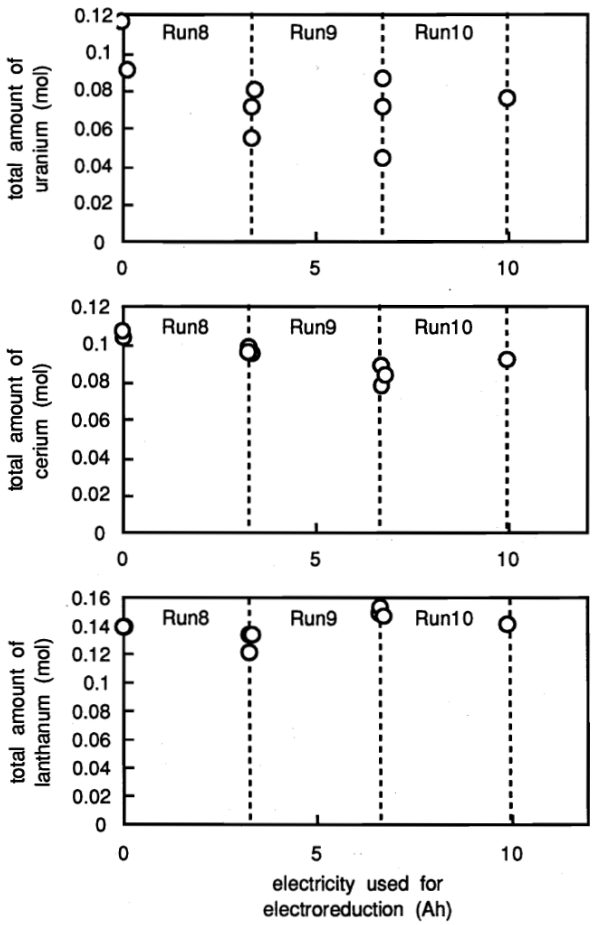

Fig. 3-10 Mass balance of uranium, cerium and lanthanum in electrochemical reduction tests (anodic current density = 0.195 A/cm^2)

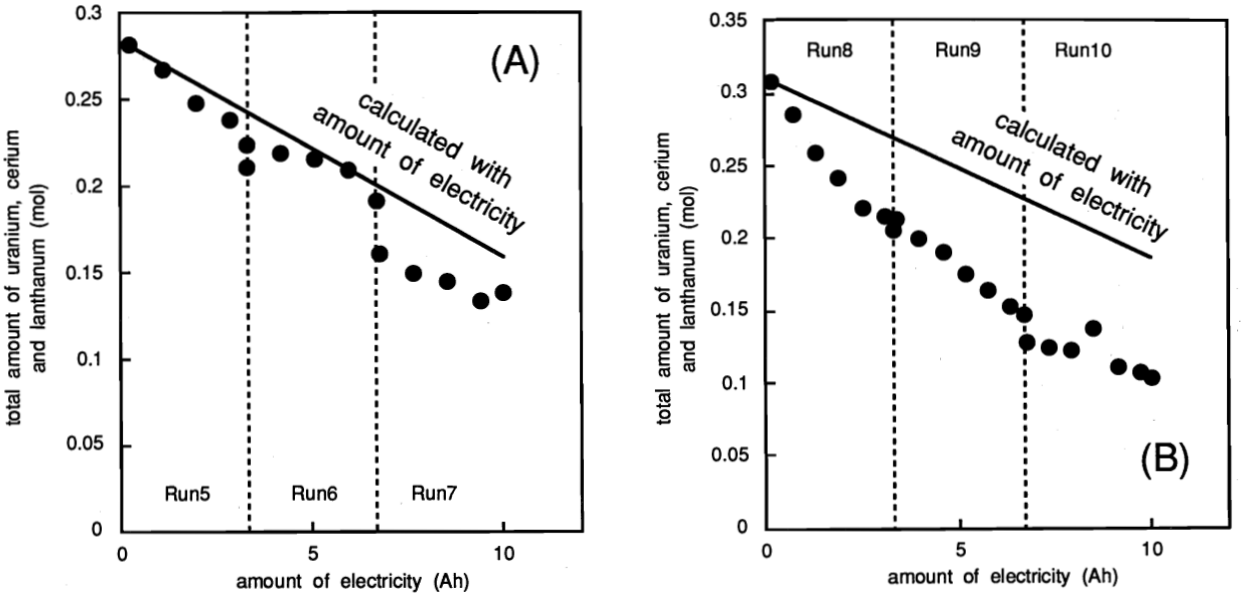

Fig. 3-11 Total amount of uranium, cerium and lanthanum in salt in electrochemical reduction tests : (A) anodic current density = 0.293 A/cm^2, (B) 0.195 A/cm^2

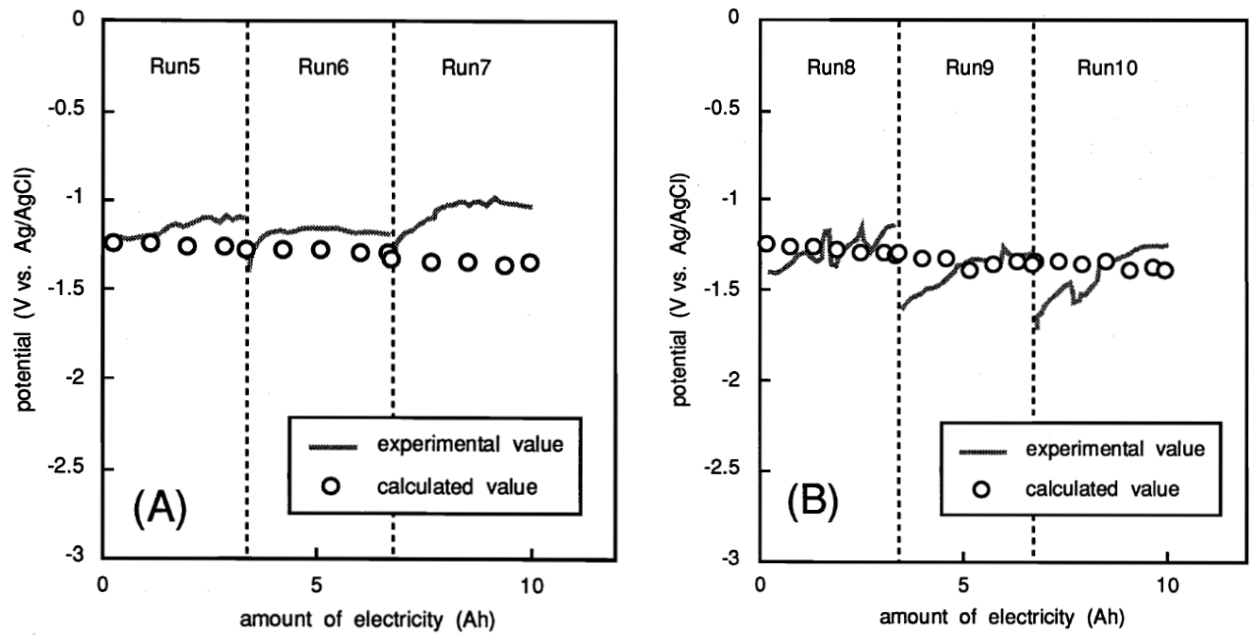

Fig. 3-12 Change of anode potential in electrochemical reduction tests : (A) anodic current density = 0.293 A/cm^2, (B) 0.195 A/cm^2

Chapter 4 Behavior of plutonium and americium at liquid cadmium cathode in molten LiCl-KCl electrolyte

4.1 Background and objectives

The main step in the pyrometallurgical process is the molten salt electrorefining [1], where the most part of the actinide elements in the spent fuel are recovered and decontaminated from the fission products. Fig. 4-1 shows a schematic flow of the normal operation of the electrorefining step. Two kinds of cathodes are used to obtain different streams of products. One is a solid cathode made of iron for the blanket material production, and the other is a liquid cadmium cathode (LCC) for the driver fuel material production. The free energy changes of chloride formation for some actinide and lanthanide elements at the two types of cathodes are shown in Fig. 4-2 [2]. At the solid cathode, uranium is selectively collected because the free energy change of chloride formation for uranium differs more than 30 kJ/mol from those for the other actinide and lanthanide elements. On the other hand, the free energy changes of the actinide elements are close to each other as seen in Fig. 4-2 because the transuranium elements (plutonium, neptunium, americium and curium) are stabilized in the LCC due to their very low activity coefficients in liquid cadmium [3,4]. Therefore, the transuranium elements are collected at the LCC together with uranium. Although a small amount of lanthanide fission products comes into the LCC product as expected from Fig. 4-2, it does not impact the performance of the fuel fabrication process or the reactor loaded with recycled fuel [5, 6]. The inevitable coexistence of γ emitting lanthanide fission products in recycled fuel could be rather an advantage in terms of proliferation resistance.

The use of the LCC is the most important technology in the pyrometallurgical process because plutonium is recovered and decontaminated from fission products in this step. Since the performance of the LCC significantly influences the feasibility of the pyrometallurgical reprocessing, ANL studied plutonium recovery with the LCC in depth with the laboratory scale equipment [7-10]. They devised the “pounder-type” LCC, which has a cylindrically shaped ceramic block rotating and reciprocating vertically above the cathode cadmium [10]. The pounder facilitates exchange of the electrolyte above the cathode and pushes solid product, which hampers stable LCC operation, down into the cathode cadmium. It was reported that more than 15 wt % of plutonium was recovered into 200 to 250 grams of cathode cadmium [10] using the pounder-type LCC made of beryllia or aluminum nitride. In Japan, the authors have reported on the behavior of uranium at LCCs, especially focusing on the formation of

dendritic uranium deposit [11, 12]. In those studies, it was shown that stirring in the cathode cadmium with the vertical paddles is effective to restrain growth of the uranium dendrite and that uranium can be collected into the LCCs at the cathodic current density of 0.2 A/cm^2 up to about 10 wt % in the cathode without dendrite formation [12]. In 1999, the plutonium electrorefining apparatus equipped with a LCC assembly was fabricated and installed in a joint research program between Japan Atomic Energy Research Institute (currently Japan Atomic Energy Agency) and Central Research Institute of Electric Power Industry on the pyrometallurgical processes. In this chapter, fundamental plutonium electrotransport experiments were carried out using this apparatus in order to understand the effects of electrochemical conditions on the behavior of plutonium at the LCC preceding investigation of the engineering factors like stirring method.

4.2 Experimental

4.2.1 Apparatus

All the experiments were carried out in a high purity argon atmosphere glove box. Both the oxygen and the moisture levels in the atmosphere were kept less than two ppm during the tests. Fig. 4-3 is a schematic view of the experimental apparatus. Inner diameter and depth of the container for the molten salt were 124 mm and 120 mm, respectively. About 1200 grams of lithium chloride-potassium chloride (LiCl-KCl) eutectic mixture was loaded in this container. Under the molten salt electrolyte, a liquid cadmium layer was placed and used as an anode which supplied plutonium in the electrotransport experiments. The amount of the anode cadmium was about 1400 grams. The salt and the anode cadmium were heated with an electric furnace and the temperature of the system was kept to 773 ± 1 K by a proportional-integral-differential (PID) controller. The molten salt and the liquid cadmium anode layer were stirred by rotating small vertical paddles (30 mm O.D., 6 mm height) at 60 rpm.

The electrorefining apparatus and the cathode assembly were originally designed to accommodate a LCC of 50 mm outer diameter, which would be stirred to facilitate the mass transfer of plutonium. In this study, however, much smaller cathodes were used because the study aimed to understand the effects of fundamental electrochemical conditions on the behavior of plutonium at the LCC before investigation of the engineering factors like stirring method. The size of the cathode crucible used in this study was 9 mm in diameter and 16 mm in depth. About 3 to 5 grams of cadmium was loaded in the crucible. A tungsten wire of 1mm diameter with a

high purity alumina sheath of 2mm outer diameter was immersed in the cathode cadmium and was used as an electric lead. It was difficult to determine the surface area of the liquid cadmium cathode exactly because it is largely affected by the wetting behavior of liquid cadmium to the alumina parts. In this study, the surface area was evaluated to be 0.605 cm^2 simply on the assumption that the annular region between the cathode crucible and the alumina sheath was flat. A silver-silver chloride (1 wt % AgCl in LiCl-KCl) reference electrode contained in a thin Pyrex glass tube was used. The potential of the reference electrode was very stable at 773 K throughout the experiments.

4.2.2 Chemicals

The chlorides (LiCl-KCl, $CdCl_2$ and AgCl) were purchased from Anderson Physical Laboratory. Because their purity was no less than 99.99 % and their moisture content was negligibly low, they were used without additional purification procedure. Cadmium metal of more than 99.9999 % purity for the anode and the cathode was purchased from Rare Metallic Corporation. Because the cadmium had been packed under vacuum just after production to avoid oxidation by the air, it was not washed or polished before use. The purity of the other electrode materials such as tungsten, tantalum, molybdenum and silver, was no less than 99.95 %. These metals were polished with # 1000 emery paper. They were then washed in diluted nitric acid and in distilled water with an ultrasonic cleaner. PuO_2 used in this study contained about 2 % of americium which was generated by (n, γ) reaction of Pu239 and β-decay.

4.2.3 Analytical procedures

EG&G Princeton Applied Research potentio/galvanostat Model 273A and EG&G 270/250 Research Electrochemistry Software were used for both the electrochemical measurement and the constant-current electrotransport. The concentrations of plutonium and cadmium in the molten salt were determined by inductively coupled plasma-atomic emission spectroscopy (ICP-AES) of the samples. The cathode products were analyzed by scanning electron microscope (SEM) and electron probe microanalyser (EPMA). An X-ray diffractometer (XRD) was also used to determine the chemical form of the cathode deposit.

4.2.4 Adjustment of plutonium concentrations in molten salt and liquid cadmium anode

In our previous studies on the chemistry and the electrochemistry of

plutonium in molten chlorides, plutonium trichloride ($PuCl_3$) was prepared in the following three steps [13] : (a) carbothermic reduction of PuO_2 to produce PuN [14], (b) formation of $PuPt_3$ by reaction between PuN and platinum metal, and (c) exchange reaction between $PuPt_3$ and cadmium chloride ($CdCl_2$) which yields $PuCl_3$ in a LiCl-KCl/liquid cadmium system. Although this is an established method to obtain $PuCl_3$ in LiCl-KCl, a large amount of expensive platinum metal becomes radioactive waste mixed with toxic cadmium. This problem is especially serious when a large amount of $PuCl_3$ is needed. Then, another method was adopted in this study. PuN obtained in the step (a) was loaded in a basket made of molybdenum mesh, then immersed into the molten LiCl-KCl and directly reacted with $CdCl_2$ to produce $PuCl_3$ and N_2 gas. The amounts of PuN and $CdCl_2$ at the beginning of this study were 44.2 grams and 53.5 grams (excess of about 5 % over the required amount for complete reaction with PuN), respectively. The molten salt samples and the cyclic voltammograms (CV) for plutonium in the salt were taken periodically in order to follow the progress of the reaction. The experiment was finished 5 days after the beginning of the reaction because the change of CVs became almost negligible. There was a small amount of brown residue at the bottom of the basket, which was presumed to be PuO_2 generated by oxidation of PuN during storage. Fig. 4-4 shows the change of the concentrations of plutonium and cadmium in the molten salt during that process. It can be seen that the reaction between $PuCl_3$ and $CdCl_2$ was almost completed in 16 hours. Although the actual plutonium concentration in the salt was slightly lower than expected, the reaction efficiency was considered nearly 100 % taking account of the oxidation of PuN and the error from the chemical analysis of the samples.

The concentration of plutonium in the liquid cadmium anode was adjusted by reduction of $PuCl_3$ in the molten salt phase by addition of cadmium-lithium alloy as a reducing agent. Lithium metal itself was not used to avoid rapid reaction with plutonium chloride and dispersion of fine plutonium metal powder product, resulting in low material balance. As well as in the case of $PuCl_3$ preparation, the molten salt/liquid cadmium anode samples and the CVs for plutonium in the salt were taken periodically. The reaction was considered to complete in 20 hours because no more change could be found in the CVs after that. The reaction efficiency in the reduction step was determined to be approximately 100 % based on the chemical analysis of the samples.

After all these steps were completed, the concentrations of plutonium in the molten salt and in the liquid cadmium anode were 2.28 wt % and 1.72 wt %, respectively.

4.3 Results and discussion

4.3.1 Voltammetric study on the electrochemistry of plutonium at the liquid cadmium electrode

Preceding the electrotransport experiments, CVs were measured with the liquid cadmium electrode in order to obtain primary information about the electrochemical reaction of plutonium at the LCC. Fig. 4-5 shows the CVs for LiCl-KCl-PuCl3 measured with a liquid cadmium electrode whose dimension is identical to those used in the electrotransport experiments. The surface area of the electrode was estimated from the inner diameter of the crucible and the outer diameter of the insulator tube of the electric lead.

The reduction current of plutonium started to flow at about –1.2 V and it made a bump at about –1.5 V. In a CV measured with a solid electrode shown also in Fig. 5, the peak current for the reduction of plutonium appeared at –1.7 V which is 0.2 V lower than that in the case of the liquid cadmium electrode. The activity coefficient of plutonium in liquid cadmium at 773 K is reported to be 1.4×10^{-4} [3]. Because this value is equivalent to a 197 mV shift to the higher direction for a three-electron reaction at 773 K, the above potential difference between the two kinds of electrodes is thermodynamically reasonable.

In general, the current by diffusion-controlled reactions is proportional to square root of the potential scanning rate in CV [15]. However, the increase of the reduction current of plutonium at the liquid cadmium electrode was very little when the potential scanning rate was increased from 50 mV/s to 100 mV/s. This behavior indicates that the concentration of plutonium at the surface of the electrode went over its solubility limit and that a solid phase which was supposed to be $PuCd_6$ from the Cd-Pu phase diagram [16] was formed. In such a situation, the supply of free cadmium which lowers the activity of the reduced plutonium would be disturbed by the solid phase barrier. Then the reduction current of plutonium would not depend on the potential scanning rate, and it would be controlled by the supply of free cadmium from the inside to the surface of the electrode. When the potential was turned to the positive direction, the reduction product ought to have accumulated near the surface of the cathode and the oxidation peak current should have been controlled by diffusion of tri-valent plutonium ion in the molten salt. Consequently, the oxidation peak current at –1.1 V is approximately in proportion to square root of the potential scanning rate as shown in Fig. 4-5.

4.3.2 Plutonium electrotransport experiments at constant cathodic current density

In order to understand the behavior of plutonium at LCC and the proper conditions for plutonium recovery, the electrotransport experiments were carried out at various cathodic current densities and plutonium concentrations in the molten salt. Major results are summarized in Table 4-1 with the experimental conditions. There was essentially no change in the concentration of plutonium in the molten salt during each test. Because the amount of plutonium transported to the cathodes was very small compared to the inventory in the anode, the change of plutonium concentration in the anode was negligibly small. The polarization of the anode was also very small because the surface area of the anode was about two hundred time larger than that of the cathode.

(1) The change of the LCC potential and the plutonium collection efficiency

Run 1 to 4 were carried out at relatively lower plutonium concentration in the molten salt (2.11 to 2.34 wt %). The changes of the LCC potential in these tests are shown in Fig. 4-6. At the cathodic current density of 33 to 41 mA/cm^2, the cathode potential was kept between –1.4 V and –1.55 V after a slight shift to the lower direction at the beginning. In this range of the potential, the reduction of plutonium followed by Pu-Cd intermetallic compound is expected to occur at the LCC from the result of the CV measurement. The moderate change of the cathode potential indicated that plutonium was collected into the LCC without abrupt growth of solid phase at the interface. The collection efficiency for plutonium calculated from the increase of the cathode weight and the total electric charge as shown below were nearly 100 % on these conditions.

$$\text{. Collection efficiency (\%)} = \frac{\text{Increase of cathode weight (g)} \times 100}{\text{Total electric charge (C)} \,/\, 1210 \text{ (C/g - Pu)}}$$

This result supports the above consideration about the smooth collection of plutonium. Fig. 4-7 is the appearance of the cathode cadmium ingot taken out of the crucible in Run 2 where plutonium was collected up to 7.75 wt % into the LCC at the cathodic current density of 41 mA/cm^2. The top of the ingot was round due to the poor wetting between cadmium and the alumina crucible. Although there was a little inequality on the surface of the LCC, no growth of dendritic deposit was found.

In Run 3, the cathode potential went down to –1.65 V at the cathodic current density of 50 mA/cm^2. The solidified salt on the top of the cathode cadmium was white after this run although LiCl-KCl containing about 2 wt % of plutonium is usually light

blue. The collection efficiency of plutonium was about 80 % in this run, a little lower than in the preceding cases at the lower cathodic current densities. These results indicate that lithium in the electrolyte was electrochemically reduced at the LCC at –1.65 V and that the reduced lithium reacted with plutonium chloride near the cathode after the electrotransport. Lithium forms a very stable chloride whose standard potential is more than 0.6 V lower than that of plutonium at an inert electrode. However, redox potential of lithium is about 0.4 V higher at the LCC due to the very low activity coefficient of plutonium in liquid cadmium ($1.8 - 2.6 \times 10^{-3}$) [17]. In addition, the concentration of lithium ion around the LCC was very high because it was one of the solvent cations. In that situation, lithium should be reduced at the LCC in competition with plutonium. Fig. 4-8 shows a CV measured with a liquid cadmium electrode for LiCl-KCl containing no plutonium. It can be seen that the reduction current of lithium increases from around –1.6 V, suggesting the validity of the above consideration.

When the cathodic current density was increased to 66 mA/cm^2, the cathode potential once descended to –1.7 V and subsequently ascended in two steps. After the experiment, the cathode was visually inspected. The lower part of the alumina insulator sheath of the electric lead for the LCC had turned black and a deposit with metallic gloss was found on that region. X-ray diffraction analysis showed that the major portion of this deposit was $PuCd_6$. At such high cathodic current density, it is expected that the concentration of lithium at the surface of the LCC was so high due to the low cathode potential that the lithium reacted with the alumina sheath. It is very likely that the alumina sheath was wetted much more easily with liquid cadmium due to the reaction with lithium. This is considered the reason why the alumina sheath worked as a thin LCC and $PuCd_6$ was deposited there. The very low collection efficiency for plutonium (25 %) in Run 4 should also be attributed to the $PuCd_6$ formation out of the cathode cadmium.

The electrotransport experiments were carried out also at the higher plutonium concentration in the molten salt (Run 5 – 8). Before these tests, the concentration of plutonium in the molten salt was increased to 4.6 wt % by the procedure described in 4.2.4. Fig. 4-9 shows the change of the LCC potential in these tests. The overall tendency and the cathodic current density dependence of the cathode potential were similar to those seen in the preceding cases at the lower plutonium concentrations. At the cathodic current density of up to 100 mA/cm^2, the cathode potential was kept higher than -1.6 V throughout the test and no growth of solid phase product was observed at the surface of the LCCs. In Run 8, where the highest cathodic current

density (132 mA/cm^2) was applied, the cathode potential showed a rapid rise from -1.68 V to – 1.51 V. After cooling, small dendritic particles with metallic shine were observed in the molten salt phase just above the LCC. These results were also seen in Run 4 and indicate that $PuCd_6$ deposited out of the cathode cadmium due to the competitive reduction of lithium at the high cathodic current density.

(2) Proper conditions for plutonium recovery with LCC

Fig. 4-10 summarizes the result of the electrotransport tests at various cathodic current densities and plutonium concentrations in the molten salt. The circles in this plot represent the conditions on which plutonium was smoothly collected into the LCC with the collection efficiency of almost 100 %. The triangles denote the conditions on which the collection efficiency was decreased by the reduction of lithium and the reaction between the lithium and the ceramics parts. From these data, it is found that the maximum cathodic current density for successful plutonium collection with no-stirred LCC is proportional to the plutonium concentration in the molten salt as represented by the line in Fig. 4-10. This proportional relation indicates that the plutonium recovery rate was limited by transport of plutonium chloride to the surface of the LCC in the range of this study.

In practical electrorefining process, other factors should be taken into consideration. At higher plutonium concentration in the molten salt, the recovery rate can be controlled by the transport of reduced plutonium from the surface to the inside of the cathode as discussed in 4.3.1. On the other hand, larger cathodic current than shown in Fig. 4-10 can be expected in practical electrorefining equipment, because the LCC will be stirred to facilitate the transport of the actinide elements from the molten salt to the cathode cadmium.

However, an evaluation of plutonium recovery rate based on the experimental result, even at an early stage of development, is important because that kind of data is useful and necessary as a baseline for following tests in lager scale, investigations on the engineering factors, and design studies of whole pyrometallurgical processing plant. Then a rough estimation of plutonium recovery rate in practical scale electrorefining equipment was attempted as following by extrapolating the result from this study.

The sum of the concentrations of all actinides in the molten salt is planned to be adjusted to 2 mol % (about 8 wt %) in the practical operation of the electrorefining step [18]. In the LCC operation, the plutonium / uranium ratio in the molten salt will be set considerably high in order of avoid the formation of uranium dendrite. This ratio was assumed to be 7 / 1 in this estimation. The inner diameter of the practical scale

LCC was assumed to be 30 cm. Because the slope of the rate limiting line in Fig. 10 was 22 mA/cm^2・wt %-Pu, the reduction current of plutonium at one practical LCC can be evaluated as follows.

$$0.022\ (\mathrm{A/cm^2 \cdot wt\ \%}) \times 7\ (\mathrm{wt\ \%}) \times 152\ \pi\ (\mathrm{cm^2}) = 109\ (\mathrm{A})$$

This current is equivalent to a collection rate of 324 grams of plutonium per hour. This performance is considered high enough as an initial condition for design of the practical electrorefiner and pyrometallugical process.

(3) Behavior of plutonium and americium in the LCC

The LCC ingot recovered after the electrotransport was analyzed by EPMA in order to evaluate the behavior and distribution of plutonium in the cathode. Fig. 4-11 is a SEM image of the intersection of the LCC ingot obtained in Run 2, where plutonium was collected into the cathode up to 7.75 wt % at cathodic current density of 41 mA/cm^2. There is a layer containing a crystallized phase in high density near the bottom of the LCC. Fig. 4-12 is a characteristic X-ray image of plutonium of this layer. It is clearly shown that the crystallized phase in this region contains a high concentration of plutonium and that only a small amount of plutonium exists in the bulk. The composition of the plutonium-rich phase was quantitatively analyzed in the following steps. X-ray counts for plutonium and cadmium from the LCC ingot sample were normalized by counts from pure plutonium and cadmium standard specimens. All these counts were corrected for background counts and dead time of the detector. Subsequently, the data was corrected by the ZAF method until it reached convergence. In the result, the mole ratio between cadmium and plutonium in the plutonium-rich phase was determined to be 6.08, indicating that the deposit was $PuCd_6$.

From these results, it seems most likely that plutonium reduced at the LCC beyond the solubility limit in liquid cadmium instantly forms $PuCd_6$ solid phase at the surface of the LCC and settled down to the bottom of the cathode. It is still possible, however, that the segregation of $PuCd_6$ was caused by the vertical temperature gradient in the LCC, because it was cooled very slowly at only a few centimeters above the top of the salt due to the safety requirement. Further tests are needed to elucidate the mechanism of $PuCd_6$ accumulation at the bottom of the LCC.

The PuO_2 used in this study contained about 2 % of Am^{241} as described in 3.2. The exposure dose rate of γ-ray from Am^{241} in the LCC ingots was plotted as shown in

Fig. 4-13 versus the total content of plutonium collected in the cathodes. The dose rate was measured at both the top and the bottom of the ingots by a GM survey meter placed outside of the glove box at a distance of about 1 mm from the ingots.

These plots have a distinctive tendency. At the low concentrations of plutonium in the LCCs, the dose rate at either top or bottom of the ingots increased as the electrotransport proceeded. When the concentration of plutonium in the LCCs reached its solubility limit, however, the increase of the dose rate concurrently stopped. In the previous LCC study with uranium and lanthanide elements, similar situation was observed (Fig. 4-14) [18]. While the concentration of uranium in the LCC increased linearly to the electricity, deposition of gadolinium and neodymium stopped before uranium saturation and their concentrations remained almost constant. Such behavior of lanthanides was explained by the consideration based on a local equilibrium model where deposition of them is restrained after the increase of uranium activity in the LCC is stopped by saturation. In the present study, however, the behavior of americium should be essentially different from that of lanthanides coexisting with uranium. When the concentration of plutonium reaches its solubility in the LCC, it is very likely that the co-deposited americium accompanies plutonium to form an intermetallic compound like $Pu_{1-x}Am_xCd_6$ and accumulates at the bottom of the LCC because of their similar chemical characteristics. That should be the reason why the increase of the γ-ray exposure dose rate stopped with saturation of the LCC by plutonium and also why the dose rate at the bottom of the ingot was always higher than that at the top as seen in Fig. 4-13. The saturation of the exposure dose rate at the bottom is considered caused by self shielding by accumulated intermetallic compound.

Although the behavior of americium in the LCC is very important data for the design of the electrorefining step and the pyrometallurgical process, no additional information was obtained in this study. To verify the above consideration and understand americium behavior further, the thermodynamic study on Pu-Am-Cd ternary system and the analysis of the amount, distribution and chemical form of americium in the cathode cadmium will be needed.

4.4 Conclusions

From the cyclic voltammograms (CVs) measured with the liquid cadmium electrode, it was found that reduction of plutonium occurs at –1.5 V (vs. Ag/AgCl) or higher at the liquid cadmium cathode (LCC). This potential is about 0.2 V higher than that of a solid electrode in accordance with the low activity coefficient of plutonium in liquid cadmium.

Plutonium was collected into the no-stirred LCC without disturbance by solid phase formation at the surface. At plutonium concentration of 2.11 wt % in molten LiCl-KCl and cathodic current density of 41 mA/cm^2, the collection efficiency of plutonium was nearly 100 % and maximum plutonium loading into the LCC was 7.75 wt %. At the higher cathodic current densities, lithium metal was reduced and reacted with the ceramic LCC parts. The collection efficiency was decreased by $PuCd_6$ formation out of the LCC caused by those reactions.

The cathodic current density adequate for plutonium collection was proportional to the concentration of plutonium in the molten salt at the ratio of 22 mA/cm^2•wt %-Pu in the range of this study. At plutonium concentration of 5.0 wt % in molten salt, cathodic current density of 100 mA/cm^2 was attained without any trouble such as solid deposit growth or descent of cathode potential indicating reduction of lithium. The plutonium collection rate in a practical scale electrorefiner was estimated to be 324 grams per hour for one LCC based on the assumption that the collection rate is proportional to the plutonium concentration in the molten salt and the surface area of the LCC. This performance is considered high enough as an initial condition for design of the practical electrorefiner and pyrometallugical process.

It was considered that plutonium collected into the LCC after saturation formed intermetallic compound $PuCd_6$ and accumulated at the bottom of the LCC based on EPMA analysis of the LCC ingot. It is still possible, however, that segregation of $PuCd_6$ was caused by a vertical temperature gradient in the LCC in the course of the slow cooling process.

Increase of γ-ray count from Am^{241} in the LCC ingots stopped coincident with saturation with plutonium. At present, this behavior is explained by formation of a mixed intermetallic compound $Pu_{1-x}Am_xCd_6$ and its self shielding at the bottom of the LCC For further understanding, however, the thermodynamic study on Pu-Am-Cd ternary system and the quantitative analysis of americium will be needed.

References

[1] T. Koyama, R. Fujita, M. Iizuka, and Y. Sumida, “Pyrometallurgical reprocessing of fast reactor metallic fuel ― development of a new electrorefiner with a ceramic partition”, *Nucl. Tech.*, **110**, 357-368 (1995).

[2] T. Koyama, K. Uozumi, M. Iizuka, Y. Sakamura and K. Kinoshita, “Pyrometallurgical Data Book”, CRIEPI report T93033, 1995, *in Japanese*.

[3] I. Johnson, M. G. Chasanov and R. M. Yonco, “Pu-Cd system : Thermodynamics and partial phase diagram”, *Trans. Metallurg. Soc. AIME*,

233, 1408-1414 (1965).

[4] J. Roy, L. Grantham, D. Grimmett, S. Fusselman, C. Krueger, T. Storvick, T. Inoue, Y. Sakamura and N. Takahashi, “Thermodynamic properties of U, Np, Pu, and Am in molten LiCl-KCl eutectic and liquid cadmium”, *J. Electrochem. Soc.*, **143**, 2487-2492 (1996).

[5] M. Kurata, A, Sasahara, T. Inoue, M. Betti, J. Babelot, J. Spirlet and L. Koch, *Proc. of Int. Conf. on Future Nuclear Systems (Global ’97)*, Yokohama, Japan, Oct. 5-10, 1997.

[6] T. Yokoo, T. Ogata and K. Ohta, “A design study on the FBR metal fuel and core for commercial applications”, *J. Nucl. Sci. Technol.*, **37**, 636-645 (2000).

[7] Annual Technical Report for 1993, Chemical Technology Division, Argonne National Laboratory Report ANL-94/15 (1994), p. 89.

[8] Annual Technical Report for 1991, Chemical Technology Division, Argonne National Laboratory Report ANL-92/15 (1992), p. 120.

[9] Annual Technical Report for 1992, Chemical Technology Division, Argonne National Laboratory Report ANL-93/17 (1993), p. 112.

[10] Annual Technical Report for 1994, Chemical Technology Division, Argonne National Laboratory Report ANL-95/24 (1995), p. 86.

[11] T. Koyama, M. Iizuka, Y. Shoji, R. Fujita, H. Tanaka, T. Kobayashi, M. Tokiwai, “An experimental study of molten salt electrorefining of uranium using solid iron cathode and liquid cadmium cathode for development of pyrometallurgical reprocessing,” *J. Nucl. Sci. Technol.*, **34**, 384–393 (1997).

[12] T. Koyama, M. Iizuka, N. Kondo, R. Fujita, and H. Tanaka, “Electrodeposition of uranium in stirred liquid cadmium cathode”, *J. Nucl. Mater.*, **247**, 227-231 (1997).

[13] O. Shirai, T. Iwai, Y. Suzuki, Y. Sakamura and H. Tanaka, " Electrochemical behavior of actinide ions in LiCl-KCl eutectic melts", *J. Alloys. Compd.*, **271**, 685-688, (1998).

[14] Y. Arai, S. Fukushima, K. Shiozawa and M. Handa, " Fabrication of (U, Pu)N fuel pellets", *J. Nucl. Mater.*, **168**, 280-289, (1989).

[15] For example, A. Bard and L. Faulkner, “Electrochemical Methods, Fundamentals and Applications”, John Wiley & Sons, New York, 1980.

[16] T. B. Massalski ed., “Binary Alloy Phase Diagrams”, ASM International, 1990.

[17] M. Lewis and T. Johnson, " A study of the thermodynamic and reducing properties of lithium in cadmium at 773 K", *J. Electrochem. Soc.*, **137**, 1414-1418 (1990).

[18] T. Koyama, M. Iizuka, H. Tanaka, *Proc. ICONE-4*, New Orleans, LA, Mar. 10-14, 1996.

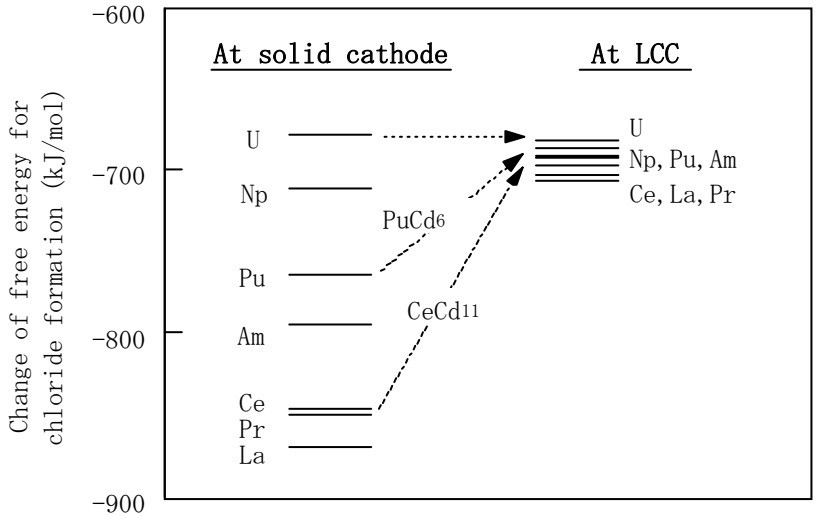

Fig. 4-2 ΔG_f of several chlorides at solid and liquid cadmium cathodes

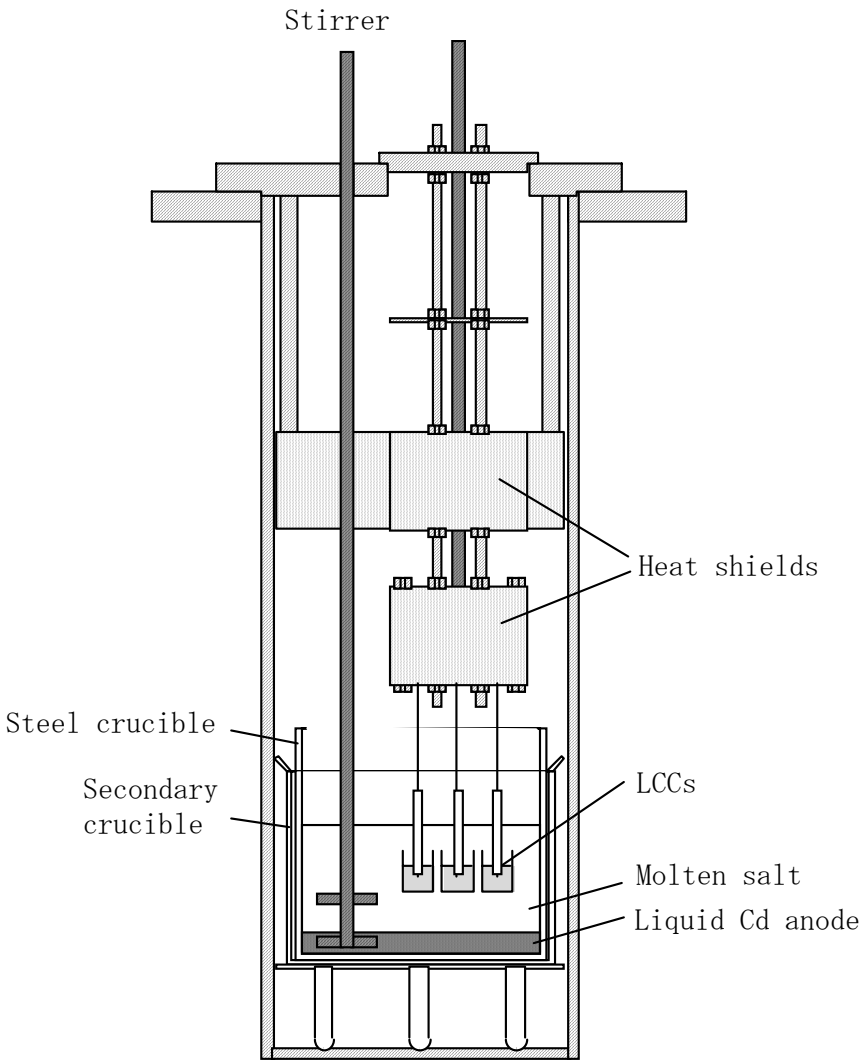

Fig. 4-3 Schematic view of the experimental apparatus

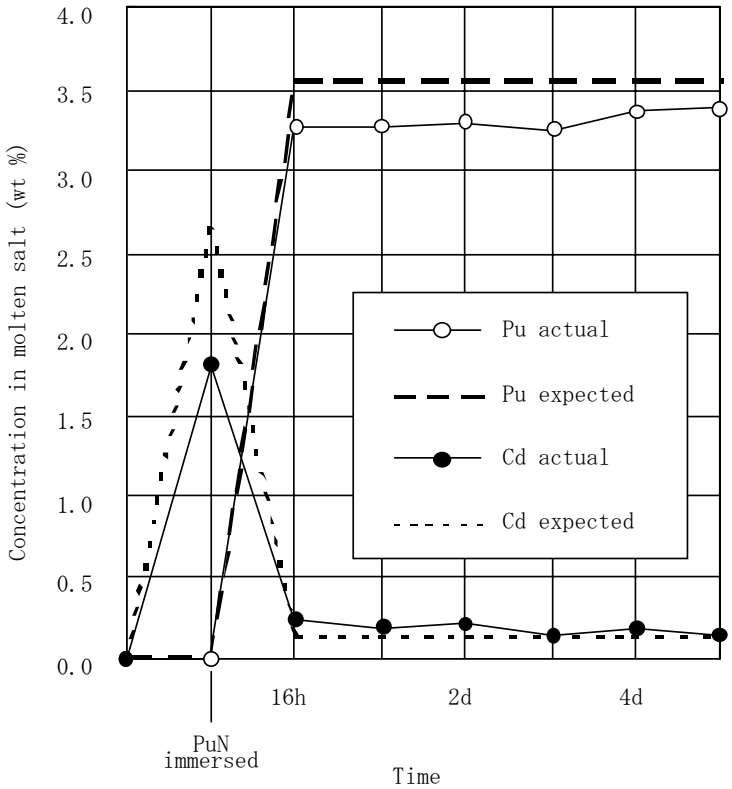

Fig. 4-4 Change of Pu and Cd concentrations in molten salt during $PuCl_3$ preparation from PuN

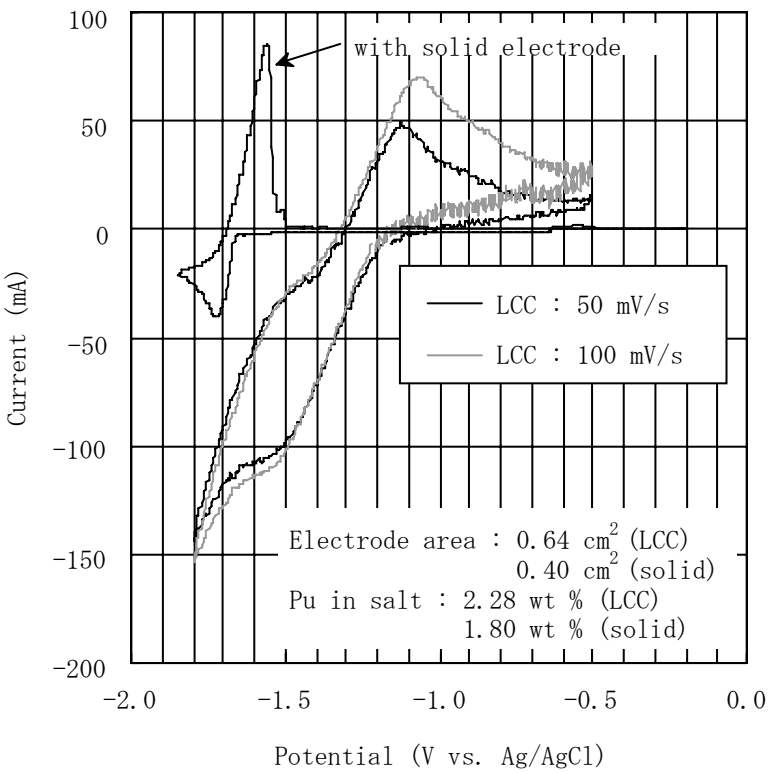

Fig. 4-5 Cyclic voltammograms for Pu in molten LiCl-KCl with solid and liquid cadmium electrodes

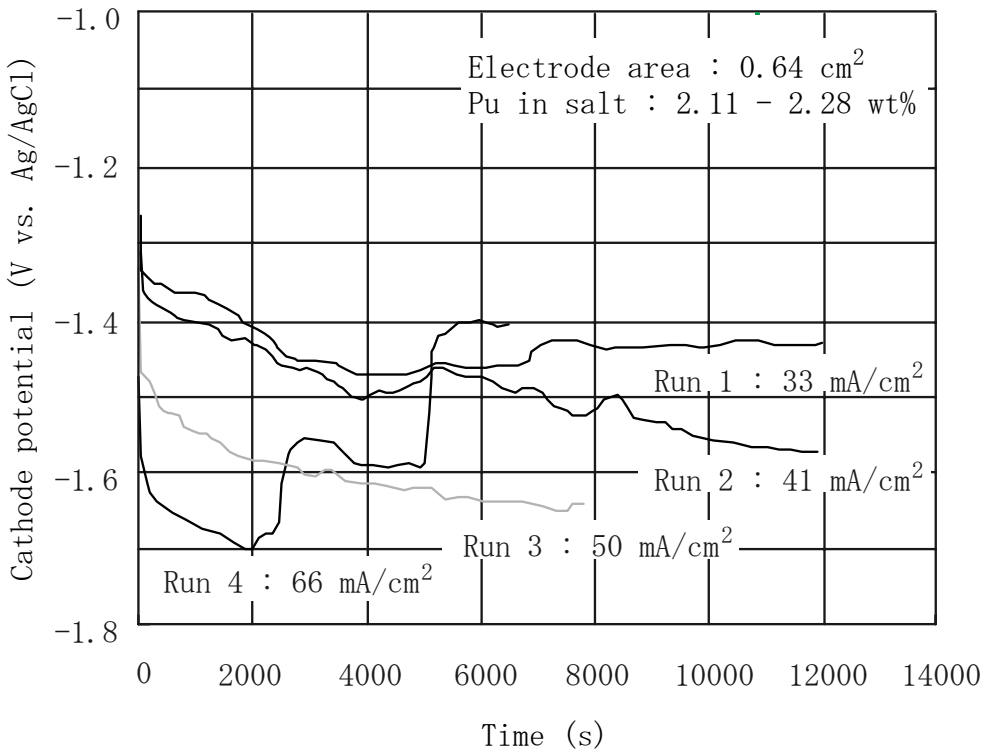

Fig. 4-6 Change of LCC potential in the Pu electrotransport tests (at the lower Pu concentration in molten salt)

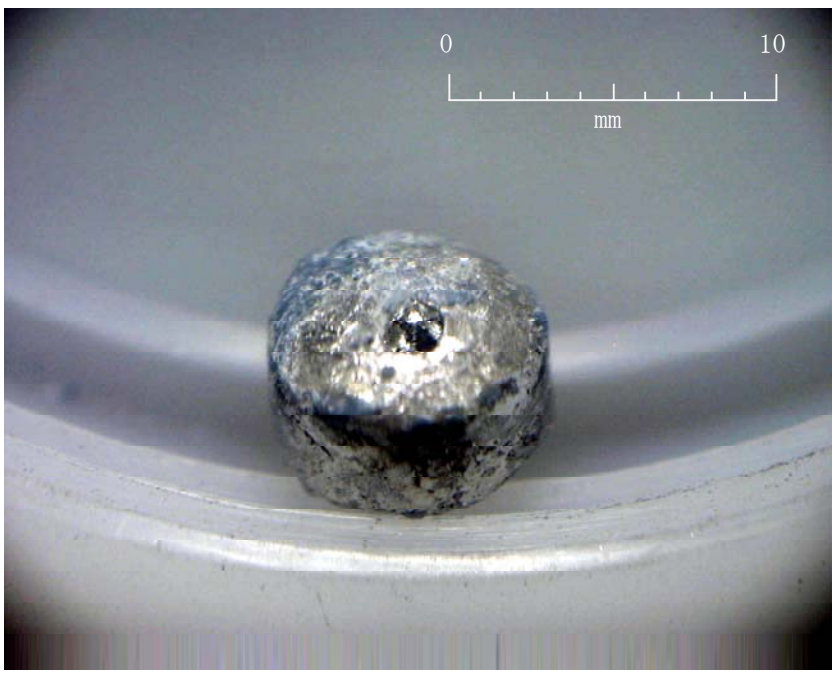

Fig. 4-7 Cathode Cd ingot obtained after the Pu electrotransport test at the cathodic current density of 41 mA/cm^2

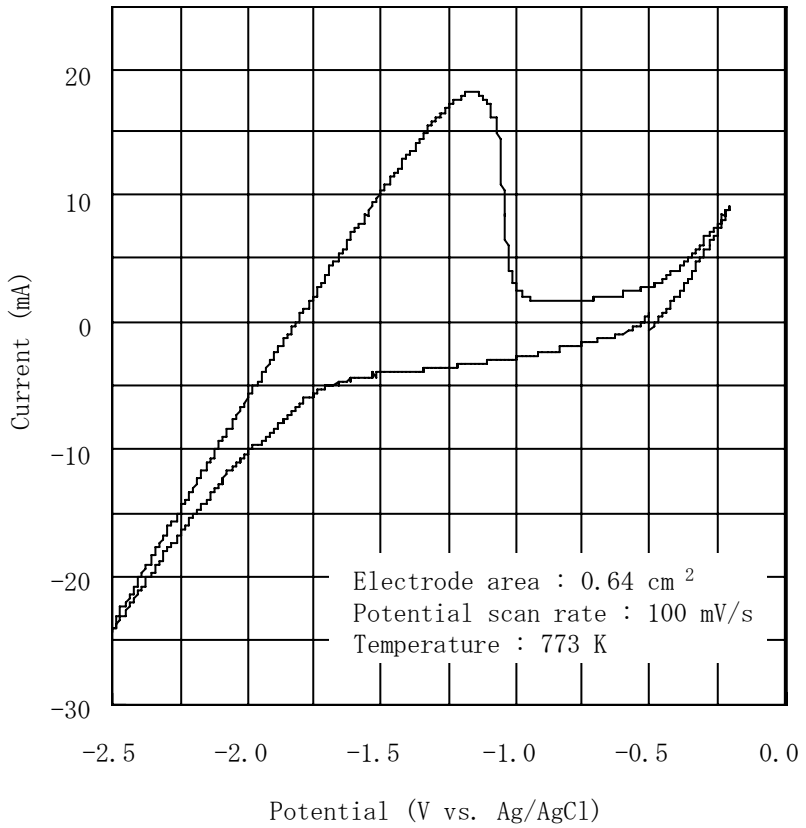

Fig. 4-8 Cyclic voltammograms for blank LiCl-KCl with liquid cadmium electrode

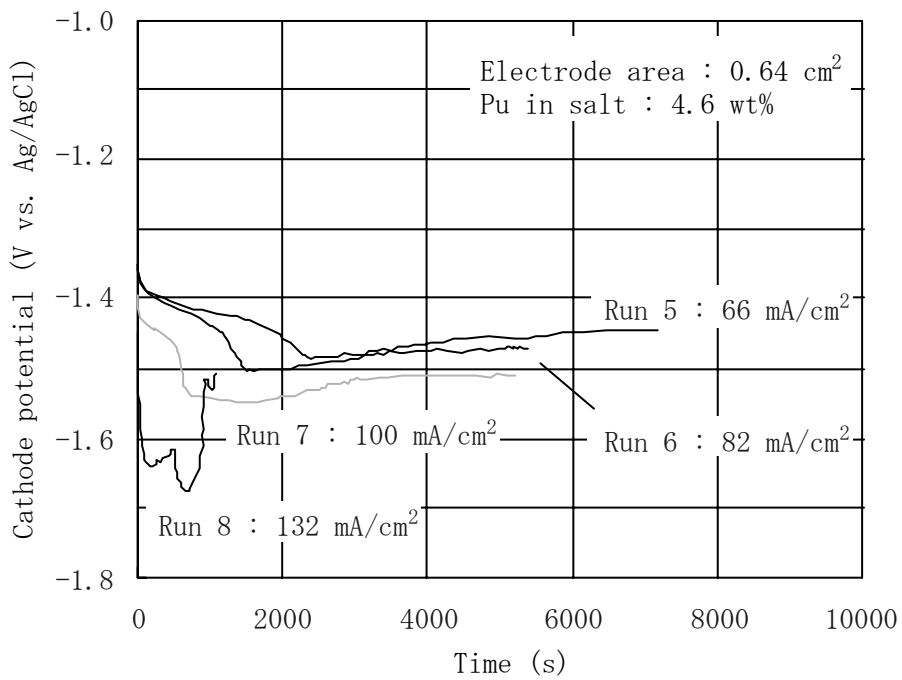

Fig. 4-9 Change of LCC potential in the Pu electrotransport tests (at the higher Pu concentration in molten salt)

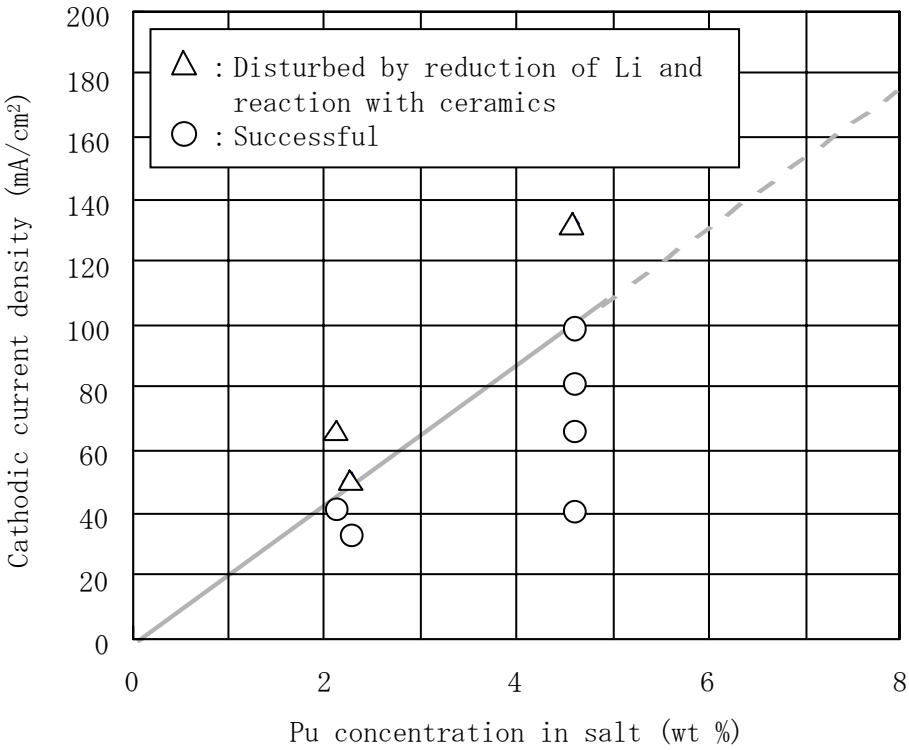

Fig. 4-10 Summary of the Pu electrotransport tests

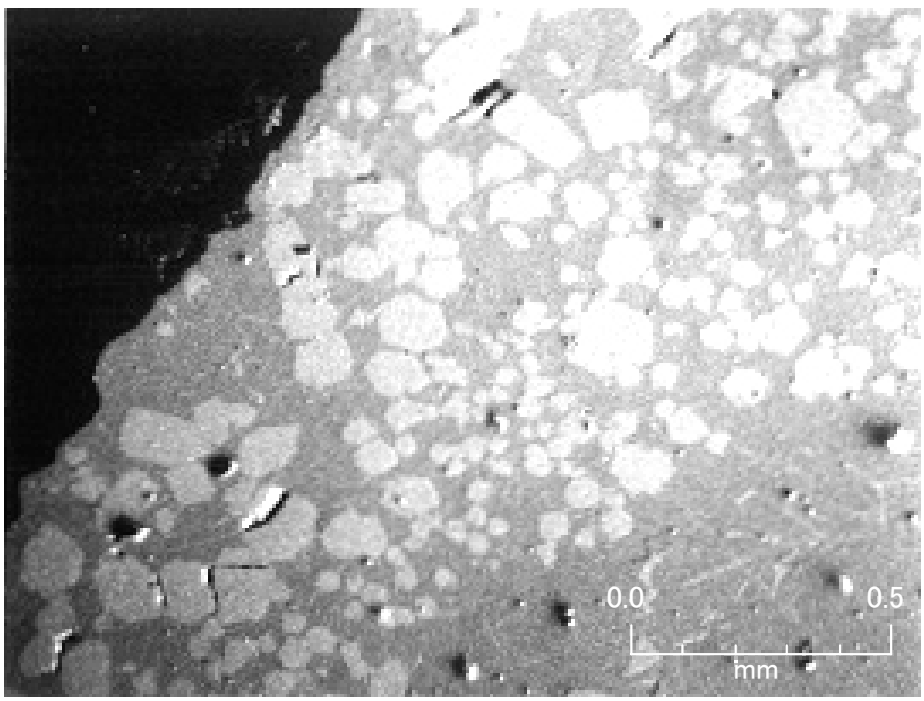

Fig. 4-11 SEM image of the LCC ingot shown in Fig. 4-7 (near the bottom)

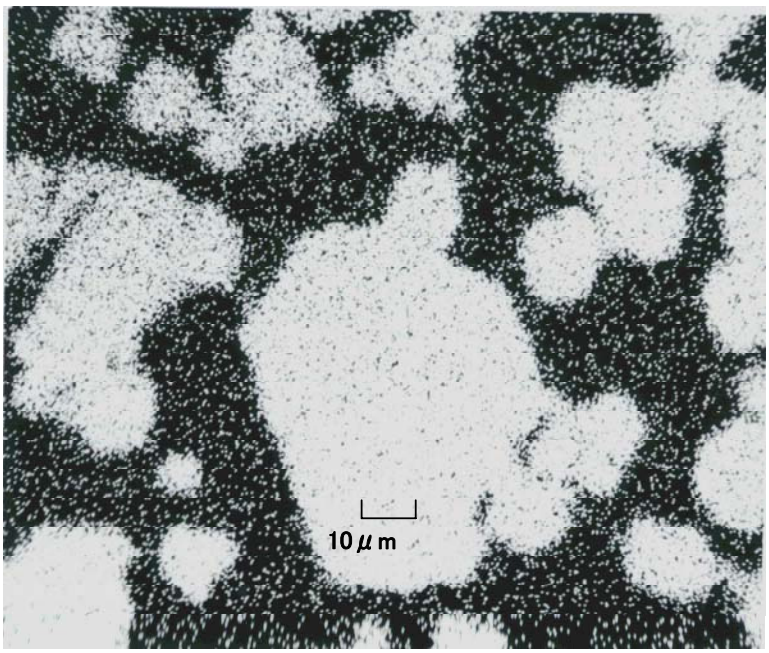

Fig. 4-12 Characteristic X-ray image of Pu at the bottom region of the LCC ingot

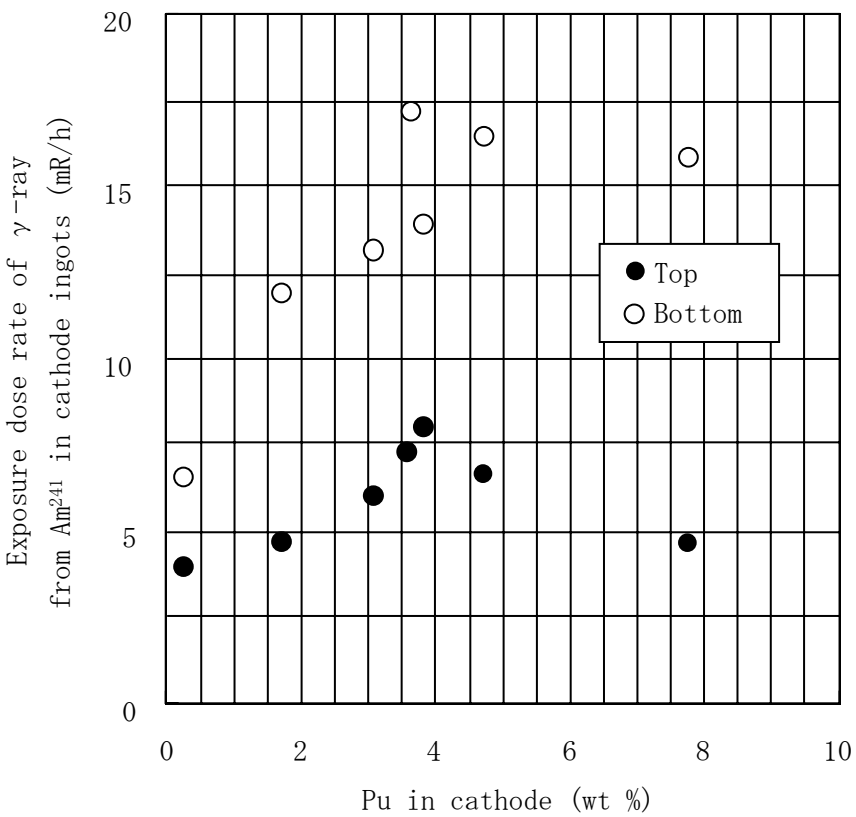

Fig. 4-13 Relation between the Pu concentration in the LCCs and γ-ray from the cathode ingots

Table 4-1 Conditions and results of the Pu electrotransport experiments with LCCs

Run No.	Pu concentration in molten (wt %)	Cathodic current density (mA/cm^2)	Electrotrans-port time (s)	Electricity passed in experiment (C)	Initial amount of cathode (g)	Increase of cathode weight (g)	Collection efficiency (%)	Final Pu concentration in cathode (wt %)
1	2.28	33	12000	240	4.036	0.1983	100	4.68
2	2.11	41	11870	297	2.918	0.245	105	7.75
3	2.28	50	7800	234	4.899	0.1555	80.6	3.08
4	2.11	66	6500	260	3.406	0.0023	1.07	0.07
5	4.6	66	7200	288	4.0287	N/A	N/A	N/A
6	4.6	82	5400	270	4.0056	N/A	N/A	N/A
7	4.6	100	5400	324	4.024	N/A	N/A	N/A
8	4.6	132	5400	432	4.082	N/A	N/A	N/A

$$\text{Collection efficiency (\%)} = \frac{\text{Increase of cathode weight (g)} \times 100}{\text{Total electriccharge (C)} / 1210\ \text{(C/g-Pu)}}$$

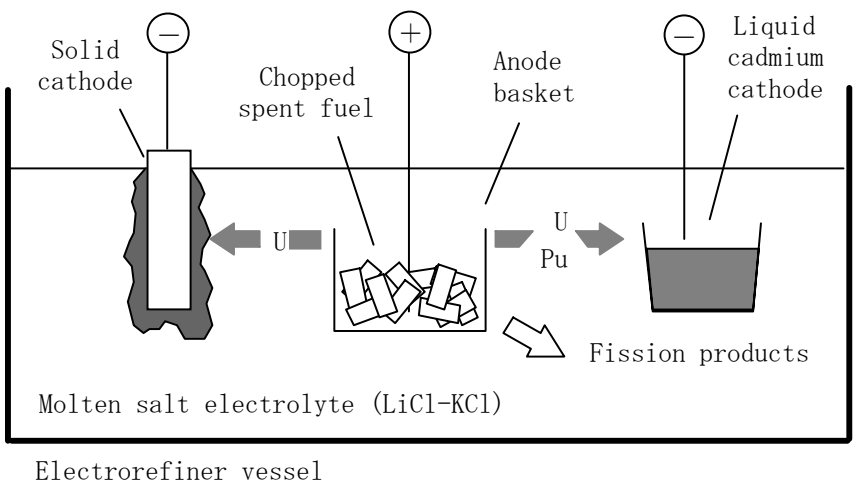

Fig. 4-1 Schematic flow of routine operation of the electrorefining step

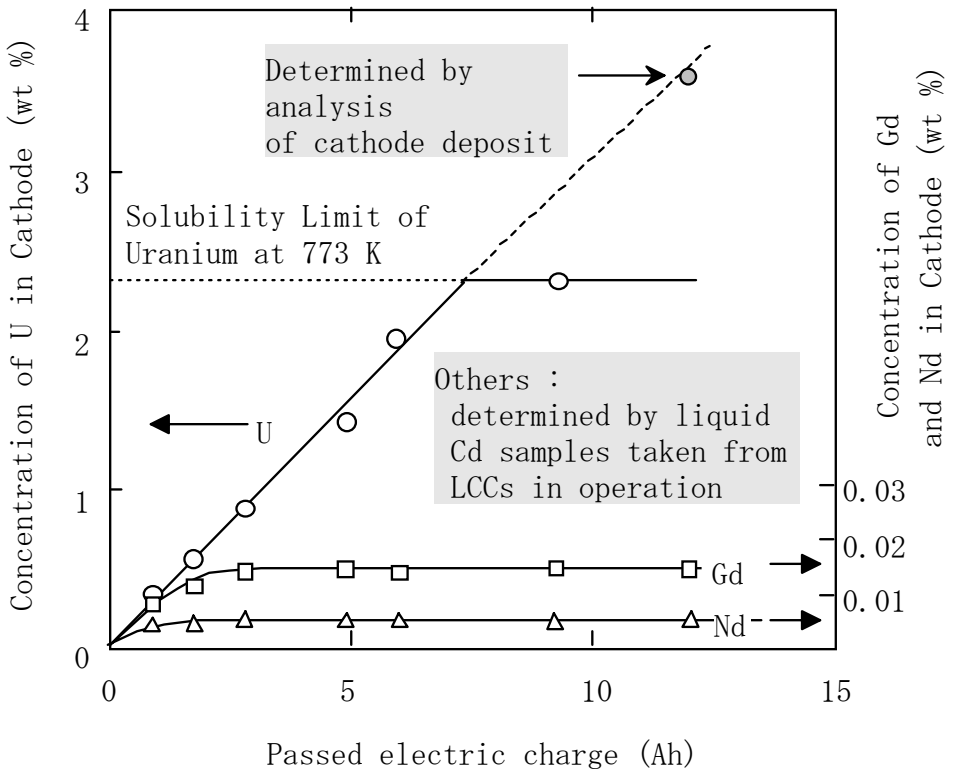

Fig. 4-14 Change of the LCC composition during the electrotransport experiment with uranium, gadolinium and neodymium [18]

Chapter 5 Analyses of anodic behavior of metallic fast reactor fuel using a multi diffusion layer mode

5.1 Background and objectives

As described in Chapter 1 and shown in the previous chapters, the fundamental feasibility of the electrorefining technology and the basic behavior of major elements in this step, such as thermodynamic and electrochemical properties in the molten salt electrolyte, and the collection of the actinides at both the solid and liquid cadmium electrodes has been clarified. To establish the engineering and practical feasibility based on the technical and economical evaluation, however, it is further needed to understand the quantitative relation between the operation conditions and the important performance such as processing rate, recovery rate and decontamination factors. To design the practical equipments and process flow sheet with satisfactory accuracy and reliability, it is also necessary to predict the performance in the electrorefining step by developing proper models of the process and that makes the most of the fundamental data and experimental findings.

Concerning the anodic dissolution of the spent fuel, the most important requirement at present is to determine the operating conditions that maximize the processing rate and dissolution ratio of the actinides. The composition of the metal fuel is basically U-Zr or U-Pu-Zr. Zirconium is added to keep the melting point of the fuels sufficiently high and to lower swelling of them due to irradiation to an allowable level. Since zirconium has a high standard redox potential next to that of uranium, it is inevitable that some part of the zirconium is dissolved with the actinides if uranium in the fuel should be completely removed by anodic dissolution [1, 2].

If zirconium is dissolved from the anode and recovered with uranium at the cathode, it would be advantageous from the viewpoint of reusability as a material of recycled fuel. On the other hand, dissolving zirconium in the electrorefiner should cause the following problems. The dissolved zirconium is reduced again by chemical reaction or cell circuit formation in the electrorefiner, which returns the actinides to the electrolyte again. A considerable part of such re-reduced zirconium would form minute particles of poor adhesion, fall down into the electrolyte, and finally accumulate in the electrorefiner vessel. In that case, zirconium recovery by electrotransport [3] should be periodically conducted, and it probably causes decrease in the processing rate of the electrorefiner throughout a long-term operation. If the anodically dissolved zirconium is recovered with uranium at the solid cathode, higher operation temperature would be required at the cathode processing step, where the electrolyte accompanying the

cathode product is removed and the product is consolidated by high temperature distillation, because the melting point of the cathode product rises as the zirconium content in it is increased. It should then cause great difficulties in development and selection of the process crucible material for the cathode processing. Furthermore, it can be predicted that the high dissolution ratio of zirconium has a negative influence on decontamination against noble metal FPs, since zirconium in the anode residue is considered to trap these FPs in its fibrous structure [2].

As shown above, the anode behavior represented by the zirconium distribution is not only a factor determining the performance of the electrorefining step, but also a subject affecting the design and specification of entire pyrometallurgical reprocessing. In addition, it has a direct influence on the composition and characteristics of metal waste [4] that is principally composed of the anode residue. Detailed investigations on the relation between the operation condition of the electrorefining and the anode behavior is thus of great importance, and a proper calculation model of the anode behavior is an indispensable tool for the pyrometallugical process design.

In our previous report [5], the zirconium layer formed by the dissolution of uranium and plutonium from the ternary alloy was introduced in the anode model as an additional diffusion layer of dissolved actinides. Although this model explained the general tendency of the anode potential change, it could not sufficiently reproduce the precise anode potential value before the commencement of zirconium dissolution. On the other hand, it was found that an intermediate region formed between the inner undissolved alloy and the outer Zr-rich region during anodic dissolution of uranium from the U-Zr alloy [6]. This intermediate region has a composition corresponding to the δ phase (50 - 67 at% Zr). It was also found that a small amount of uranium remained in the Zr-rich region of the anodic residue even after electrorefining for more than 45 hours. In the present study, the anode model was improved incorporating those latest findings so as to be utilized in the investigation on optimized anodic dissolution conditions.

5.2 Layers formation model

5.2.1 Principle in layers formation

In this chapter, it is assumed for simplicity in explanation, if not specified, that the anodic dissolution of alloy and the diffusion of dissolved material progress uniformly only in the axial direction, as schematically shown in Fig. 5-1.

The molten salt diffusion layer is located at the interface between the anode residue and the electrolyte. A linear concentration profile of dissolved actinides in this

layer is assumed according to Nernst's diffusion model.

The anode model developed in this study consists of three layers in the anode residue and a diffusion layer at the molten salt electrolyte side of the anode surface, as shown in Fig. 5-1. Undissolved alloy and porous zirconium layer are located at the central and outer regions of the anodic residue, respectively, similarly to the previous model [5]. In the present model, an intermediate layer that has a composition corresponding to the δ phase (referred to as the δ layer in this report) is added between the above two layers based on the observation of the anode residue [6]. The δ layer, the porous zirconium layer, and the molten salt diffusion layer act as diffusion barriers to the dissolved actinide species.

The δ layer is formed as an intermediate state of anodic dissolution of actinides from the undissolved metal fuel alloys. According to the observation of the anode residues, fine cracks are made in the δ layer by decrease of volume due to a part of the actinides being removed by anodic dissolution. Although these cracks work as a path for diffusion of the dissolved actinides from the undissolved alloy layer, they are very narrow and limited in number. Therefore, the effective diffusion coefficients of dissolved actinide species in this layer are considered to be significantly lower than those in the bulk molten salt electrolyte.

The porous zirconium layer is formed by further dissolution of actinides from the δ layer. The outer diameter of this layer was the same as that of the alloy before anodic dissolution while most of the zirconium was left undissolved [7]. The volume exactly occupied by the zirconium in this layer would be no more than 20 – 30%, which is the estimated volumetric ratio of zirconium in the original alloy. The balance is filled with infiltrating electrolyte salt. The zirconium of such small proportions forms a fibrous or cotton-like microstructure in this layer as shown in Fig. 5-2 [3]. The analytical results showed that the porous zirconium layer still contains a slight amount of uranium even after electrorefining operations for a few days [6]. Although the most part of this residual uranium should be the chloride infiltrated in the fibrous structured layer, there would probably be a very minor amount of metal that is dissolved in zirconium or has poor electric contact with the surrounding materials. Since the porous zirconium layer is located at the external position of the anode residue, the anode potential was assumed to be determined by the local equilibrium in a redox reaction between uranium species at the surface of this layer as follows.

$$
\begin{aligned}
E_{\text{anode}} &= E^{0}_{\text{U/U(III)}} + \frac{RT}{3F}\ln\frac{a\left[\text{U(III)}\right]_{\text{l}}}{a\left[\text{U}\right]_{\text{l}}} \\
&= E^{0}_{\text{U/U(III)}} + \frac{RT}{3F}\ln\gamma_{\text{U(III)}} + \frac{RT}{3F}\ln\frac{X\left[\text{U(III)}\right]_{\text{l}}}{a\left[\text{U}\right]_{\text{l}}} \\
&= E^{0'}_{\text{U/U(III)}} + \frac{RT}{3F}\ln\frac{X\left[\text{U(III)}\right]_{\text{l}}}{a\left[\text{U}\right]_{\text{l}}}
\end{aligned}
\qquad (5\text{-}1)
$$

where

E_{anode} : anode potential (V vs. Ag/AgCl)

$E^{0}_{\text{U/U(III)}}$: standard redox potential of U/U(III) (V vs. Ag/AgCl)

$E^{0'}_{\text{U/U(III)}}$: formal potential of U/U(III) (V vs. Ag/AgCl)

R, T, F : gas constant, temperature (K), Faraday constant

$a\left[\text{U(III)}\right]_{\text{l}}$: activity of U(III) at electrolyte/porous Zr layer interface

$a\left[\text{U}\right]_{\text{l}}$: activity of U at electrolyte/porous Zr layer interface

$\gamma_{\text{U(III)}}$: activity coefficient of U(III) in electrolyte

$X\left[\text{U(III)}\right]_{\text{l}}$: mol fraction of U(III) at electrolyte/porous Zr layer interface

When the actinides are anodically dissolved, these materials are supplied from the undissolved alloy or from the surrounding δ layer.

$$
\begin{aligned}
i_{\text{M}} &= i_{\text{M}}\left(\text{alloy}\right) + i_{\text{M}}\left(\delta\right) \\
&= 3FD_{\text{M in Zr}}\frac{c\left[\text{M(III)}\right]_{2} - c\left[\text{M(III)}\right]_{\text{l}}}{l_{\text{Zr}}} \\
&= 3FD_{\text{M in salt}}\frac{c\left[\text{M(III)}\right]_{\text{l}} - c\left[\text{M(III)}\right]_{0}}{l_{\text{salt}}}
\end{aligned}
\qquad (5\text{-}2)
$$

$$
i_{\text{M}}\left(\text{alloy}\right) = 3F\cdot n_{\text{M,alloy}}\frac{dl_{\text{alloy}}}{dt},\quad i_{\text{M}}\left(\delta\right) = 3F\cdot n_{\text{M},\delta}\frac{dl_{\delta}}{dt} \qquad (5\text{-}3)
$$

where

M : denotes actinide

i_{M} : partial anodic current density by reaction

M = M(III) + $3e^-$ (A/cm^2)

$i_{M}(\text{alloy})$: contribution of M dissolution from undissolved alloy (A/cm^2)

$i_{M}(\delta)$: contribution of M dissolution from δ layer (A/cm^2)

$D_{\text{M in Zr}}$: diffusion coefficient of M(III) in porous Zr layer (cm^2/s)

$D_{\text{M in salt}}$: diffusion coefficient of M(III) in δ layer (cm^2/s)

$c[\text{M(III)}]_0$: concentration of M(III) in bulk electrolyte (mol/cm^3)

$c[\text{M(III)}]_1$: concentration of M(III) at electrolyte/porous Zr layer interface (mol/cm^3)

$c[\text{M(III)}]_2$: concentration of M(III) at porous Zr layer/δ layer interface (mol/cm^3)

l_{Zr} , l_{salt} : thickness of porous Zr layer and molten salt diffusion layers, respectively (cm)

$n_{\text{M, alloy}}$: amount of M in undissolved alloy (mol/cm^3)

$n_{\text{M, }\delta}$: amount of M in δ layer (mol/cm^3)

When the applied current is too large compared with the maximum possible total diffusion fluxes of the actinides passing through the porous zirconium layer as described in equation (5-4), however, the outer surface of the porous zirconium layer is dissolved to compensate for the insufficient fluxes (equation (5-5)).

$$i_{\text{anode}} > \sum_{\text{M}} \left\{ 3FD_{\text{M in Zr}} \frac{Sol_{\text{M}} - c[\text{M(III)}]_1}{l_{\text{Zr}}} \right\} \qquad (5\text{-}4)$$

where

i_{anode} : total anodic current density (A/cm^2)

Sol_{M} : solubility of M(III) in electrolyte (mol/cm^3)

$$i_{\mathrm{Zr}} = i_{\mathrm{anode}} - \sum_{\mathrm{M}} i_{\mathrm{M}} \tag{5-5}$$

where

i_{Zr} : partial anodic current density by reaction Zr = Zr(IV) + 4e$^-$ (A/cm^2)

The maximum possible diffusion flux is determined by the thickness of the diffusion layer, diffusion coefficient of the diffusing actinide and the difference in its concentration across the diffusion layer. The highest concentration of the diffusing actinide is limited to its solubility in molten LiCl-KCl.

When the dissolution rate of the actinide exceeds the maximum possible diffusion flux passing through the δ layer as described in equation (5-6), this actinide is dissolved from the outer surface of the δ layer to compensate for the insufficient flux according to equation (5-7).

$$i_{\mathrm{M}} > \sum_{\mathrm{M}} \left\{ 3FD_{\mathrm{M\,in\,\delta}} \frac{Sol_{\mathrm{M}} - c\left[\mathrm{M(III)}\right]_2}{l_{\delta}} \right\} \tag{5-6}$$

where

$D_{\mathrm{M\,in\,\delta}}$: diffusion coefficient of *M(III)* in δ layer (cm^2/s)

l_{δ} : thickness of δ layer (cm)

$$i_{\mathrm{M}}(\delta) = i_{\mathrm{M}} - i_{\mathrm{M}}(\mathrm{alloy}) \tag{5-7}$$

In all other cases, the actinides are dissolved from the undissolved alloy at the center of the anode residue.

$$i_{\mathrm{M}} = i_{\mathrm{M}}(\mathrm{alloy}) \tag{5-8}$$

After the dissolution processes proceed, the thickness of each layer in the anode residue changes. The thickness of the porous zirconium layer is decreased by anodic dissolution of itself, and increased by the dissolution of the actinides from the δ layer. The δ layer is reduced or grows through the dissolution of the actinides from itself or from the undissolved alloy, respectively. From the results of the observation of

the anode residue sample, it is assumed that the apparent volume of the layers do not change through the transition from initial alloy to the porous zirconium layer.

Although plutonium has a lower standard redox potential than that of uranium, it does not come into contact with the electrolyte until the coexisting uranium begins to be dissolved. In the present anode model, therefore, the anodic dissolution rate of plutonium is assumed to be proportional to that of uranium according to their existing ratio in the undissolved alloy.

The procedure to determine the thickness of each layer is as follows.

(a) The maximum possible diffusion flux of uranium passing through the porous zirconium layer is evaluated from the thickness of both this layer and the molten salt diffusion layer.

(b) If the applied current density exceeds the flux evaluated in (a), the outer surface of the porous zirconium layer is dissolved to compensate for the insufficient flux. The balance corresponds to the uranium dissolution rate from the undissolved alloy or from the δ layer.

(c) The maximum possible diffusion flux of uranium passing through the δ layer is evaluated from the thickness of this layer.

(d) If the uranium dissolution rate calculated in (b) exceeds the flux evaluated in (c), this actinide is dissolved from the outer surface of the δ layer to compensate for the insufficient flux. If not, uranium is dissolved from the undissolved alloy.

(e) The thickness of the layers is adjusted taking account of changes in uranium and zirconium amounts in each layer.

(f) Procedures (a) to (e) are repeated at sufficiently small intervals (around 10 s of electrorefining operation) to avoid unstable behavior due to a significant change of the layers' thickness in a single calculation step.

In the present study, the calculation with the anode model is conducted for the electrorefining tests using U-Zr binary alloy pins chopped after cladding by stainless steel tubes and uncladded U-Pu-Zr ternary alloy pins. In the former case, the exposed area to the electrolyte was limited to the chopped surface. To investigate this type of anode, a ***Planar type*** model is applied, where the dissolved uranium diffuses out only from the chopped section and the dissolution progresses uniformly in the axial direction. In the latter case, the area of the cylindrical side surface is larger than that of the chopped section. To investigate this type of anode, a ***Cylindrical type*** model is

considered, where dissolution and diffusion of uranium occurs uniformly but only in the radial direction.

5.2.2 Parameters in layers formation model

(1) Diffusion coefficients in bulk molten LiCl-KCl electrolyte

The diffusion coefficients of U(III) and Pu(III) in LiCl-KCl around 773K have already been reported [8-10]. Because they are in agreement at approximately $1.0\times10^{-5}cm^2/s$, this value was used in the following calculations. As no report can be found on the diffusion coefficient of Zr(IV) in LiCl-KCl, it was also assumed to be the same as those of U(III) and Pu(III).

(2) Diffusion coefficients in porous Zr layer

As mentioned above, the volume occupied by zirconium in the porous zirconium layer would be no more than 20 – 30%. Although the apparent diffusion coefficients of the actinide ions are readily expected to be lowered due to decrease of free path length, no experimental evidence of such retardation in the diffusion process exists. Therefore, the ratio of diffusion coefficient in this layer to that in bulk LiCl-KCl was assumed to the volume proportion of the electrolyte, 0.7 in the present study for all the elements. In the modeling of U-Zr fuel irradiated in EBR-II [11], decrease of the mass transfer coefficient for the transport of uranium ion across the porous zirconium layer was considered by introducing the tortuosity parameter in the layer. The empirically determined value for the tortuosity was 5.6, corresponding to 0.18 in terms of the ratio of diffusion coefficient in the porous zirconium layer to that in bulk LiCl-KCl. Since this parameter is one of the important factors that determine the starting point for zirconium dissolution at the anode, an exact estimation of it is strongly expected in future.

(3) Diffusion coefficients in δ layer

Since the analyzed composition of the δ layer is 50 - 67 at% Zr [6], approximately 80% of uranium has been removed when transition from the initial U-Zr alloy to the δ layer is completed. Although the δ layer seems still dense at least near the undissolved alloy, fine cracks are made in other regions as mentioned above. Because these cracks are very narrow and limited in number, the apparent diffusion coefficients of dissolved actinides in this layer should be significantly smaller than in the bulk electrolyte. As well as the data in the porous zirconium layer, no diffusion coefficient data in this layer is available. In this study, the ratio between the diffusion

coefficients in this layer and in bulk electrolyte is tentatively determined to be 10^{-3}. Though this parameter directly influences the calculated δ layer thickness, it has only a minor effect on the electrorefiner performance such as the dissolved ratio of uranium and zirconium.

(4) Solubility of actinide chlorides in LiCl-KCl

As mentioned above, the solubility of dissolved actinides in the LiCl-KCl electrolyte is a highly important property that directly influences the maximum possible diffusion rate in the porous zirconium layer. However, there are no reports on determination of either solubility of the UCl_3 or LiCl-KCl-UCl_3 phase diagram. Only a little description, indicating that the solubility limit of UCl_3 in the melt is 50 wt%, can be found in a patent description applied by a researcher of the Argonne National Laboratory [12]. Although no experimental evidence for this value is provided, this value is considered to be reliable from our experiences such as sample preparation and electrorefining. Therefore, the sum of the solubilities of UCl_3 and $PuCl_3$ is tentatively assumed to be 0.15 in mol fraction, corresponding to about 52 wt% of UCl_3 and $PuCl_3$ in the electrolyte, in this study. The LiCl-KCl-$ZrCl_4$ phase diagram has not yet been investigated either. However, it has been reported that the solubility of $ZrCl_4$ in LiCl-KCl at 773 K is 0.013 (in mol fraction), and that $ZrCl_4$ beyond solubility forms a precipitate considered to be K_2ZrCl_6 [13]. This value was used for calculations in this study.

(5) Thickness of molten salt diffusion layer

Concerning the cylindrical iron cathode slowly rotating in molten salt electrolyte, the thickness of the molten salt diffusion layer was estimated using a diffusion layer model [14]. The best agreement is reached between a current-potential curve obtained during the electrorefining tests and the calculated result with the diffusion layer thickness value of 0.025 cm. In the engineering-scale electrorefining tests using U-Zr alloy, which were simulated in the present study, the alloy pins were chopped into a few thousand small pieces and loaded into four anode baskets made of perforated stainless steel plates [2]. This anode differs vastly from the above mentioned iron cathode in both dimension and configuration. However, the major conditions of the electrolyte flow are considered not to differ between these two electrodes, and the same value as shown above is adopted in the following calculations for the engineering-scale tests.

In the small-scale electrorefining tests using U-Pu-Zr alloy, one or two short

pins without cladding were loaded in a small anode basket made of stainless steel mesh. Since this anode stayed still and the stirring of the electrolyte was not so powerful, the molten salt diffusion layer thickness at the surface of the anode in these tests was assumed to be twice as much as that in the engineering-scale tests, i.e. 0.05 cm.

(6) Composition and density of U-Zr, U-Pu-Zr alloys

The composition and density of the binary alloy used in the engineering-scale electrorefining tests were U - 9 wt% Zr and 15.9 g/cm^3, respectively [15]. From these numbers, the molar density of uranium and zirconium in the undissolved alloy can be calculated as 0.0616 mol/cm^3 and 0.0136 mol/cm^3, respectively. The composition of the ternary alloy used in the small-scale tests was U - 19 wt% Pu – 10 wt% Zr [16]. Its density was assumed to be the same as that of the binary alloy. From these numbers, the molar densities of uranium, plutonium and zirconium in the undissolved alloy are calculated as 0.0474 mol/cm^3, 0.0126 mol/cm^3 and 0.0174 mol/cm^3, respectively.

(7) Composition and density of δ layer

The Zr/U ratio in the intermediate layer, located between the undissolved alloy and the porous zirconium layer, found in the anode residue samples ranged from about 1 to 2. In the anode model, however, that ratio was fixed to 2 for simplicity. As mentioned above, the apparent volume of the layers is assumed not to change through the transition from the initial alloy to the δ layer. The density of the δ layer was then calculated as 2.86g/cm^3 from the Zr/U ratio and the density of the initial alloy. The molar density of uranium and zirconium was similarly calculated as 0.00680mol/cm^3 and 0.0136mol/cm^3, respectively.

Regarding the δ layer formed from the U-Pu-Zr alloy, the Zr/(U + Pu) ratio was assumed to be 2 as well, and the molar densities of uranium, plutonium and zirconium were calculated as 0.00688mol/cm^3, 0.00183mol/cm^3 and 0.0174mol/cm^3, respectively.

(8) Composition and density of porous zirconium layer

The apparent volume of the layers is also assumed not to change through the transition from the δ layer to the porous zirconium layer. Regarding the porous zirconium layer formed from the U-Zr alloy, the density and molar density of zirconium were assumed to be 1.24 g/cm^3 and 0.0136mol/cm^3, respectively. Regarding the porous zirconium layer formed from the U-Pu-Zr alloy, the density and molar density of zirconium were assumed to be 1.59 g/cm^3 and 0.0174mol/cm^3, respectively.

(9) Standard electrode potentials

Formal potentials for U(III)/U(0) and Pu(III)/Pu(0), which involve contribution of the activity coefficients in molten salt solvent to the standard electrode potentials, have been determined by the emf measurement [17]. These values versus the Ag/AgCl reference electrode were simply used in the following calculations. Although the standard potential for Zr(IV)/Zr(0) at 773 K has not been reported, it was evaluated from the results of the emf measurements at 723 K and 823 K [18, 19].

(10) Cell resistance in electrorefining test

To discuss the anode potential during electrorefining tests quantitatively, iR drop of the potential due to the cell resistance should be taken into account. Since the cell resistance was not directly measured in the small-scale electrorefining test using ternary alloy [7], it was evaluated by primary current distribution calculation with the recorded information on the dimension of the experimental apparatus and the configuration of the electrodes. It was reported that the cell resistance of the electrorefiner used in the Argonne National Laboratory was evaluated by the same method and that the calculated value was in good agreement with the actual measurement [20]. In the present case, the evaluated cell resistance was about 0.2 Ω and its distribution between the anode and reference electrodes was approximately 0.1 Ω.

(11) Phase segregation in irradiated or annealed alloy

It was reported that U-Zr alloy was segregated into α-U and δ phases by long-term annealing or irradiation at lower than 890 K [21]. In this study, however, the effect of annealing is not considered, since only the as-cast alloys are used in the electrorefining tests under discussion. When anodic behavior of the irradiated fuels is discussed in future, the effect of irradiation and heat treatment on the phase formation should be introduced into the anode model.

The parameter values, which are discussed above and used in the following calculations, are summarized in Table 5-1.

5.3 Calculated result using layers formation model

Using the layers formation model, calculation was conducted on the engineering-scale electrorefining tests E-3 and E-5 [2]. While the details of these tests

have been previously reported, major conditions and results are quoted and shown in Table 5-2. All the U-Zr alloy loaded into the anode baskets in these tests was chopped into small pieces after cladding with stainless steel tubes. The ***Planar type*** model is then used in the following calculations.

Since a large current up to 450 A was applied in these tests, the measured anode and cathode potentials were heavily influenced by the cell resistance. Furthermore, the cell resistance was obviously changed during the run due to accumulation of the cathode deposit. It was therefore concluded that discussion on the anode potential during these tests was impossible.

Spatial current distribution in the anode varied significantly in these tests because the dimension of the anode baskets was so large and each basket contained hundreds of chopped alloy pins. Only qualitative comparison is thus given here between the calculated thickness of the layers and the observation results. The dissolved ratios of uranium and zirconium are quantitatively discussed instead, since these values are derived as the cumulative results of layers formation and also expected to represent the average progress of dissolution in the entire anode.

Figure 5-3 shows the change in the thickness of each layer in the anode residue during Run E-3 calculated by the ***Planar type*** model. When the ***Planar type*** model is used, the thickness or distance in the axial direction of the pins is taken as the Y-axis. Then, the thickness of the undissolved alloy at t = 0 indicates the distance between the chopped section and center of the pin, that is, a half of the chopped length. The current density was evaluated as the applied total current divided by the number of pins in the basket and by the exposed area at both ends, and then factored by the current efficiency that was experimentally determined. The calculation result indicates that the dissolution current for zirconium would begin at a relatively earlier part (about 20,000 s) and that 53.5% of zirconium loaded into the anode would be dissolved at the end of the test. Since practically no zirconium was dissolved in the actual test, it is obvious that the ***Planar type*** model does not give a correct result under the present conditions. For the very early stage of the test, at least, the ***Planar type*** model ought to reproduce the experimental result correctly, since the pins in the anode baskets are cladded by stainless steel tubes. According to the further progress of the anodic dissolution, however, the electrolyte infiltrates into the gap between the pin and cladding, and dissolution began at the cylindrical side face of the pin as shown in Fig. 5-4 [2]. The effective surface area must have been then larger than assumed in the ***Planar type*** model, and the actual current density must have been somewhat lower.

Under such conditions, dissolution of zirconium is delayed since a thicker porous zirconium layer is allowed at lower diffusion flux of the actinides. That is considered to be a reason why the amount of dissolved zirconium in the actual test is much smaller than the calculation result. Since the irradiated fuel alloy is swollen in the radial direction and it is strongly pressed against the cladding, anodic dissolution from the side face would be less significant and the anode behavior of irradiated fuel would be nearer to that expected by the ***Planar type*** model.

The calculation result for Run E-5 is shown in Fig. 5-5. Because the current applied in the early part of this test was more than four times larger than that in Run E-3, the results show that dissolution of zirconium would begin earlier and that 55.1% of zirconium loaded into the anode would be dissolved at the end of the test. In the actual test also, it was confirmed by chemical analysis of the anode residue that 45.8% of zirconium was dissolved, indicating that the ***Planar type*** model reproduced the anode behavior much better for E-5. In E-5, the cladded U-Zr alloy pins were chopped to 5 mm in length, half as much compared with that in E-3. Therefore, the ratio of the side face area to the chopped face was smaller, and the effect of the electrolyte infiltrating between the pin and the cladding should also be smaller than in E-3.

These results reveal that the anodic dissolution of the cladded U-Zr alloy pin progresses preferentially in the axial direction and that the anode behavior estimated by the ***Planar type*** model is in good agreement with the experimental result when the alloy pin is chopped to as short as 5 mm. However, discrepancy between the calculated and experimental results became significant for longer pins because the cylindrical surface of the alloy against the cladding tube, in addition to the chopped section, worked as the anode surface. It is also readily expected that the undissolved region in the anode residue becomes round in shape as the anode dissolution nears completion, while it is simply assumed to become thinner in the ***Planar type*** model. Therefore, extension of the anode model to three-dimensions is required in future in parallel with observation of the irradiated fuels during anodic dissolution to improve the precision in the calculation results.

Figure 5-6 shows the BSE image of the axial section of the anode residue sample obtained after E-5, where the dissolution rate was much lower than those of the other samples in the anode baskets probably due to a geometric disadvantage [6]. In another anode residue sample, the δ layer was found between the outer porous zirconium layer and the undissolved alloy at the center. In the sample shown in Fig. 5-6, however, the porous zirconium layer was not found and EPMA analysis of the

undissolved region indicated the δ phase composition. An attempt was made to reproduce this behavior using the ***Planar type*** anode model under the condition that 20% of the average current density in the test was applied to the sample. The apparent diffusion coefficient in the δ layer was changed to $1.0\times10^{-6}cm^2/s$, a hundred times larger than the reference value, since a large part of the δ layer seen in Fig. 5-6 coheres together and diffusion paths through the electrolyte have been formed to a certain extent. The calculation result is shown in Fig. 5-7. Due to the low applied current density, the dissolution rate of uranium is generally lower than the maximum possible diffusion flux passing through the δ layer. The thickness of the porous zirconium layer, then, quickly reaches saturation and the transition from the undissolved alloy remains at δ layer formation. This result is in good agreement with the observation in Fig. 5-6, indicating the validity of the anode model.

5.4 Calculation of anode potential

Calculation using the anode model was also conducted on the small-scale electrorefining tests where around 10 g of U-Pu-Zr ternary alloy were used. Although the details of these tests have been previously reported [7, 22, 23], major conditions and results are grasped and shown in Table 5-3. The U-Pu-Zr alloy loaded into the anode baskets in these tests was in the form of uncladded pins 0.48 cm in diameter and a few centimeters in length. Since the area of the side face was larger than that of the chopped sections, the ***Cylindrical type*** model was used in the following calculations. In these tests, the cell resistance must have been stable all the way, since the amount of electrotransported materials was very small compared with the dimension of the electrorefiner. Then, in addition to the layer formation, the anode potential was estimated and compared with the experimental results in the following calculations.

5.4.1 Procedure of anode potential calculation in the present model

In the present model, the anode potential is determined from the local redox equilibrium involving uranium species at the outer surface of the anode (surface of the porous zirconium layer, in most cases) as shown in equation (5-1). Concentrations of U(III) and Zr(IV) at the porous zirconium layer/molten salt diffusion layer interface are calculated in the layer formation model described in II.1. Activity of Zr at the surface of the anode was assumed to be unity.

In calculation of the layer formation, the porous zirconium layer was assumed to contain no actinides. According to the EPMA analytical results of the anode residue samples, however, it was found that a small amount of uranium remained in this region

even after electrorefining for more than 45 hours [6]. Although the most part of the remaining uranium should be the chloride infiltrated in the fibrous structured layer, there would probably be a very minor amount of metal that was dissolved in zirconium or has poor electric contact with the surrounding materials. While the porous zirconium layer was growing, the anode potential stayed at too low a value for zirconium to be dissolved [7]. If uranium had been completely removed from the porous zirconium layer, the anode potential should have jumped to a much higher level which could be explained from equilibrium involving only the zirconium species. All these results and discussion lead us to conclude that a very small amount of uranium metal exists in the porous zirconium layer, at least until significant zirconium dissolution commences.

In the present study, then, the activity of uranium in the porous zirconium layer is assumed to decrease exponentially to the layers' thickness. Its lower limit is not exactly zero, but a certain positive value *m* independent of other conditions. Finally, uranium activity at the surface of the porous zirconium layer is expressed as follows.

$$a[\mathrm{U}]_{\mathrm{I}} = m + e^{-bl_{Zr}} \tag{5-9}$$

5.4.2 Formulation of uranium activity in the porous zirconium layer by experimental conditions

It is obvious that the principal factor determining the thickness of the porous zirconium layer is the electric charge passed per anode surface area, since this layer is produced by electrochemical removal of the actinides from the spent fuel alloy. The other factors such as current density, δ layer formation and shape of the anode may have a certain influence. Figure 5-8 shows the relation between the thickness of the porous zirconium layer and the electric charge at various current densities for a U-Pu-Zr ternary alloy pin 0.48 cm in diameter, which is calculated using the ***Cylindrical type*** anode model. The calculation was conducted until the ratio of the zirconium dissolution current to the total anodic current reached 10%. At the current density of 40 mA/cm^2 or higher, this relation does not essentially depend on the current density and the thickness of the porous zirconium layer is approximately in proportion with and the total electric charge. At 20 mA/cm^2 or lower, on the other hand, the thickness of the porous zirconium layer obviously decreases with the current density, indicating that the current is used for formation of thicker δ layer as experimentally observed at very low current density (Fig. 5-6).

The relation between the porous zirconium layer thickness and initial diameter of the alloy estimated at a constant anodic current density is shown in Fig. 5-9. Since a smaller diameter gives larger thickness of the inner diameter of the porous zirconium layer with the same electric charge, the plot deviates to the upper direction according to the decrease of the initial alloy diameter. This effect is, however, not as significant as that of current density. It is not likely either that the diameter of fuel is altered as dramatically as shown in Fig. 5-9. After all, there is no need to give serious consideration to the influence of the fuel diameter on the thickness of the zirconium layer.

To summarize, the thickness of the porous zirconium layer cannot be expressed using the electric charge alone, or additionally taking account of the current density and anode configuration. The situation would be more complicated in the case where the current density is changed during the electrorefining operation. In the following calculations of the anode potential, then, the thickness of the zirconium layer is treated not as a function of experimental variables like current density and operated period, but simply as a calculation result obtained by the layers formation model. Under a limited condition (i.e. at the current density of 60 mA/cm^2 or higher), however, it can be approximated to be proportional to the electric charge as shown in Fig. 5-8.

5.4.3 Calculated result for electrorefining test using U-Pu-Zr ternary alloy

In equation (5-9) that gives uranium activity at the surface of the porous zirconium layer used in the anode potential calculation, there are two parameters *a* and *m* to be determined.

Three runs of laboratory-scale electrorefining tests were simulated with various values for these parameters using the ***Cylindrical type*** anode model. Comparison between the calculated anode potential and the experimental data showed that a combination of b = 8,000 and m = 2.0×10^{-4} gives the best agreement. The calculated anode potentials with these parameters is shown in Figs. 5-10 to 5-12 with the experimental data. The electric charge passed between the electrodes and the thickness of the layers in the radial direction of the pins are taken as the X- and Y-axes, respectively.

The calculation result finely reproduces the characteristics of the anode potential observed during Run-2, such as the rapid rise at the beginning and near the end, and the plateau between them (Fig. 5-10). The rise of potential at the beginning of the test is caused by growth of the δ and porous zirconium layers. While the thickness of the porous zirconium layer continues to increase even after the initial anode

potential rise, uranium activity approaches its lower limit (m = 2.0×10^{-4}) and its influence on the anode potential quickly becomes moderate. The second sudden increase of the anode potential is due to the fact that the concentration of U(III) in the porous zirconium layer reaches its solubility and that this layer is dissolved to maintain the anodic current density.

Run-3 was conducted at a higher anodic current density than in Run-2. The tendency of the anode potential change is well reproduced also for this test (Fig. 5-11). In the practical experiment, some distribution of the current density in the anode inevitably occurs dependent on the configuration of electrodes or the conditions of alloy retention in the anode basket. This inhomogeneity should be more significant at a higher current density. Since the progress of anodic dissolution and the layers formation is not uniform over the anode in such situation, it is possible that some part of the anode surface, where a thick porous zirconium layer has formed preferentially to the other parts, influenced the actual anode potential at the plateau part to be slightly higher than the calculated value.

The lowest anodic current density in these three runs was applied in Run-9. The overall trend in the anode potential is satisfactorily reproduced for this test as well as the other two runs mentioned above (Fig. 5-12). One notable point found in common with all the three tests presented here is that the actual anode potential continued to increase slowly at the period between two rapid rises, while the calculated anode potential remains constant in the same period. Although the cause of this disagreement is unclear at present, a few possibilities can be mentioned. One is that there was some inhomogeneity or distribution of the porous zirconium layer thickness at the anode surface. The actual anode potential is considered to be determined by a statistically representative value of this thickness distribution that should gradually increase until zirconium begins to dissolve. Another possibility is that the parameter m in equation (5-9) slightly changes during the test. According to the U-Zr binary phase diagram [24], m could be interpreted as an activity of uranium dissolved in the solid α-Zr. The amount of uranium allowed in this phase seems very small, and its diffusion coefficient must also be very low. However, its concentration at the surface, which determines the electrochemical potential, might possibly be decreased by long-term anodic dissolution.

5.5 Utilization of anode model for determination of operation conditions

The above results of the tests and calculations clarify that the maximum available anodic current density restraining the dissolution of zirconium is limited by

the thickness of the porous zirconium layer in most cases. It is obvious that the throughput of the electrorefiner reaches a peak when the above maximum current density is maintained throughout the operation, if no limit is imposed by the actinide reduction rate at the cathode. In the following, the influence of some conditions on the anodic dissolution rate is evaluated using the anode model developed in this study. For simplicity's sake, the dissolved anode pin under consideration was limited to cladded U-Zr alloy, and the ***Planar type*** anode model is assumed to be applicable in all cases. A value of 5 mm was chosen as the reference length of the pin.

Change of the current density and the thickness of each layer in an ideal case where the current density was maintained at its maximum possible value without zirconium dissolution are shown in Fig. 5-13. At the initial part of the electrorefining, the current density is drastically decreased according to the growth of the porous zirconium layer. Since decrease in the current density means nothing but decrease in the development rate of the porous zirconium layer, the change of the current density becomes much slower at the latter stage. The time required until the remaining ratio of uranium reaches 1% was evaluated as about 19.4 h.

5.5.1 Influence of current-control program on processing rate and dissolved ratio of Zr

Since it is impractical to control the current density at the maximum permissible value at every moment in the electrorefining operation, the calculation was conducted in a case where the current density was lowered stepwise under control to prevent dissolution of zirconium. The result is shown in Fig. 5-14. In this case, the anodic dissolution rate does not exceed the maximum possible throughout the operation. The time required until the remaining ratio of uranium reaches 1% is evaluated as about 23.5 h, which is about 21% larger than the ideal case shown above. To practically perform such control closely adjusted to the ideal situation, accurate prediction of the anodic behavior and more rapid detection of anode potential are necessary.

There is a possibility that the anodic dissolution rate would be increased by allowing a certain degree of zirconium dissolution and its entrainment into the cathode product. Various patterns for the current density control are considered to realize such a condition. One example case is calculated here, where an anodic current density is always maintained at 5% larger than the maximum permissible value without zirconium dissolution. By applying the excess current density averaged through the total duration of operation, a definite ratio of zirconium dissolution current to total anodic current is expected and eventually more uniform cathode deposit composition

would be obtained. The calculation result is shown in Fig. 5-15. The time required until the remaining ratio of uranium reaches 1% is evaluated as about 16.6 h, which is about 15% less than the ideal case. The dissolution ratio of zirconium under this condition is estimated as 17.5%. When the anodic current density is further increased to 10% larger than the maximum allowed value to avoid zirconium dissolution, the turnaround time is reduced by 30% while the zirconium dissolution rate is increased by 34.4%. Although there is a merit of reduction in the processing time by increasing the anodic current density, it leads to co-dissolution of a considerable amount of zirconium at the same time, which will cause problems not only in the electrorefining step, but also in the cathode processing step and metal waste treatment as mentioned in the introduction. In determining the operation parameters in the anodic dissolution, therefore, those influences on the overall pyrometallurgical processing flow sheet should be carefully taken into consideration.

5.5.2 Influence of chopped length of spent fuel alloy on processing rate and dissolved ratio of Zr

In the ***Planar type*** anode model, the longer the chopped length of the alloy pins, the longer the processing time for anodic dissolution, since the anodic dissolution begins at the chopped face and progresses in the axial direction. The dissolution rate is further decreased according to the porous zirconium layer thickness due to the decline in the diffusion flux through this layer. This tendency is shown in Fig. 5-16. As the chopped length of the pin is increased, the time required to attain the uranium remaining ratio of 1% rises sharply. In order to obtain the same dissolution rate with longer pins, a greater amount of zirconium needs to be dissolved. Although 0.25 cm is not exactly a realistic length into which the spent fuels are chopped from the technical point of view, it seems necessary to achieve as short as 0.5 cm to dissolve the uranium almost completely within a day without significantly dissolving zirconium. Concerning the problems coming from the electrolyte flow through the piled chopped pins and the current distribution in a larger scale anode, additional studies from the standpoint of engineering are required.

In actual situations, the anodic dissolution does not progress only in the axial direction of the chopped pins, and the undissolved region may shrink also in the radial direction. The change of the surface area of the undissolved alloy and that of the effective thickness of the porous zirconium layer should heavily affect the anode behavior. To investigate this influence and to improve the precision in the calculation of anode behavior, it is highly important in future to observe the irradiated fuels during

anodic dissolution, and to extend the anode model to a three-dimensional system.

5.6 Conclusions

The anodic behavior of U-Zr or U-Pu-Zr alloys during electrorefining in molten chloride electrolyte was modeled taking account of recent findings from the observation of anode residues after a number of electrorefining tests, such as formation of an intermediate region that has a composition corresponding to the δ phase. In this model, a multi-layered structure consisting of the undissolved alloy, δ phase composition layer and porous zirconium layer is formed according to anodic dissolution of actinides. The succeeding anode reaction and its location are determined from the limiting diffusion rate of dissolved actinides in three diffusion layers. To calculate the anode potential based on the local equilibrium of uranium at the surface of the anode residue, exponential distribution of uranium activity in the porous zirconium layer was assumed.

Simulation of anodic dissolution of the U-Zr alloy during the engineering-scale electrorefining tests using the model showed that calculated dissolution ratios of uranium and zirconium, which are directly affected by the multi-layer formation, were in agreement with the experimental result when the alloy pin is chopped to as short as 5 mm. However, discrepancy between the calculated and experimental results became significant for longer pins because the cylindrical surface of the alloy against the cladding tube, in addition to the chopped section, worked as the anode surface. Growth of the thick δ layer found in the anode residue sample was also explained by simulating the local anode behavior at lower anodic current density than the average value.

Three runs of laboratory-scale electrorefining tests with uncladded U-Pu-Zr ternary alloy were also simulated. The characteristic change of anode potential during these tests was finely reproduced in the calculation by fitting parameters for uranium activity in the porous zirconium layer. The distribution of the porous zirconium layer thickness at the surface of the anode or the slight decrease of uranium dissolved in solid α-Zr could be a cause of the disagreement found between the experimental and calculation results, such as the gradual increase of the actual anode potential.

After the validation and optimization of parameters, exploratory calculations were conducted to investigate the effect of the current-controlling pattern and length of chopped alloy pins on the anodic dissolution rate and zirconium dissolution ratio. The results showed that the required period to attain a certain uranium dissolution ratio would be drastically increased with increase in pin length, and that the zirconium

dissolved ratio would be largely increased when a higher anodic current density is applied to improve the electrorefining processing rate.

To improve the precision in the calculation of anode behavior, remaining important subjects are exact estimation of the solubility of the actinides in molten salt electrolyte and the diffusion coefficients in the porous zirconium layer, observation of the irradiated fuels during anodic dissolution, and extension of the anode model to a three-dimensional system.

References

[1] S. X. Li, "Anodic process of electrorefining spent nuclear fuel in molten LiCl-KCl-UCl_3/Cd system", *Proc. 201st Meeting of the Electrochemical Society, 13th International Symposium on Molten Salts*, Philadelphia, PA, May 12-17, 2002.

[2] M. Iizuka, K. Uozumi, T. Ogata, T. Omori and T. Tsukada, “Development of an innovative electrorefiner for high uranium recovery rate from metal fast reactor fuels”, *J. Nucl. Sci. Technol.*, **46**, 699–716 (2009).

[3] S. X. Li, T. A. Johnson, B. R. Westphal, K. M. Goff and R. W. Benedict, "Electrorefining experience for pyrochemical processing of spent EBR-II driver fuel", *Proc. GLOBAL 2005*, Tsukuba, Japan, Oct. 9-13, 2005,.

[4] D. D. Keiser, Jr. and B. R. Westphal, "Consolidation of cladding hulls from the electrometallurgical treatment of spent fuel", *Proc. 3rd Topical Meeting DOE Spent Nuclear Fuel and Fissile Materials Management*, Charleston, SC, Sep. 8-11, 1998.

[5] M. Iizuka, K. Kinoshita and T. Koyama, “Modeling of anodic dissolution of U-Pu-Zr ternary alloy in the molten LiCl-KCl electrolyte”, *J. Phys. Chem. Solids*, **66**, 427-432 (2005).

[6] M. Iizuka, T. Omori and T. Tsukada, “Behavior of U-Zr alloy containing simulated fission products during anodic dissolution in molten chloride electrolyte”, *J. Nucl. Sci. Technol.*, *to be published*.

[7] K. Kinoshita, T. Koyama, T. Inoue, M. Ougier and J.-P. Glatz, “Separation of actinides from rare earth elements by means of molten salt electrorefining with anodic dissolution of U-Pu-Zr alloy fuel”, *J. Phys. Chem. Solids*, **66**, 619-624 (2005).

[8] L. Martinet and F. Caligara, “Electrochemistry of actinides in molten salts”, *At. Energy Rev.*, **11**, 3-61 (1973).

[9] P. Masset, R. J. M. Konings, R. Malmbeck, J. Serp and J.-P. Glatz,

"Thermochemical properties of lanthanides (Ln = La, Nd) and actinides (An = U, Np, Pu, Am) in the molten LiCl–KCl eutectic", *J. Nucl. Materials*, **344**, 173-179 (2005).

[10] S. A. Kuznetsov, H. Hayashi, K. Minato and M. Gaune-Escard, "Electrochemical transient techniques for determination of uranium and rare-earth metal separation coefficients in molten salts", *Electrochem. Acta.*, **51**, 2463-2470 (2006).

[11] R. Ahluwalia, T. Q. Hua and H. K. Geyer, "Behavior of uranium and zirconium in direct transport tests with irradiated EBR-II fuel", *Nucl. Technol.*, **126**, 289-302 (1999).

[12] J. Willit, U.S. patent 7267754, 2007.

[13] Y. Sakamura and T. Inoue, *Proc. 5th Topical Meeting on DOE Spent Nuclear Fuel and Fissile Materials Management*, Charleston, SC, Sep. 17-20, 2002.

[14] T. Kobayashi, R. Fujita, M. Fujie and T. Koyama, "Polarization effects in the molten salt electrorefining of spent nuclear fuel", *J. Nucl. Sci. Technol.*, **32**, 653-663 (1995).

[15] T. Ogata and T. Tsukada, "Engineering-scale development of injection casting technology for metal fuel cycle", *Proc. GLOBAL 2007*, Boise, Idaho, Sp. 9-13, 2007.

[16] M. Kurata, A. Sasahara, T. Inoue, M. Betti, J.-F. Babelot, J.-C. Spirlet and L. Koch, "Fabrication of U-Pu-Zr metallic fuel containing minor actinides", *Proc. GLOBAL 97*, Yokohama, Japan, Oct. 5-10, 2007.

[17] J. Roy, L. Grantham, D. Grimmett, S. Fusselman, C. Krueger, T. Storvick, T. Inoue, Y. Sakamura and N. Takahashi, "Thermodynamic properties of U, Np, Pu and Am in molten LiCl-KCl eutectic and liquid cadmium", *J. Electrochem. Soc.*, **143**, 2487-2492 (1996).

[18] T. Suzuki, "Equilibrium between zirconium and its chlorides in LiCl-KCl eutectic melt", *Denki Kagaku*, **39**, 864-867 (1971).

[19] R. Baboian, D. L. Hill and R. A. Bailey, "Electrochemical studies on zirconium and hafnium in molten LiCl-KCl eutectic", *J. Electrochem. Soc.*, **112**, 1221-1224 (1965).

[20] T. Kobayashi, M. Tokiwai and E. C. Gay, "Investigation of cell resistance for molten salt electrorefining of spent nuclear fuel", *J. Nucl. Sci. Technol.*, **21**, 68-74 (1995).

[21] G. L. Hofman, R. G. Pahl, C. E. Lahm and D. L . Porter, "Swelling behavior of U-Pu-Zr fuel", Metallurgical Trans. A, 21A, 517-528 (1990).

[22] T. Koyama, K. Kinoshita, T. Inoue, M. Ougier, G-P. Glatz and L. Koch, *Proc. GLOBAL 2001*, Paris, France, Sep. 8-12, 2001.

[23] T. Koyama, K. Kinoshita, T. Inoue, M. Ougier, R. Malmbeck, J-P. Glatz and L. Koch, “Study of molten salt electrorefining of U-Pu-Zr alloy fuel”, *J. Nucl. Sci. Technol.*, Supplement 3, 765-768 (2002).

[24] T. B. Massalski ed., "Binary Alloy Phase Diagrams", ASM International, 1990.

Table 5-1 Parameters and properties used in analysis of anode behavior

		U(III)	Pu(III)	Zr(IV)
Diffusion coeffcient (cm^2/s, at 773 K)	in bulk LiCl-KCl	1.0×10^{-5}		
	in porous Zr layer	0.7×10^{-5}		-
	in δ layer	1.0×10^{-8}	-	-
Solubility in LiCl-KCl (mol frac., at 773 K)		0.15 in total [20]		0.013 [21]
Standardl redox potential (at 773 K)		-1.25 [25]	-1.55 [25]	-0.85 [26]

	U-Zr	U-Pu-Zr
Density (g/cm^3)	15.9 [23]	15.9
Comopsition (wt. %)	Zr : 9 wt. % U : balance [23]	Pu : 19 wt. % Zr : 10 wt. % U : balance [24]
Diameter (cm)	0.29 [23]	0.24 [24]
Cladding	Stainless-steel	-
Molar density (mol/cm^3)	U : 0.0616 Zr : 0.0136	U : 0.0474 Pu : 0.0126 Zr : 0.0174

Molar volume (cm^3/mol)		33.7
Thickness of diffision layer (cm	Engineering-scale tests using U-Zr	0.025
	Small-scale tests using U-Pu-Zr	0.050

Table 5-2 Major conditions and results of engineering-scale electrorefining tests [2]

	Run E3	Run E5
Amount of alloy loaded in anode (kg)	U-Zr : 7.72	U-Zr-FP (*1) : 7.07
nitial concentration of U in electrolyte (wt. %)	1.68	2.05
Current (A)	100 → 10	450 → 5
Total electric charge (Ah)	2945	3510
Amount dissolved from anode (kg)	U : 6.342 Zr : - (*2)	U : 6.091 Zr : 0.324
Anodic current efficiency (%)	72.8	58.6
Amount collected at cathode (kg)	U : 7.421 Zr : 0.0877	U : 5.934 Zr : 0.329
Cathodic current efficiency (%)	88.6	57.1
Recovery rate (g-U/h·litter-electrodes)	9.6	32.9

(*1) Zr : 9.00 wt. %, Mo : 1.06 wt. %, Pd : 0.59 wt. %, Ce : 0.04 wt. %, Nd : 0.04 wt. %

(*2) not determined due to large error in evaluation of electrolyte content in anode residue

Table 5-3 Major conditions and results of small-scale electrorefining tests [7,22,23].

	Run-2	Run-3	Run-9
Amount of alloy loaded in anode (g)	13.2	14.9	4.59
Initial composition of electrolyte (wt. %, initial/final)	U : 0 / 0.19 Pu : 3.5 / 3.4 Zr : 0 / 0	U : 0 / 0.19 Pu : 3.5 / 3.4 Zr : 0 / 0	U : 0 / 0.19 Pu : 3.5 / 3.4 Zr : 0 / 0
cathode	liquid Cd (84.4 g)	liquid Cd (77.8 g)	liquid Cd (75.9 g)
Current (A)	0.4	0.7	0.1
Anodic current density per cylindrical side surface area (A/cm^2)	0.057	0.089	0.041
Total electric charge (C)	8100	10220	3800
Amount of cathode deposit (g)	90.8	77.8	NA
Composition of cathode deposit (wt. %)	U : 0.62 Pu : 6.0 Zr : 0.003	U : 1.9 Pu : 6.0 Zr : 0.006	U : 0.95 Pu : 1.8 Zr : 0.004
Cathodic current efficiency (%)	90	77	67

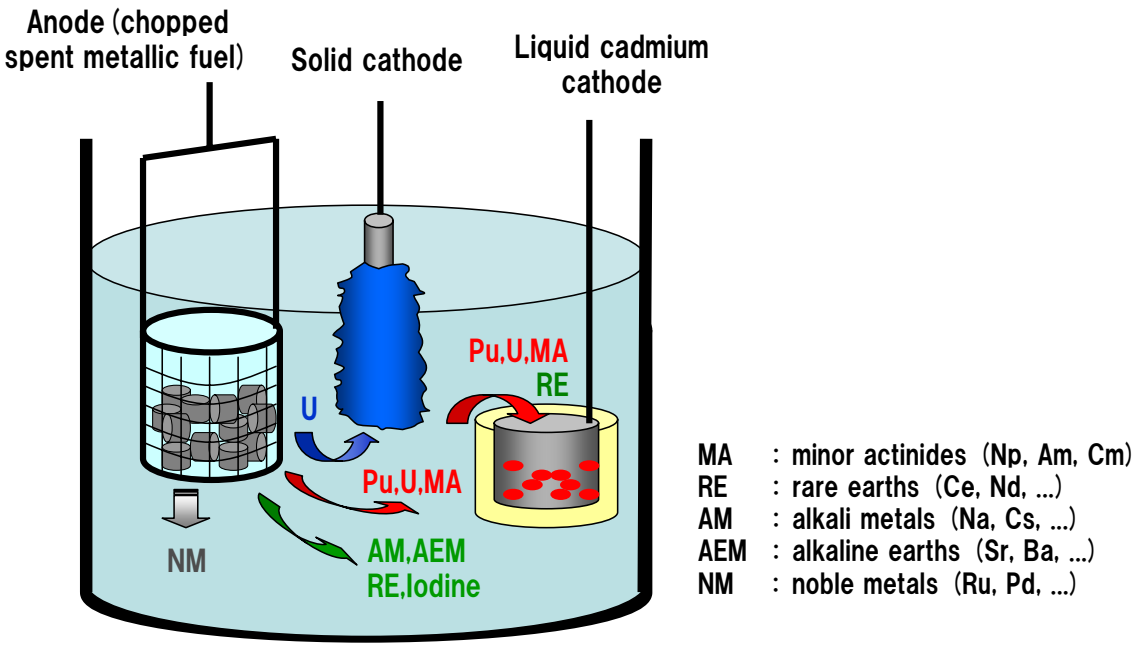

Fig. 5-1 Schematic diagram of electrorefining step for spent metallic fuel

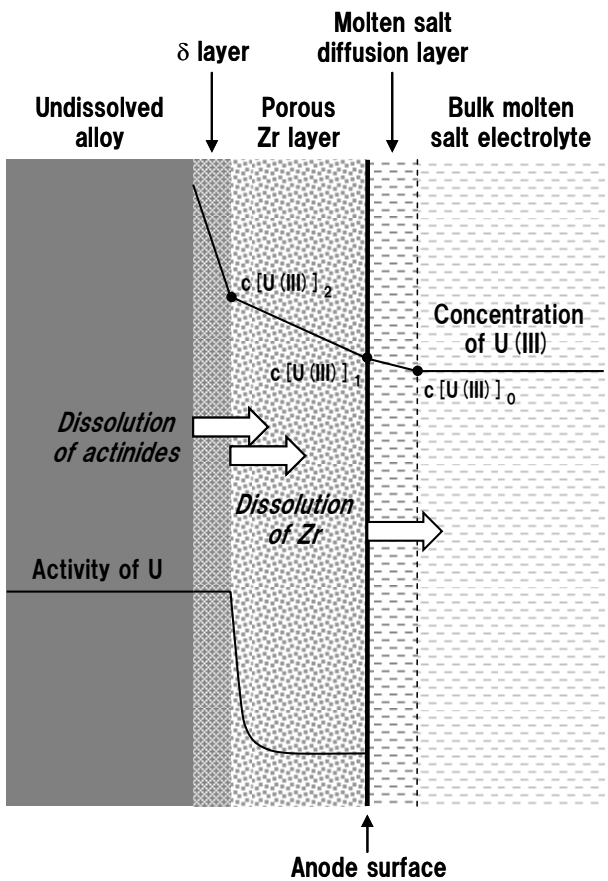

Fig. 5-2 Schematic view of anode model in this study

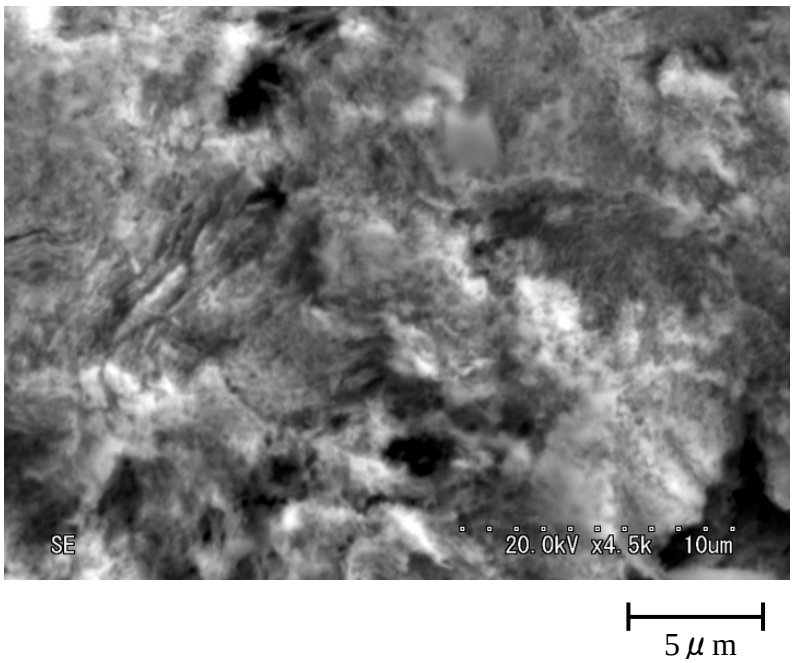

Fig. 5-3 Microstructure of remaining zirconium in anode residue [2]

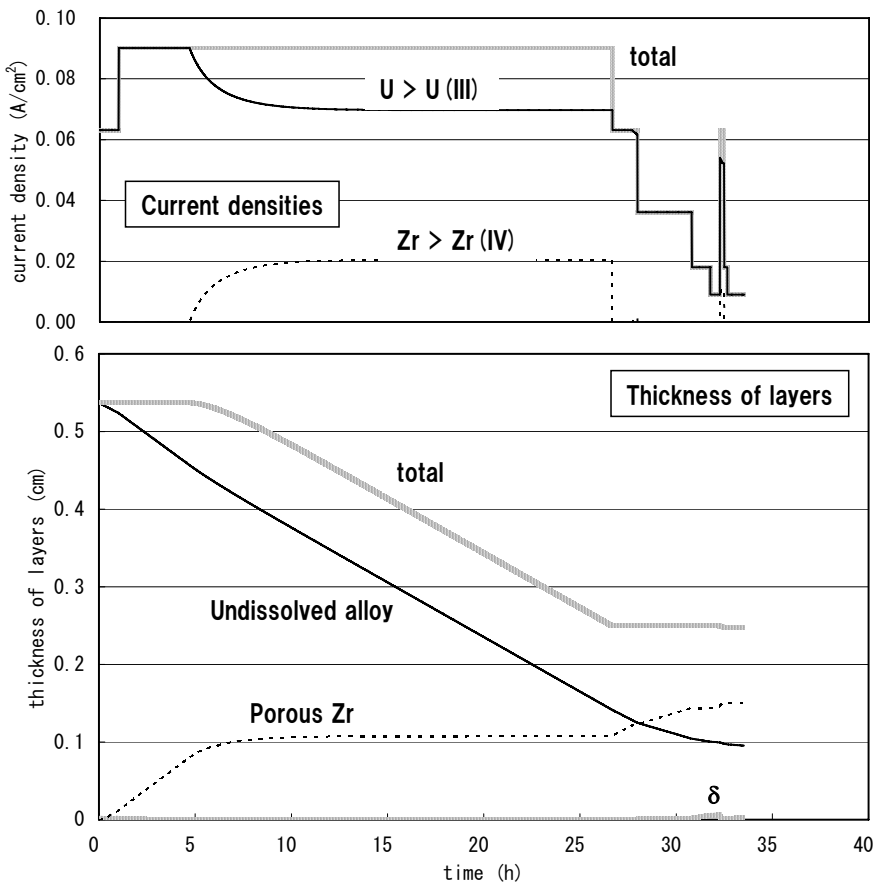

Fig. 5-4 Change in partial current densities and thickness of layers in anode residue during Run E-3 calculated by planar type anode model

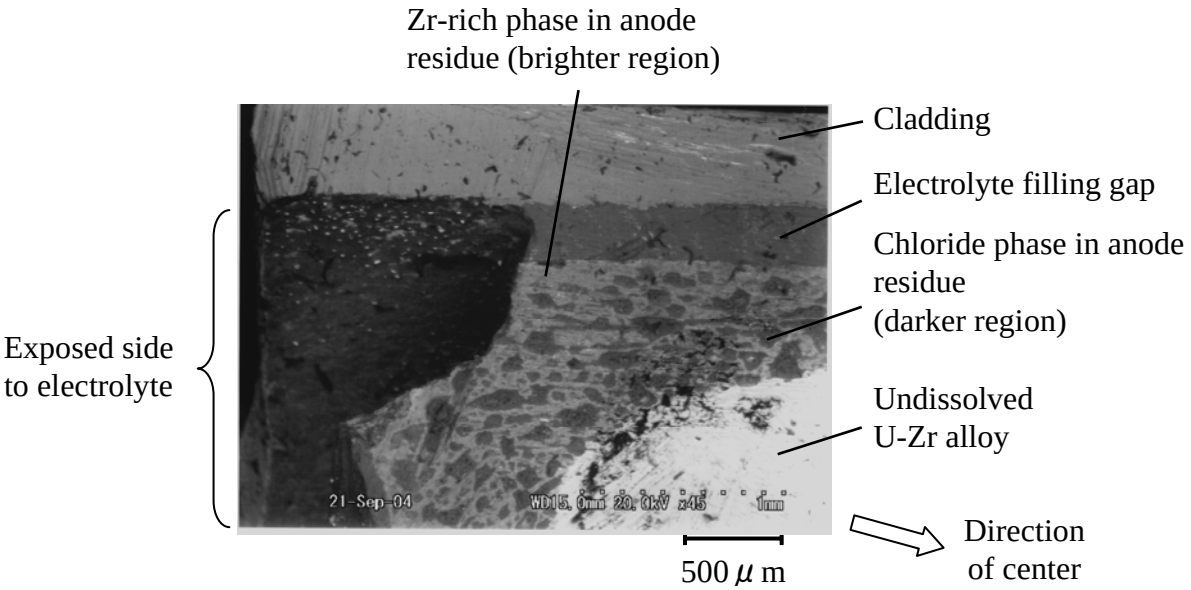

Fig. 5-5 BSE image of sectioned anode residue

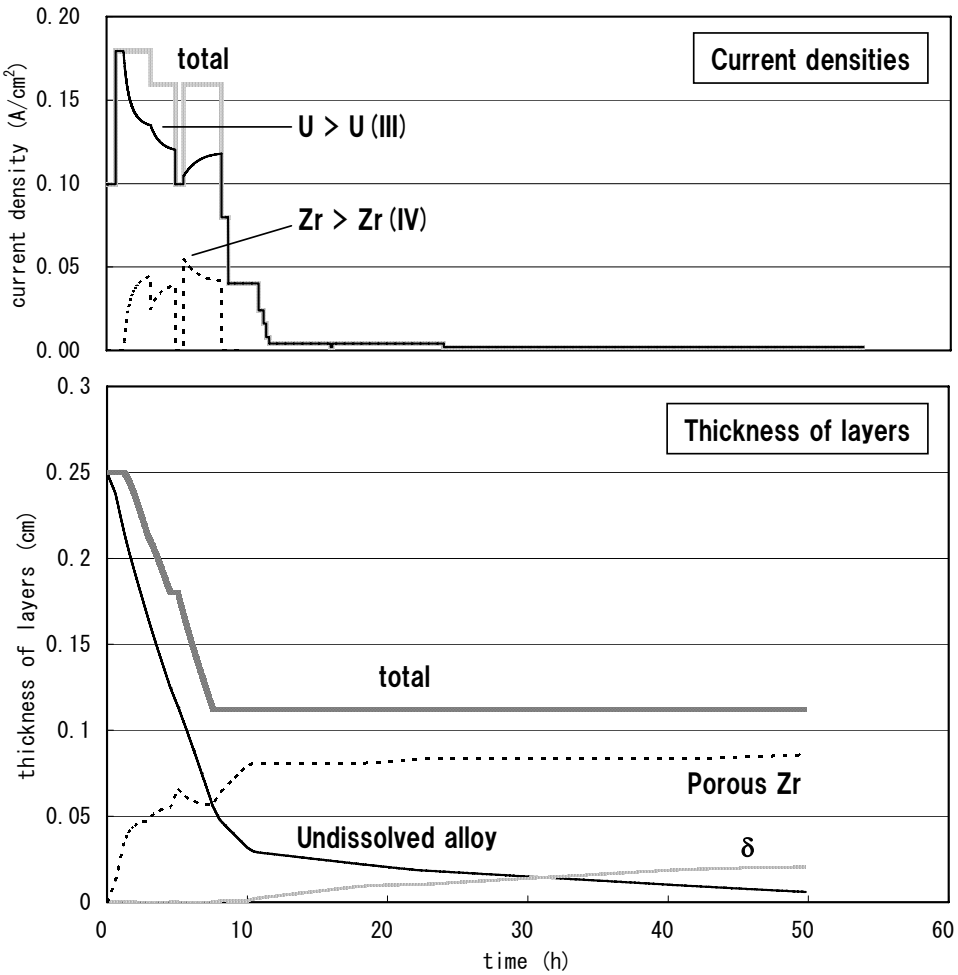

Fig. 5-6 Change in partial current densities and thickness of layers in anode residue during Run E-5 calculated by planar type anode model

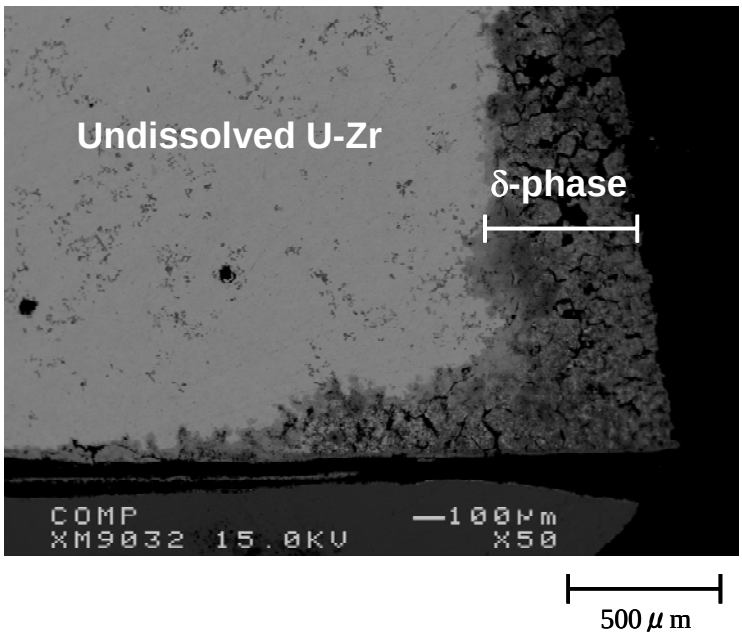

Fig. 5-7 BSE image of axially sectioned anode residue where dissolution rate was much lower than other part [6]

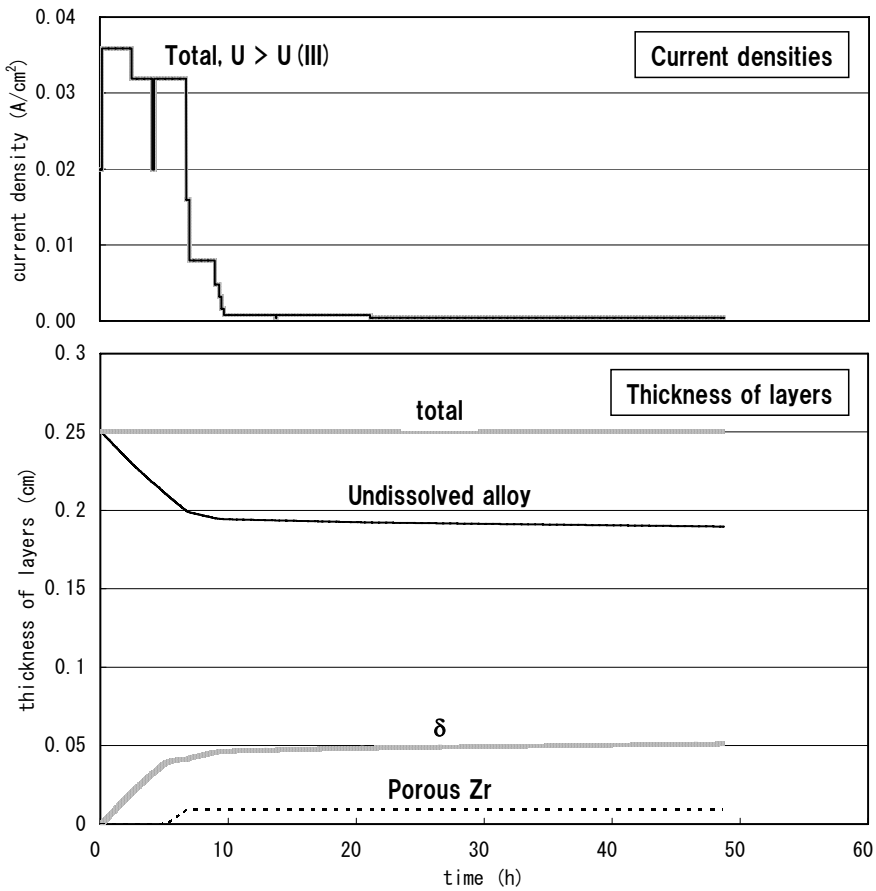

Fig. 5-8 Change in partial current densities and thickness of layers in anode residue at lower current density than the average value

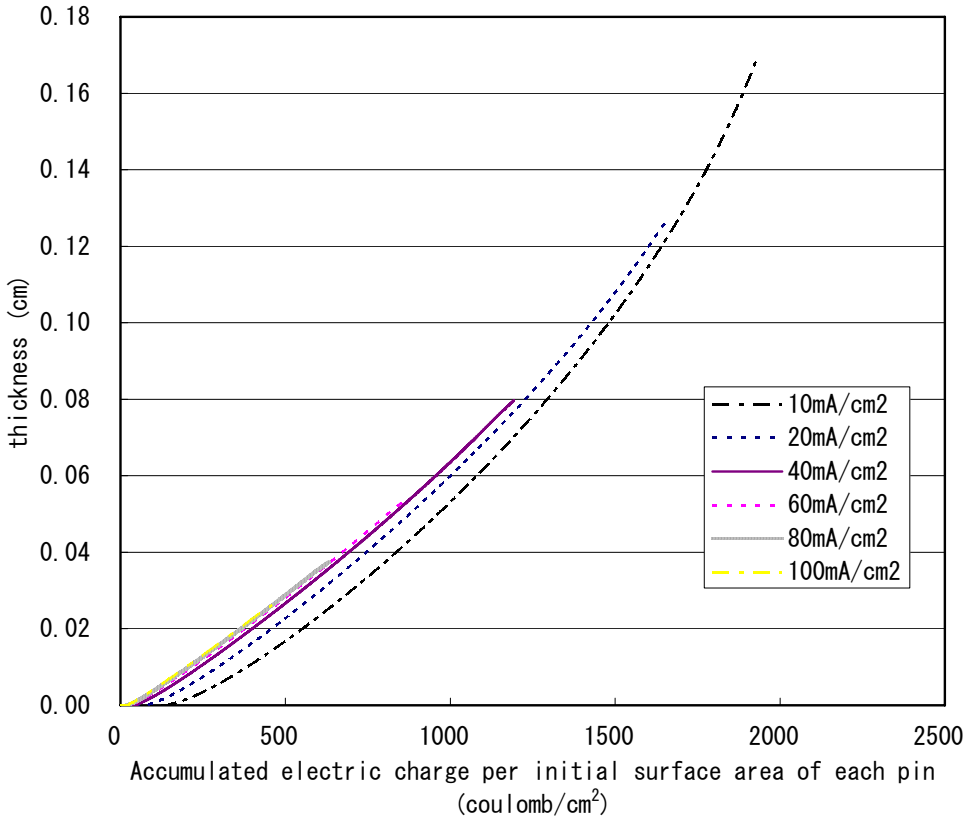

Fig. 5-9 Relation between thickness of porous zirconium layer and electric charge for a U-Pu-Zr ternary alloy pin calculated using the cylindrical type anode model

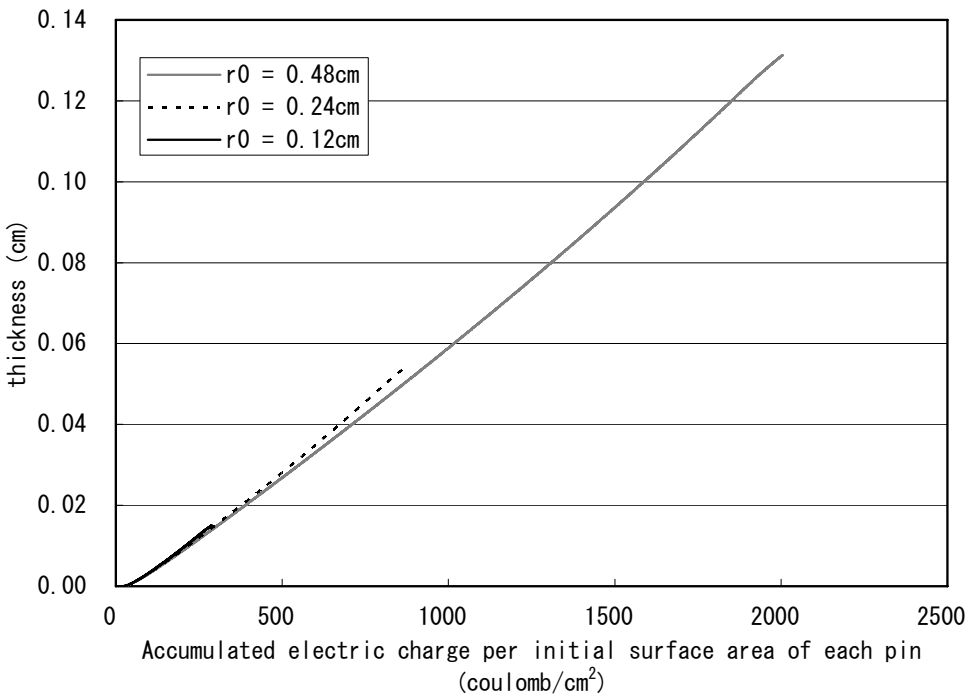

Fig. 5-10 Relation between thickness of porous zirconium layer and initial diameter of alloy

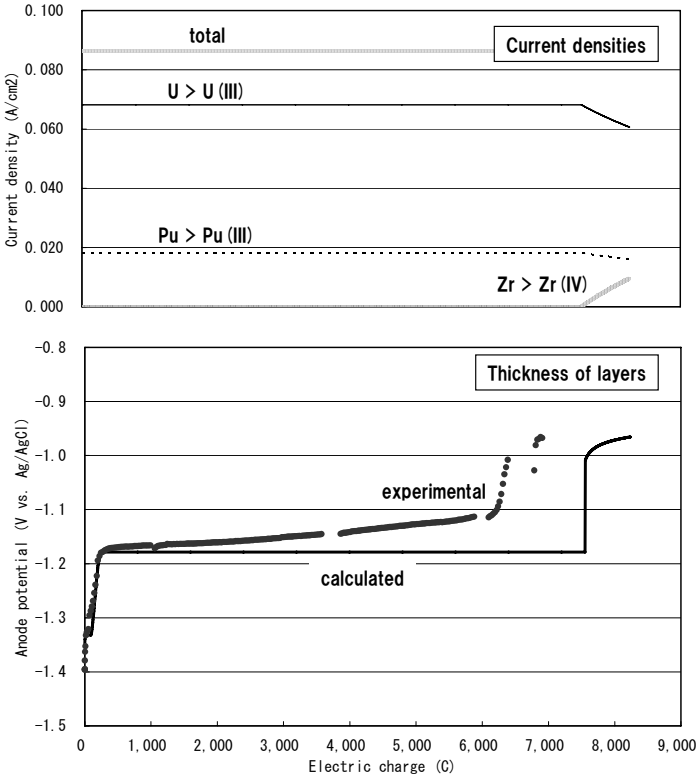

Fig. 5-11 Change in partial current densities and anode potential during electrorefining test Run-2 using U-Pu-Zr ternary alloy calculated using cylindrical type anode model

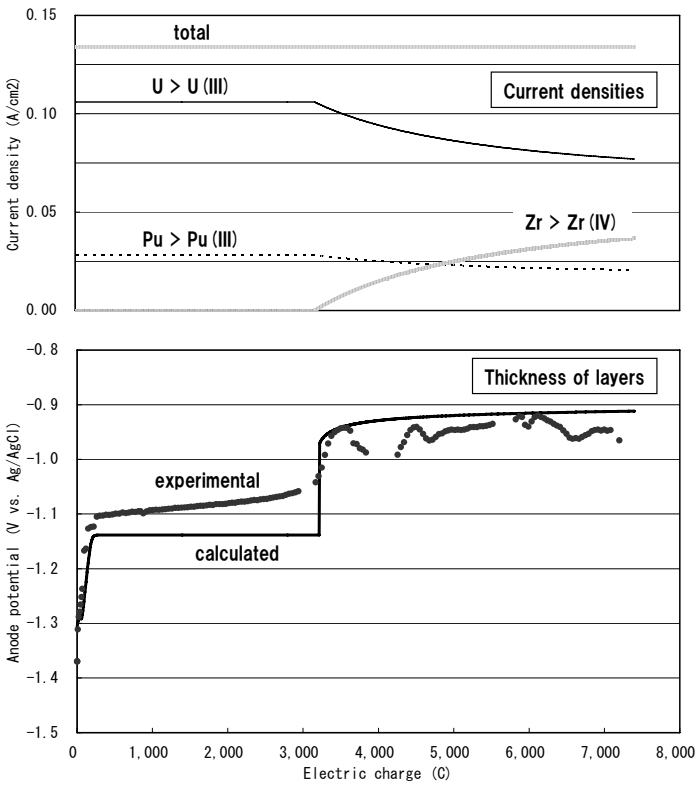

Fig. 5-12 Change in partial current densities and anode potential during electrorefining test Run-3 using U-Pu-Zr ternary alloy calculated using cylindrical type anode model

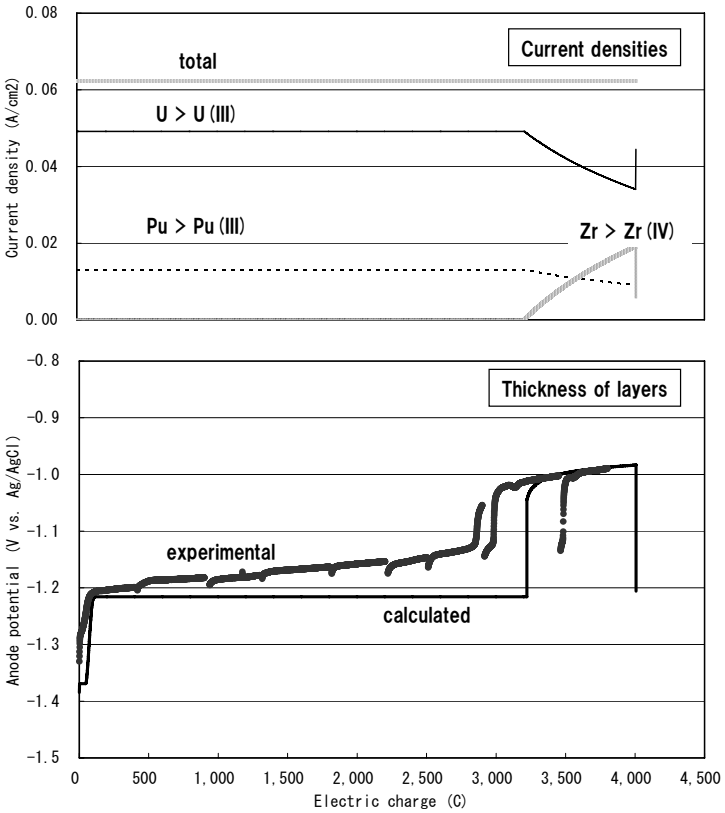

Fig. 5-13 Change in partial current densities and anode potential during electrorefining test Run-9 using U-Pu-Zr ternary alloy calculated using cylindrical type anode model

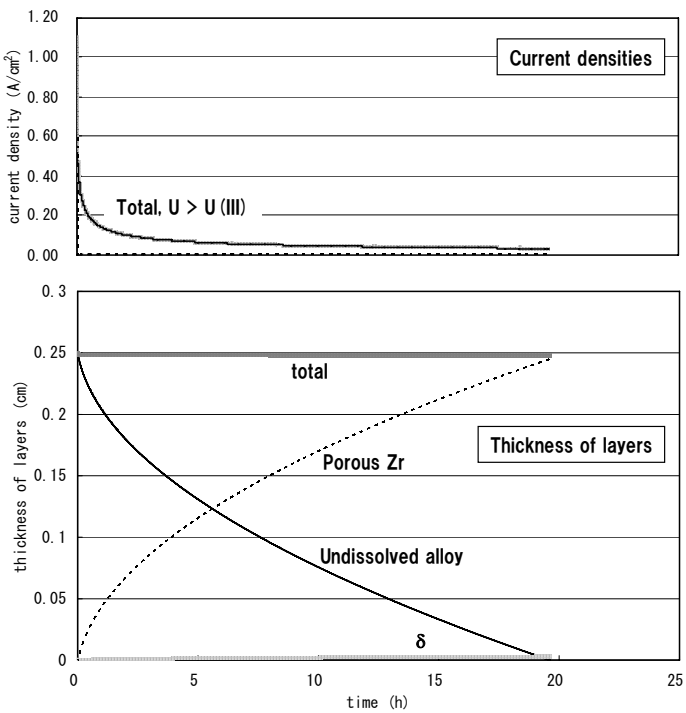

Fig. 5-14 Change in partial current densities and thickness of layers in anode residue expected at maximum current density unless dissolving zirconium calculated using planar type anode model

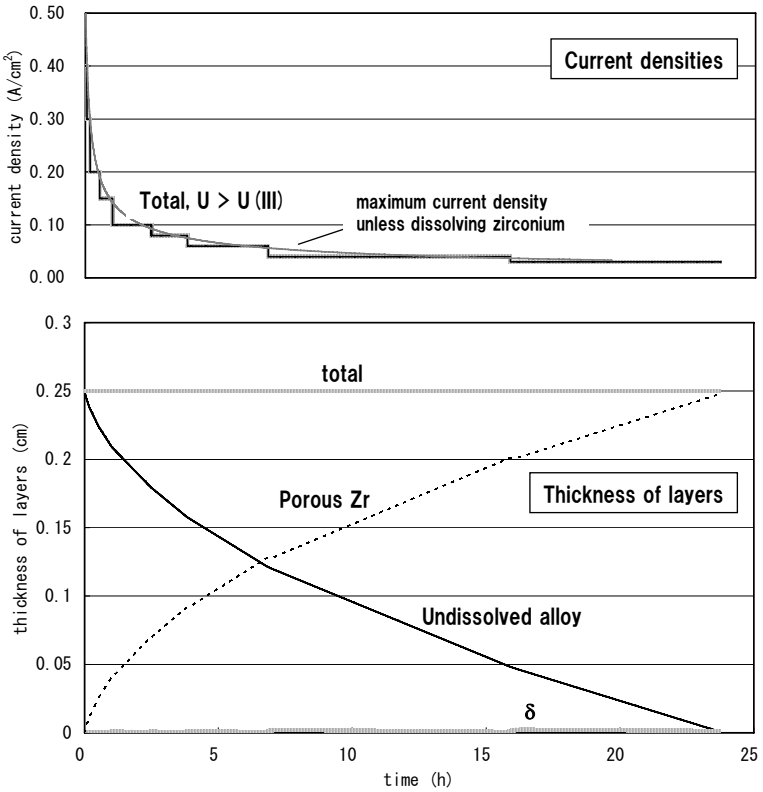

Fig. 5-15 Change in partial current densities and thickness of layers in anode residue expected at current lowered stepwise within the maximum value unless dissolving zirconium

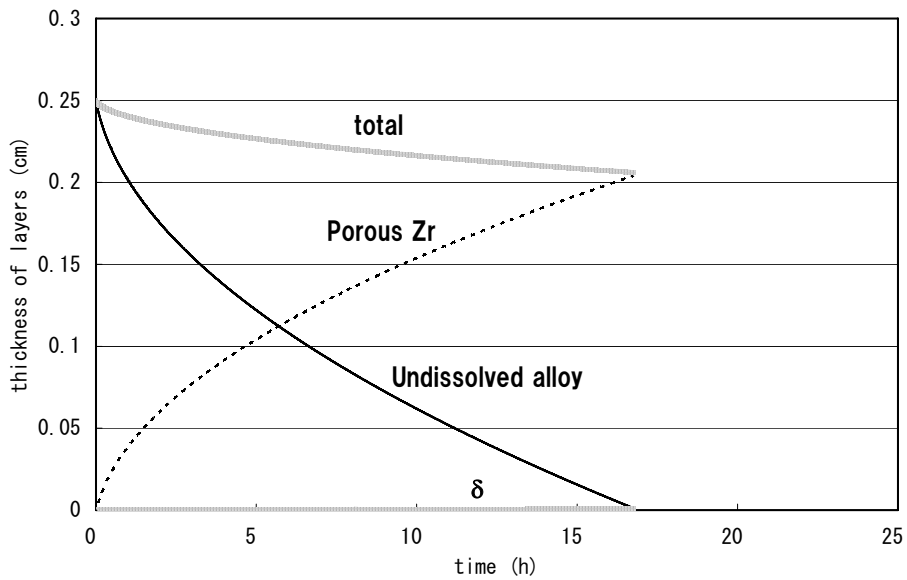

Fig. 5-16 Change in thickness of layers in anode residue expected at current maintained 5 % larger than the maximum value unless dissolving zirconium

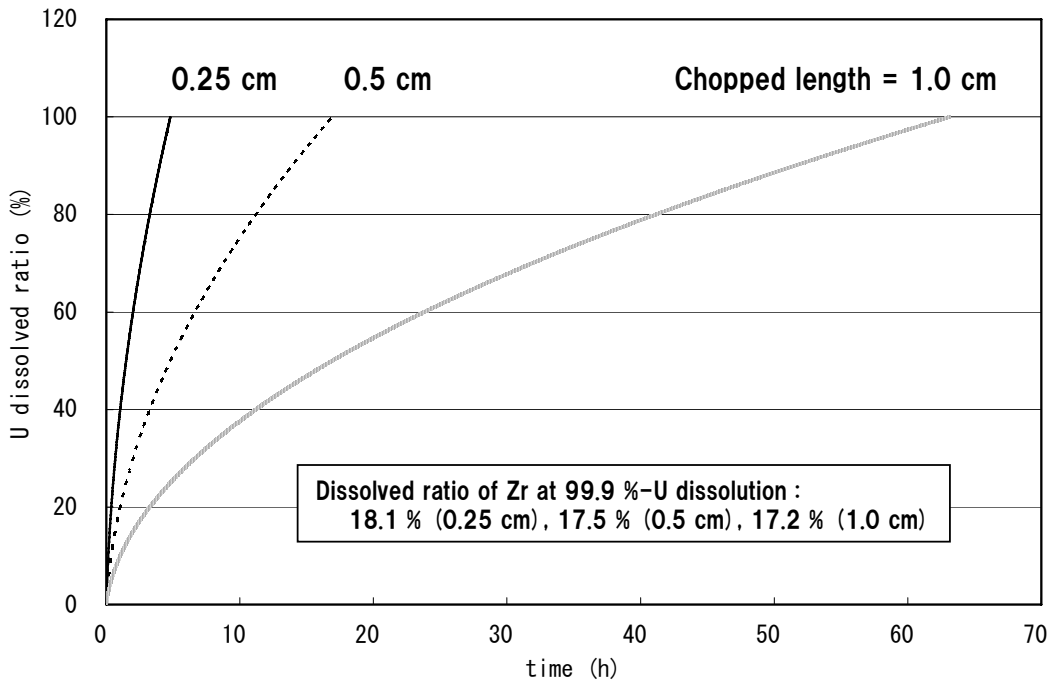

Fig. 5-17 Relationship between chopped length of alloy pins and anodic dissolution rate

Chapter 6 Application of normal pulse voltammetry to on-line monitoring of actinide concentrations in molten salt electrolyte

6.1 Background and objectives

The main step in the pyrometallurgical process is molten salt electrorefining [1], where the most part of the actinide elements are recovered and decontaminated from the fission products. Fig. 6-1 shows the schematic flow for normal operation of this electrorefining step. The spent fuel is immersed in molten chloride electrolyte and the actinide elements in the spent fuel are anodically dissolved. The chemically active fission products (FPs) such as alkali, alkaline earth, and rare earth metals exchange with the actinide chlorides in the electrolyte and accumulate in the molten salt in the form of chlorides. Uranium is selectively reduced and collected at the solid cathode due to its higher standard electrode potential than those of other actinide elements [2, 3]. Plutonium and minor actinide elements (neptunium, americium, and curium) are recovered into the liquid cadmium cathode together with uranium making use of their low activity coefficients in liquid cadmium [2-6].

The concentration of plutonium in the electrolyte increases as uranium is selectively collected to the solid cathode. In reverse, the concentration of uranium increases when plutonium is recovered into the liquid cadmium cathode. Calculation with the electrorefining simulation code [7] showed that the concentration ratio between plutonium and uranium in the electrolyte widely changes during the electrorefiner operation. Such a change of the electrolyte composition has to be monitored quickly to obtain information for switching the two types of cathodes.

After many batches of the spent fuel are processed, the molten salt electrolyte is sent to the waste treatment process to remove the accumulated FPs. Before the waste treatment process, it is planned to collect the actinides in the electrolyte by electrochemical reduction with cadmium-lithium anode [8]. In this step, the concentration of actinides is lowered by dissolution of lithium at the anode and simultaneous deposition of the actinides at the cathode. The concentration of actinides should be measured frequently in this step in order to monitor the progress of the electroreduction.

As described above, an on-line monitoring method for prompt determination of the actinide concentrations in the molten salt electrolyte is required for practically quick and smooth process control. Electroanalytical methods are considered suitable for this purpose because they are rapid in-situ measurement techniques which produce no sample waste and save cost of analytical load. Furthermore, sufficient basic data

useful for qualitative analysis, such as standard electrode potentials, are available for most of the elements in the system. In Argonne National Laboratory, the square wave voltammetry (SWV) was examined as a process monitoring method for the pyrometallurgical treatment [9]. In that study, SWV was carried out in molten chlorides containing zirconium, uranium, plutonium, and dysprosium. However, little discussion was made about the appropriate potential waveform and concentration dependence, especially the relation between the output current and the actual concentration at the practically high concentration region.

In this report, the applicability of two electroanalytical techniques was studied as the on-line monitoring method for the actinide concentrations in molten chloride electrolyte. One is SWV, and another is the normal pulse voltammetry (NPV). The concentration dependence and performance of these methods in a multi-component system were specifically studied. The standard electrode potentials of the elements fed from the metal-fueled fast reactor to the pyrometallurgical reprocessing are shown in Table 6-1. In the major steps in the pyrometallurgical process, the elements which have lower standard electrode potentials than that of zirconium exist in the molten salt electrolyte in the form of chlorides, and the other elements remain at the anode as metals. From the viewpoint of process control, usually concentrations of uranium and plutonium need to be separately determined because the expected amount of the other actinides, such as neptunium or americium, in the spent fuel is much smaller than those of uranium and plutonium.

6.2 Experimental

6.2.1 Apparatus

All the experiments were carried out in a high purity argon atmosphere glove box. Both oxygen and moisture levels in the atmosphere were kept lower than two ppm during the tests. Fig. 6-2 is the schematic view of the experimental apparatus. About 50 grams of lithium chloride-potassium chloride (LiCl-KCl) eutectic mixture was put in a high purity (> 99.5%) alumina crucible. It was placed in the magnesia secondary crucible and the stainless steel outer crucible. These crucibles were heated with the electric furnace and the temperature of the molten salt was kept to 773 ± 1 K by a proportional-integral-differential (PID) controller. The working electrode was made of tungsten wire of 1 mm diameter. About 10 mm of the lower end of the wire was immersed in the molten salt. The surface area of the working electrode could not be estimated from the immersed length because of an expected large error due to the wetting of the electrode surface by the molten salt. The tantalum wire of 1 mm

diameter was coiled and used as the counter electrode. A silver-silver chloride (1 wt% AgCl in LiCl-KCl) electrode contained in a thin Pyrex glass tube was used as reference electrode. The potential of the reference electrode was very stable at 773 K throughout the measurements.

6.2.2 Chemicals

LiCl-KCl and rare earth chlorides ($GdCl_3$ and $CeCl_3$) were purchased from Anderson Physical Laboratory. Because the purity of these chlorides was no less than 99.99 % and their moisture content was negligibly low, they were used without additional purification procedure. The concentration of uranium and plutonium in the molten salt was adjusted by the addition of LiCl-KCl-23 wt% UCl_3 and LiCl-KCl-20 wt% $PuCl_3$ which were prepared prior to these measurements [10]. The LiCl-KCl-UCl_3 mixture was prepared by the reaction of uranium metal with cadmium chloride in LiCl-KCl. The LiCl-KCl-$PuCl_3$ was prepared by the following three steps : (a) carbothermic reduction of PuO_2 to produce PuN [11], (b) formation of $PuPt_3$ by the reaction of PuN with platinum metal, and (c) exchange reaction between $PuPt_3$ and cadmium chloride in LiCl-KCl/liquid cadmium system. Metals for the electrode material (tungsten, tantalum and silver) were also of high purity (> 99.95%). They were polished and cleaned with dilute nitric acid before use.

6.2.3 Analytical procedures

EG&G Princeton Applied Research potentio/galvanostat Model 273A and EG&G 270/250 Research Electrochemistry Software were used for the electroanalytical measurement. The concentration of the actinide elements in the molten salt was determined by inductively coupled plasma-atomic emission spectroscopy (ICP-AES) of the samples.

6.3 Results and discussion

6.3.1 Result from SWV measurements

(1) Potential waveform for the SWV measurement

Before the experiments with actinide elements, the effect of the half height and the frequency of the square wave on the SWV result were examined with cerium [12]. The peak current for cerium reduction increased approximately in proportion to the half height of the square wave except for the largest case at 100 mV (Fig. 6-3). The peak was also broadened to the positive direction with the increase of the square wave half height. Sharp peaks are preferable from the viewpoint of peak separation in a

multi-component system and the peak height at the small square wave half height shown in Fig. 6-3 was considered large enough for detection and the succeeding data processing. Then a square wave half height of 5 to 10 mV was selected for the SWV measurement in this study. The increase of the square wave frequency also brought growth in the current peak width to the negative direction as seen in Fig. 6-4. At low frequency, the sharp current peaks are observed which can be more easily separated from each other although the required time for measurement becomes longer. In this study, 5 to 10 Hz was adopted for the measurement with uranium and plutonium. The entire square wave parameters are tabulated in Fig. 6-5. When the potential is scanned from –1.0 V to –2.2 V with a frequency of 5 Hz and a potential increment of 4 mV, the turnaround time required for one measurement becomes 60 s.

(2) Applicability of SWV for on-line monitoring of actinide elements

Fig. 6-6 shows the result of SWV for LiCl-KCl-$PuCl_3$ in a relatively higher concentration range (0.14 to 3.35 wt %-Pu). Distinct and sharp current peaks by reduction of plutonium were observed at around –1.7 V in all cases. However, the height of the peak current did not show a linear relation to the actual concentration of plutonium over this concentration range as shown in Fig. 6-7. Below the deposition potential, the surface area of the working electrode is expected to be a little larger when reverse step current is measured than when forward step current is measured due to the deposition of plutonium metal. Because SWV output is obtained by subtracting the reverse current from forward current in each step, the final output value would be smaller than expected especially at higher concentration. This is considered to be the reason for the non-linearity of the peak current to the plutonium concentration.

At concentration range of plutonium lower than 0.1 wt %, the linearity of the peak current to the concentration was better as shown in Fig. 6-8. In this figure, extrapolation of the linear trend to zero current crosses the x-axis at about 0.02 wt %. This concentration is considered to be an inevitable detection limit of NPV method on the conditions of this study. This limit is, however, much smaller than expected concentration range to be monitored for the process control. Experimental results in LiCl-KCl-UCl_3-$PuCl_3$ showed that the peaks for reduction of uranium and plutonium were clearly separated because there was very little overlap between the output current waves of those elements.

From the above results, it was considered to be difficult to apply SWV to the process where the concentration of actinides in the molten salt electrolyte is higher than a few wt % such as the electrorefining step in normal operation [8]. However,

SWV has many advantages when it is applied at very low concentrations of less than 0.1 wt % because of its high sensitivity and easy separation among the current peaks. It is still a candidate as an on-line monitoring method in the electroreduction step and the waste treatment process, where the concentrations of actinides are decreased to a very low level.

6.3.2 Result from NPV measurement

(1) Potential waveform for the NPV measurement

NPV with various tm and tp was also carried out in LiCl-KCl-$CeCl_3$ [12] before the actinide elements were used in order to find out the potential waveform adequate for this method, where tp is the pulse width and tm is the period between the two succeeding pulses. Fig. 6-9 shows a few examples. In this case, tp was fixed to 100 ms and tm was varied. With longer tm, the limiting current for cerium reduction was clearly defined. On the other hand, the cerium reduction current was found to decrease to some extent after the current was once reached the maximum value when tm was shorter than about ten times t_p. It indicates that tm of about ten times t_p, at least, is needed for restoration of the concentration profile around the working electrode to the initial state. At a constant tm, higher sensitivity can be theoretically expected with shorter tp. In the preliminary tests with cerium, the reduction current of cerium was approximately proportional to square root of t_p in the range of 50 to 200 ms [12]. In the potential step experiment with uranium and plutonium, however, a significant delay was found in the reduction current rise until about 90 ms after the start of measurement (Fig. 6-10). In this figure, theoretical value was calculated on assumption that the reduction of uranium and plutonium are both reversible and diffusion-controlled. The configuration of the electrochemical cell and structure of the electrodes were practically same in the tests with cerium and actinides. It is unlikely that the mechanism and the kinetics of reduction significantly differ between the cases for lanthanides and actinides in this system. Then the delay in the reduction current was considered attributed to over 10 m of wiring from the electrodes through the plutonium glove box wall to the potentiostat (in contrast with the case with cerium where length of the wiring was less than 3 m), and it was thought to be inevitable in the present circumstances. With those results, the parameters for NPV measurement in this study were determined as shown in Fig. 6-5. When the potential is scanned from –1.0 V to –2.2 V with tm of 2000 ms, t_p of 100 ms and potential increment of 4 mV, the turnaround time required for one measurement becomes 600 s.

(2) Determination of uranium and plutonium

Fig. 6-11 shows the result of NPV measurement in molten LiCl-KCl at various uranium and plutonium concentrations. It was found that the reduction current rises in two steps : one is around –1.4 V by reduction of uranium and the another around –1.7 V by reduction of plutonium. The reduction current by uranium and plutonium increased with the increase of concentrations of these elements in the electrolyte.

In order to determine the concentrations of uranium and plutonium from the NPV data, the contribution of the reduction of each element to the output current should be separately determined. For this purpose, the current output of NPV was differentiated with respect to the working electrode potential as shown in Fig. 6-12. The increase of reduction current was transformed to clear peaks by this treatment. Although the accurate criteria for the determination of tails of those peaks have not been fixed at present, the width of the peaks corresponding to the reduction of uranium and plutonium was tentatively determined to be –1.32 V to –1.57 V and –1.57 V to –1.87 V, respectively, as seen in Fig. 6-12. The increase of output current by reduction of each element was defined as the area of the corresponding peak in Fig. 6-12. A plot of the reduction currents defined in this way against the actual concentration determined by ICP-AES is shown in Fig. 6-13. The excellent linearity in this plot demonstrates the applicability of NPV to on-line monitoring in the pyrometallurgical process. There is one point for plutonium that deviates from the linear relationship. This is the case where the concentration of coexisting uranium in the molten salt was the highest (2.48 wt %) in this study. Under this condition, it is expected from the results of uranium electrorefining study [1] that reduced uranium forms dendritic deposit which increases the effective surface area of the working electrode. That is considered why the reduction current for plutonium at this point was a little larger than that expected from the linearity among the other data. This problem would be avoided by optimization of the applied potential waveform, i.e. reduction of the pulse width tp, although it was not demonstrated in this study due to the long wiring as described in 3.1.

(3) Effect of coexisting fission products

Fig. 6-14 shows the change of differentiated NPV current measured in molten LiCl-KCl containing uranium, plutonium, and gadolinium. The concentration of gadolinium in the molten salt was calculated from the amount of its chloride added to the electrolyte because the error of this method had been found to be very small in our

past studies. The peaks of these elements in the differentiated NPV data were easily separated each other. The area of the peaks corresponding to the reduction current of uranium and plutonium were not influenced by the addition of gadolinium. Since the standard electrode potentials of the other FPs in the electrolyte are lower than that of gadolinium (Table 6-1), it is expected that the concentrations of uranium and plutonium can be determined by NPV without any interference by fission products even in the practical multi-component systems.

(4) Determination of minor actinide elements

In order to discuss the determination of minor actinides, NPV was carried out in molten LiCl-KCl containing uranium, plutonium, gadolinium, and neptunium. Fig. 6-15 shows the differentiated NPV results. A slight increase by the reduction of neptunium can be found between the peaks corresponding to the reduction of uranium and plutonium. However, the reduction current of neptunium could not be determined exactly due to the overlap with the plutonium peak. Because the amount of neptunium in the molten salt electrolyte is thought to be much smaller than that of plutonium in the normal operation of the electrorefiner, determination of neptunium by NPV seems to be difficult. Determination of americium concentration by NPV is expected to be more difficult because the standard electrode potential of americium is closer to that of plutonium than in the case of neptunium. It is possible, however, that NPV or SWV is applied to determine the minor actinides in cases where the concentrations of all the actinide elements are very low, such as in the electroreduction step or in the waste treatment process.

6.4 Conclusion

The applicability of two electroanalytical methods - square wave voltammetry (SWV) and normal pulse voltammetry (NPV) - to on-line monitoring of actinide concentrations in molten lithium chloride-potassium chloride eutectic mixture was investigated for use in the pyrometallurgical processes. The potential waveforms for both methods were fixed based on the results of the preliminary tests using rare earth elements. For SWV of plutonium, the concentration dependence of the peak current was not linear at relatively high concentration, although SWV showed the advantage in high sensitivity and easy separation among the peaks in multi-component systems. The reduction currents for uranium and plutonium determined from the differentiated NPV data were proportional to their concentrations up to about 1.7 wt %. The fission product elements do not seem to affect the determined concentrations of uranium and

plutonium because the reduction currents for these elements were not influenced by the addition of gadolinium which has the nearest standard electrode potential to those of the actinides among the fission product elements. It was found to be difficult to determine neptunium in the presence of plutonium due to the overlap of the output current waves. From those results, NPV was considered to be more promising for on-line monitoring in molten salt although the optimization of applied potential waveform would be necessary for use at the higher concentrations expected in the normal operation of the electrorefiner in the pyrometallurgical reprocessing.

References

[1] T. Koyama, M. Iizuka, H. Tanaka, M. Tokiwai, Y. Shoji, R. Fujita, and T. Kobayashi, “An experimental study of molten salt electrorefining of uranium using solid iron cathode and liquid cadmium cathode for development of pyrometallurgical reprocessing”, *J. Nucl. Sci. Technol.*, **34**, 384-393 (1997).

[2] J. Roy, L. Grantham, D. Grimmett, S. Fusselman, C. Krueger, T. Storvick, T. Inoue, Y. Sakamura and N. Takahashi, “Thermodynamic properties of U, Np, Pu, and Am in molten LiCl-KCl eutectic and liquid cadmium”, *J. Electrochem. Soc.*, **143**, 2487-2492 (1996).

[3] S. P. Fusselman, J. J. Roy, D. L. Grimmett, L. F. Grantham, C. L. Krueger, C. R. Nabelek, T. S. Storvick, T. Inoue, T. Hijikata, K. Kinoshita, Y. Sakamura, K. Uozumi, T. Kawai, N. Takahashi, " Thermodynamic properties for rare earths and americium in pyropartitioning process solvents", *J. Electrochem. Soc.*, **146**, 2573-2580 (1999).

[4] M. Krumpelt, I. Johnson, J. J. Heiberger, " Thermodynamics of the cadmium-neptunium system: Solute-solvent intercation in liquid alloys ", *Metallurg. Trans.*, **5**, 65-70 (1974).

[5] I. Johnson, M. G. Chasanov and R. M. Yonco, “Pu-Cd system : Thermodynamics and partial phase diagram”, *Trans. Metallurg. Soc. AIME*, **233**, 1408-1414 (1965).

[6] Koyama, T. R. Johnson, D. F. Fischer, “Distribution of Actinides between Molten Salt/Cadmium Metal Systems”, *J. Alloys and Compounds*, **189**, 37-44 (1993).

[7] T. Koyama, M. Iizuka, H. Tanaka, *Proc. ICONE-4*, New Orleans, LA, Mar. 10-14, 1996.

[8] M. Iizuka, T. Koyama, N. Kondo, R. Fujita, and H. Tanaka, “Actinides recovery from molten salt/liquid metal system by electrochemical methods”, *J.*

Nucl. Mater., **247**, 183-190 (1997).

[9] Annual Technical Report for 1994, Chemical Technology Division, Argonne National Laboratory Report ANL-95/24 (1995), p. 88.

[10] O. Shirai, T. Iwai, Y. Suzuki, Y. Sakamura and H. Tanaka, " Electrochemical behavior of actinide ions in LiCl-KCl eutectic melts", *J. Alloys. Compd.*, **271**, 685-688, (1998).

[11] Y. Arai, S. Fukushima, K. Shiozawa and M. Handa, " Fabrication of (U, Pu)N fuel pellets", *J. Nucl. Mater.*, **168**, 280-289, (1989).

[12] M. Iizuka, “Applicability of electrochemical methods for on-line monitoring of molten salt composition - Experimental study with rare earth elements -”, Central Research Institute of Electric Power Industry Report T96054 (1997), *in Japanese*.

Table 6-1 Standard redox potentials of the elements fed to pyrometallurgical reprocessing

element	E^0 (V vs. Cl_2/Cl^-)
Te	-0.316
Pd	-0.430
Rh	-0.447
I	-0.471
Ru	-0.518
Ag	-0.853
Mo	-0.854
Eu	-0.860
Sb	-0.886
Ni	-1.011
Co	-1.207
Sn	-1.298
Fe	-1.388
Se	-1.463
Nb	-1.472
Cd	-1.532
Cr	-1.641
V	-1.749
Sm	-2.035
Mn	-2.065
Zr	-2.186
U	-2.500
Np	-2.697
Mg	-2.796
Pu	-2.803
Am	-2.865
Gd	-3.027
Nd	-3.078
Pr	-3.078
Ce	-3.094
Y	-3.106
La	-3.141
Na	-3.356

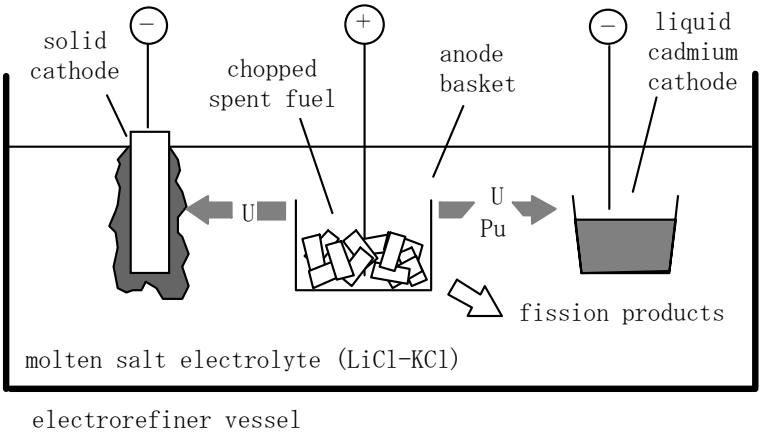

Fig. 6-1 Schematic flow of normal operation of the electrorefining step

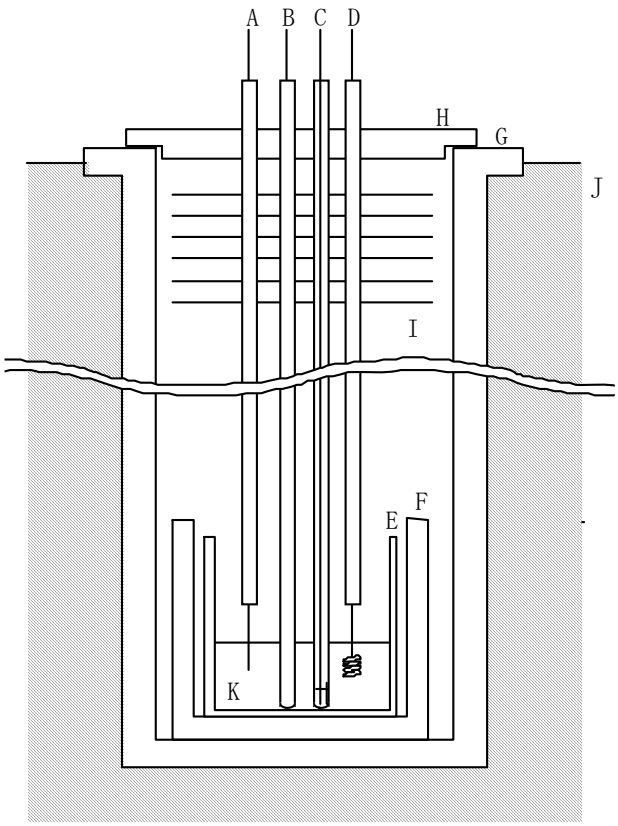

A : tungsten wire working electrode
B : thermocouple
C : Ag/AgCl reference electrode
D : tantalum wire coil counter electrode
E : alumina crucible
F : magnesia secondary crucible
G : stainless steel outer vessel
H : flange
I : heat shield
J : electric furnace
K : molten LiCl-KCl eutectic mixture

Fig. 6-2 Schematic view of the experimental apparatus

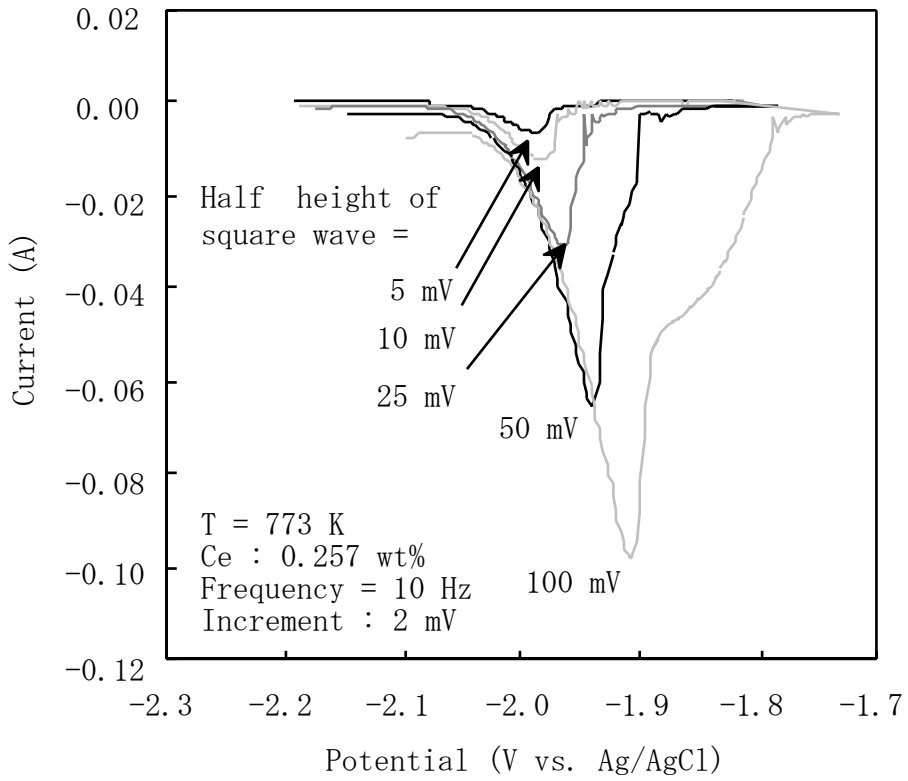

Fig. 6-3 Effect of half height of square waveform on results of SWV in LiCl-KCl-$CeCl_3$

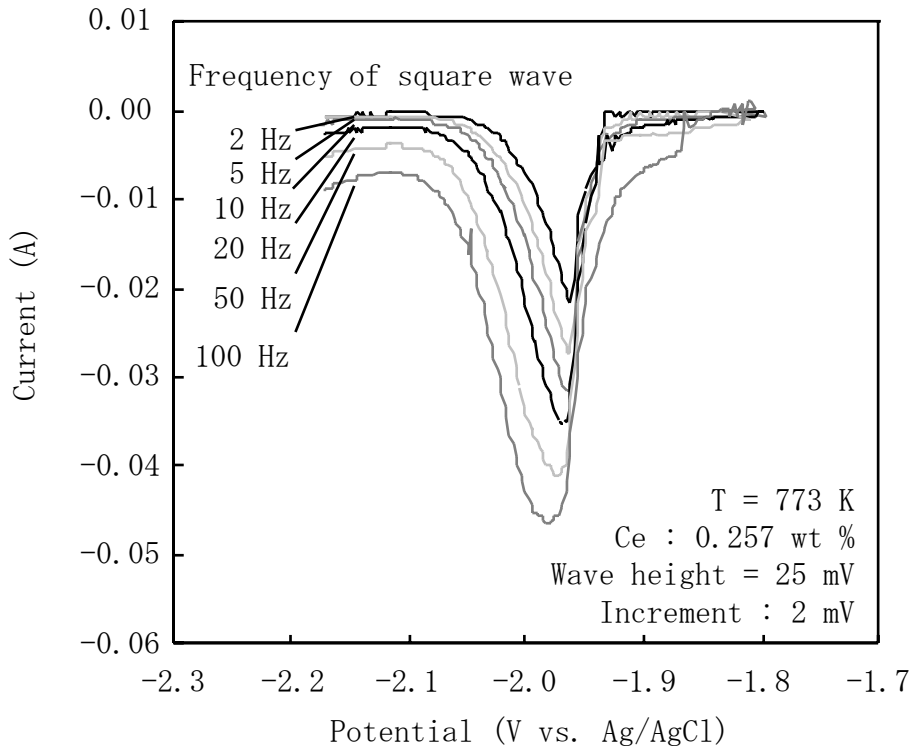

Fig. 6-4 Effect of frequency of square waveform on results of SWV in LiCl-KCl-$CeCl_3$

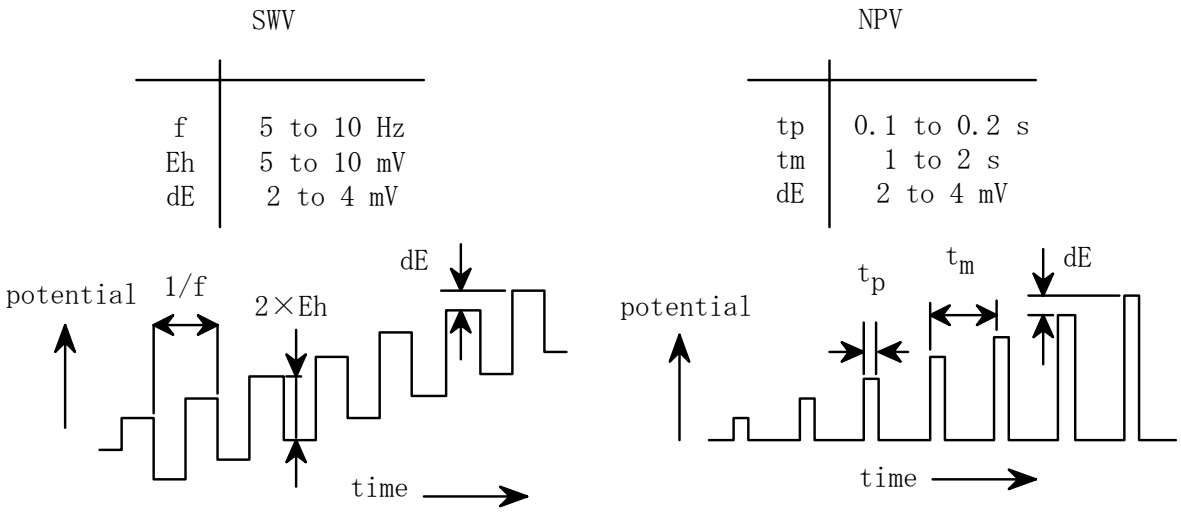

Fig. 6-5 Potential waveform parameters for SWV and NPV used in this study

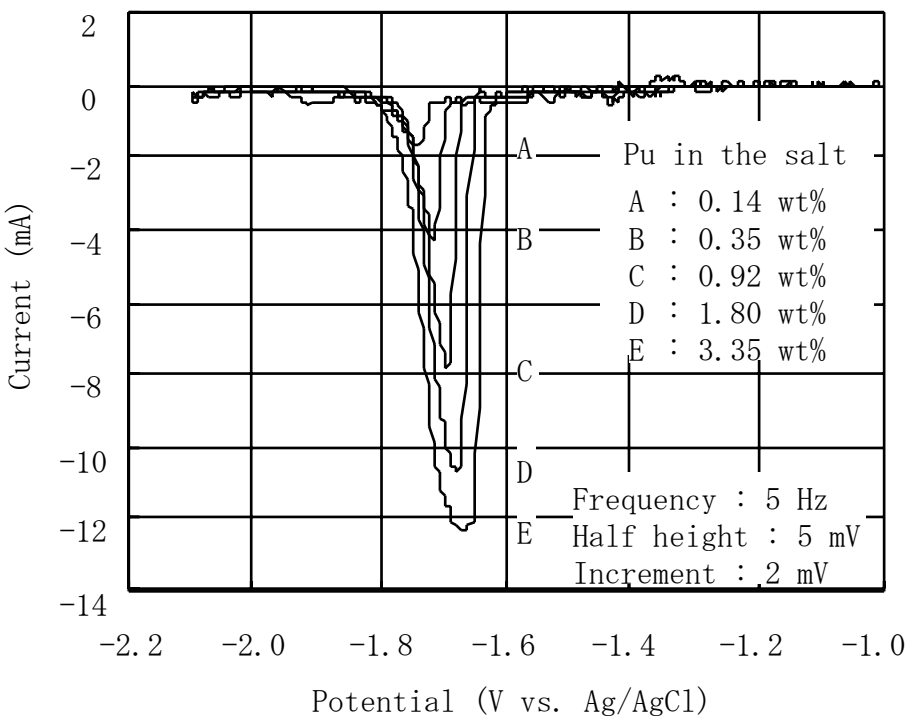

Fig. 6-6 SWV curves for LiCl-KCl-$PuCl_3$

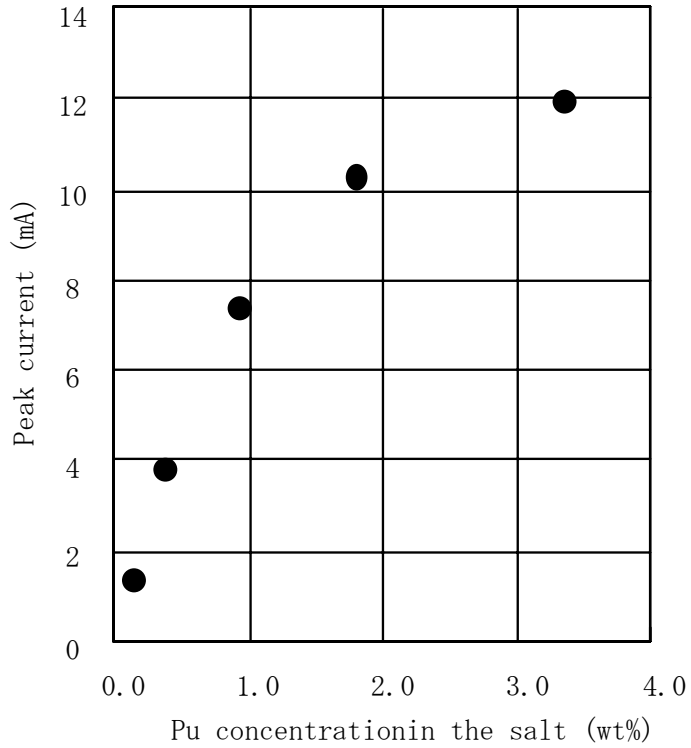

Fig. 6-7 Concentration dependence of peak height in SWV curves for LiCl-KCl-$PuCl_3$

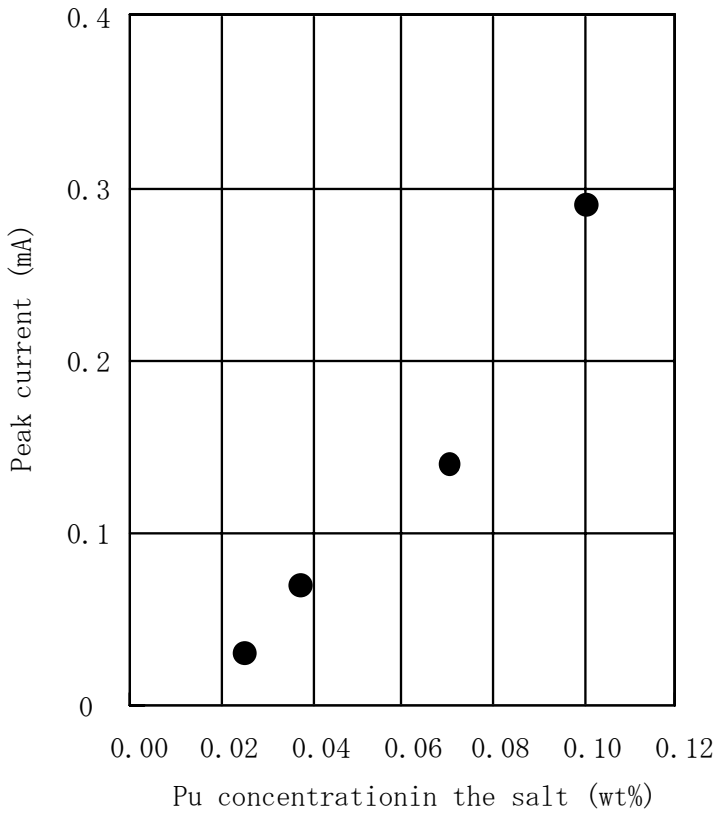

Fig. 6-8 Concentration dependence of peak height in SWV curves for LiCl-KCl-$PuCl_3$ (at lower Pu concentration)

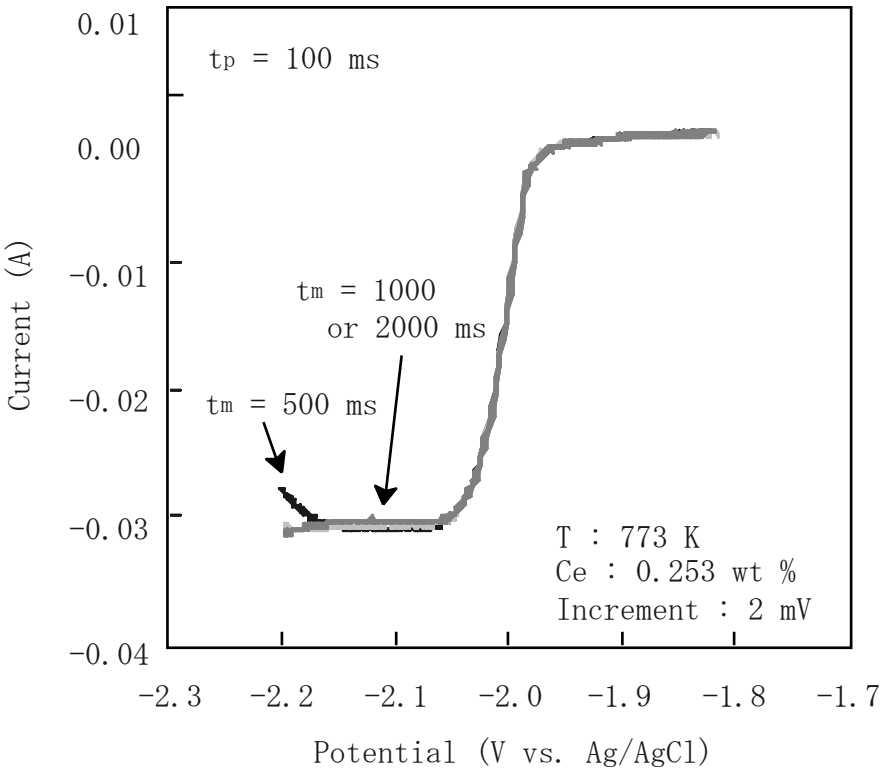

Fig. 6-9 Effect of t_m on results of NPV in LiCl-KCl-$CeCl_3$

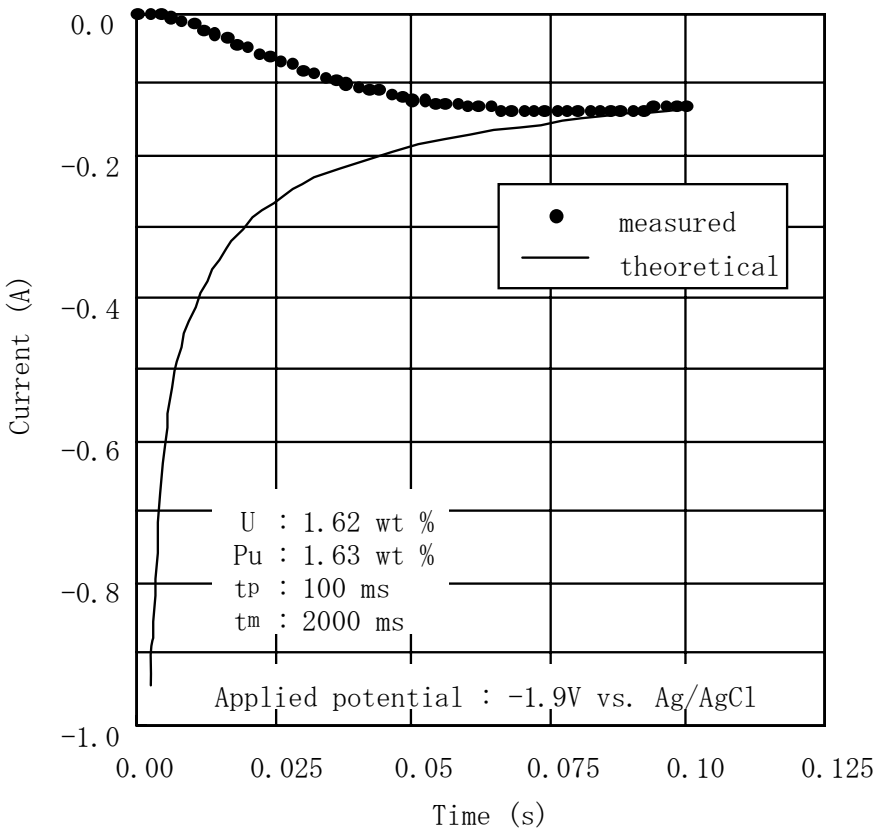

Fig. 6-10 Result of potential step experiment in LiCl-KCl-UCl_3-$PuCl_3$ compared with theoretical solution

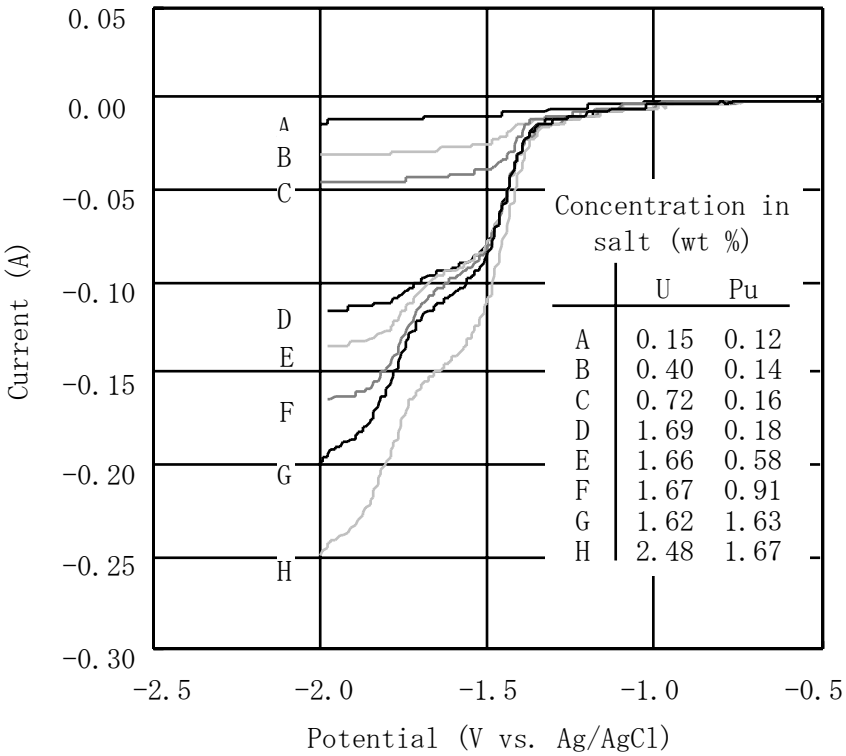

Fig. 6-11 NPV curves for LiCl-KCl-UCl_3-$PuCl_3$

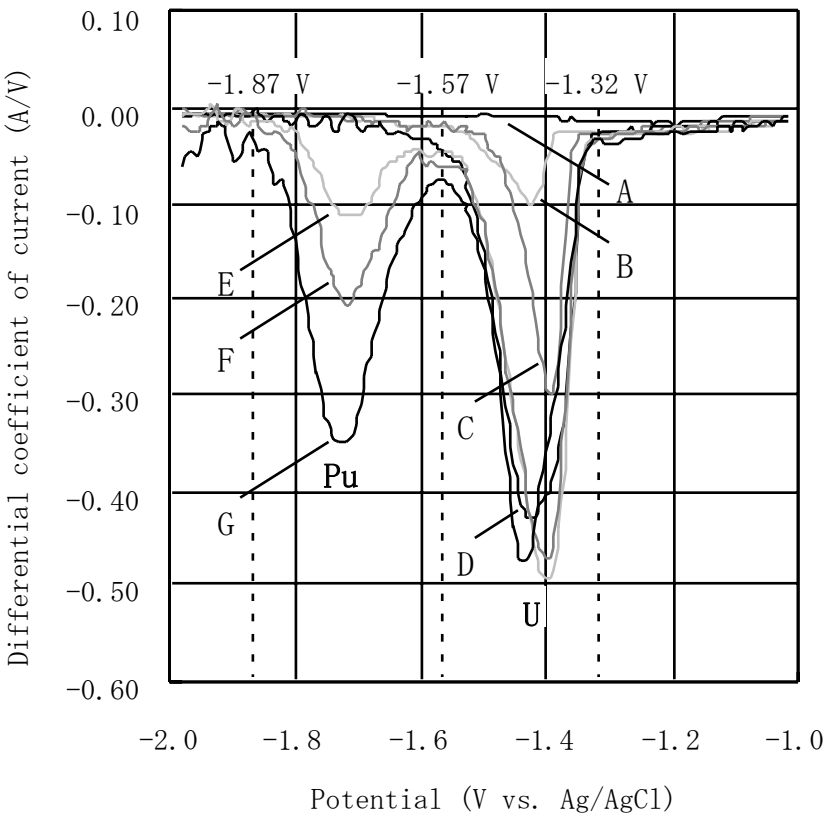

Fig. 6-12 Differentiated NPV curves for LiCl-KCl-UCl_3-$PuCl_3$

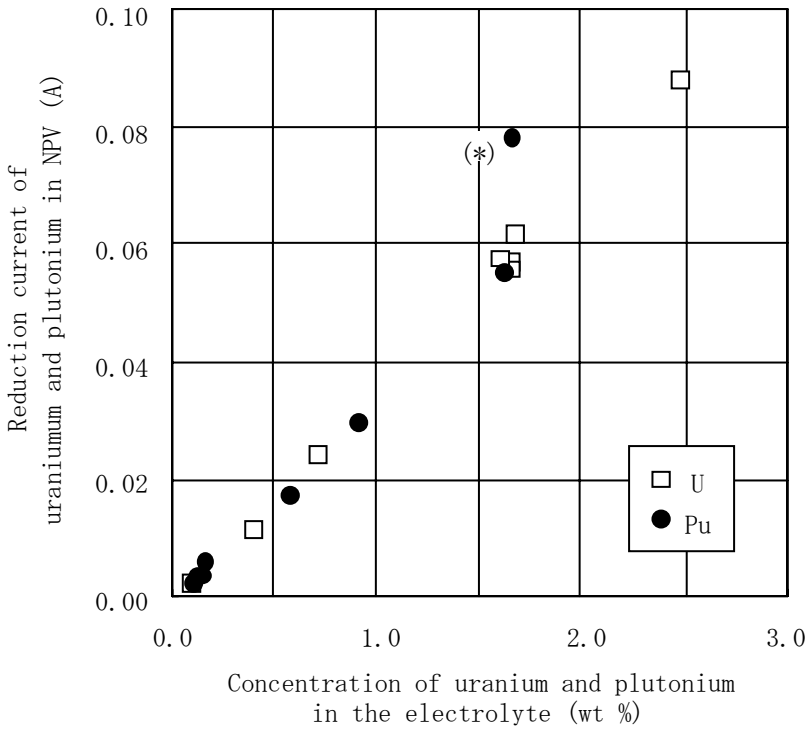

Fig. 6-13 Concentration dependence of reduction current in NPV curves for LiCl-KCl-UCl_3-$PuCl_3$

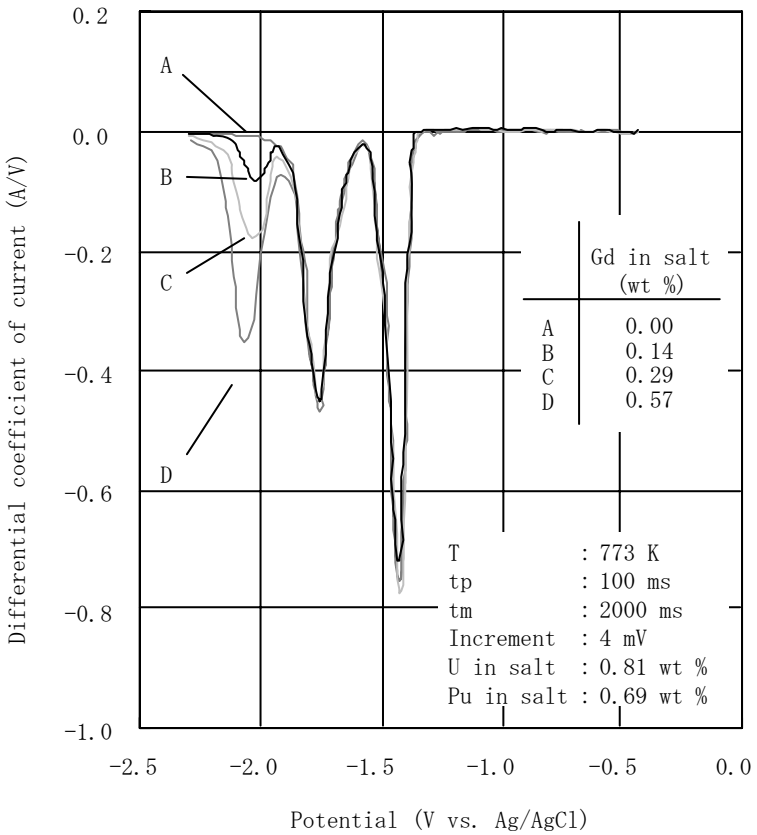

Fig. 6-14 Differentiated NPV curves for LiCl-KCl-UCl_3-$PuCl_3$-$GdCl_3$

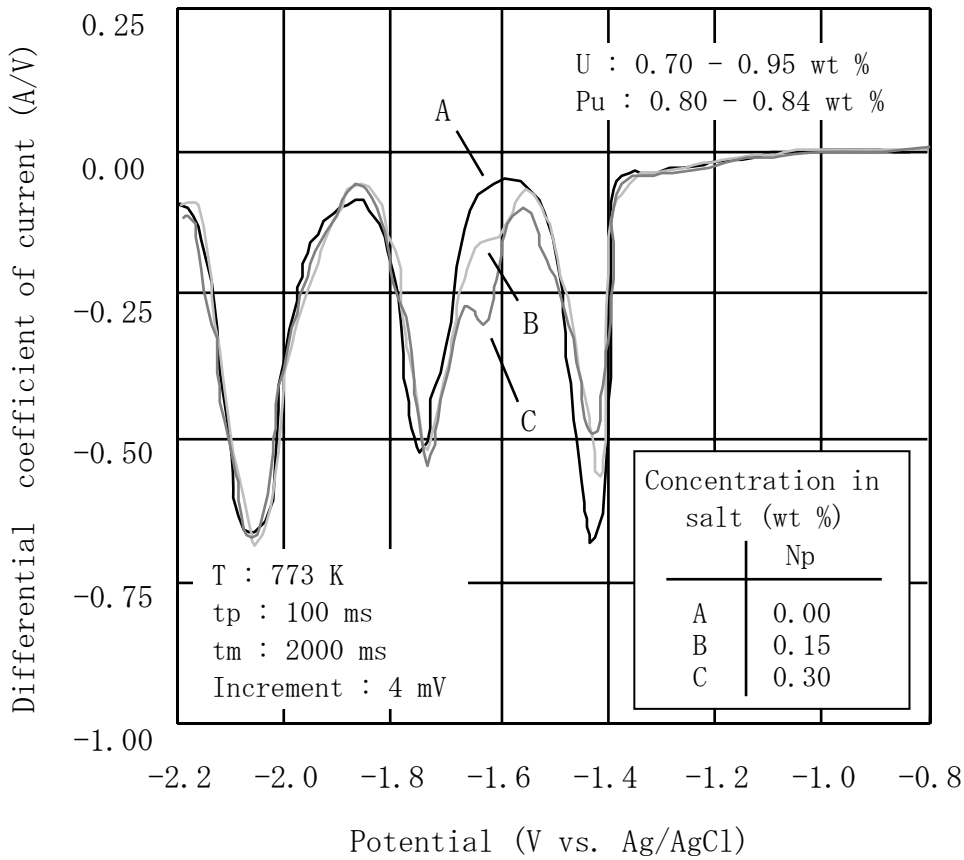

Fig. 6-15 Differentiated NPV curves for LiCl-KCl-UCl_3-$PuCl_3$-$GdCl_3$-$NpCl_3$

Chapter 7 Electrochemical reduction of $(U,Pu)O_2$ in molten LiCl and $CaCl_2$ electrolytes

7.1 Background and objectives

Development of innovative nuclear fuel cycle technology is strongly required to serve for both the environmental sustainability and the increasing energy demand. The metallic fuel cycle is proposed as one of the most promising options in the nuclear fuel cycle technologies for the next generation. The metallic fuel cycle, a combination of the metal fuel fast reactor and the pyrometallurgical reprocessing, has excellent advantages in economic, safety and proliferation resistance aspects [1].

In order to supply the metallic fuel for start-up of the fast reactors, the oxide materials, either the LWR spent fuels or the UO_2-PuO_2 mixed oxide (MOX) products from the light water reactor (LWR) fuel reprocessing, must be reduced to metals.

The lithium reduction process using lithium metal reductant in molten LiCl bath has been developed for that purpose. Reduction of UO_2 [2] and simulated spent LWR fuel [3] was demonstrated. The thermodynamic conditions for reduction of transuranium elements (TRUs) [4] were also studied. The lithium reductant was successfully recovered by electrochemical decomposition of the co-produced Li_2O in the bath [5]. Although the lithium reduction process is thus already an experimentally proven technique, there are still some technical problems to be solved such as the handling of highly reactive and sticky lithium metal and the difficulties in the design of the lithium recovery equipment.

Recently, the electrochemical reduction method has been studied for reduction of oxide nuclear fuels. This method is an application of the innovative titanium production/deoxidation processes [6-8] to the conversion of nuclear material. Figure 7-1 shows the principle of the electrochemical reduction of spent oxide fuels. The cathode and anode reactions are as follows:

Cathode: $MO_2 + 4\ e^- \rightarrow M + 2\ O^{2-}$ (7-1)

Anode: $2O^{2-} \rightarrow O_2 + 4\ e^-$ (7-2)

where M denotes actinide metals

When a carbon anode is used, CO or CO_2 is evolved in place of O_2.

Anode: $2O^{2-} + C \rightarrow CO_2 + 4e^-$ (7-3)

$O^{2-} + C \rightarrow CO + 2e^-$ (7-4)

The electrochemical reduction process eliminates the troublesome handling of lithium metal required in the lithium reduction process. Another advantage of the electrochemical reduction is that the oxide ions produced at the cathode are simultaneously consumed at the anode. It means that the concentration of oxide ions in the electrolyte can be maintained at a desired low level, while it gradually accumulates in the lithium reduction process. This nature of the process is very favorable because low oxide ion concentration thermodynamically pushes the reaction towards complete reduction of the actinide elements. Since concentration of oxide ion in the electrolyte does not increase, the amount of the electrolyte and the volume of the equipment, in consequence, can be reduced.

The fundamental behavior of UO_2 in the electrochemical reduction process has been investigated in molten LiCl [9, 10] and also $CaCl_2$ electrolytes [11]. In $CaCl_2$ bath at 1123 K, a thin but dense layer has formed in the surface region of the oxide material at the cathode due to cohesion among the reduced uranium metal particles. Since this layer hampered the outward diffusion of oxide ions evolved by the reaction (7-1), the subsequent reduction was disturbed and the central region of the cathode material remained original oxide. In LiCl bath at 923 K, on the other hand, the reduction product did not cohere so much to form a dense layer, probably because of the lower temperature. Electrochemical reduction of MOX [12] in molten LiCl was also studied. Complete reduction of a small MOX piece of around two hundred milligrams in weight was confirmed by scanning electron microscope (SEM) observation. The reduction started at the grain boundaries of the oxide material. In the course of the reduction into the grain bulk, the reduction products formed the coral-like structure.

The feasibility of the electrochemical reduction of UO_2, PuO_2 and MOX has been experimentally well explained. However, some points still need to be clarified, such as the electrochemically optimum conditions for the reduction and the cause for decrease of plutonium concentration in the reduction product [12]. In the next step, more detailed information on the behavior of plutonium in the electrochemical reduction process should be studied in order to evaluate the material balance and establish the process flow sheet.

In the present study, the electrochemical reduction of MOX was performed in molten LiCl at 923 K and $CaCl_2$ at 1123 K to evaluate the behavior of plutonium quantitatively and to define the desirable conditions for the electrochemical reduction of those materials.

7.2 Experimental

7.2.1 Apparatus

All the electrochemical reduction experiments were carried out in an argon atmosphere glove box, because both LiCl and $CaCl_2$ are highly hygroscopic and the reduction products might be easily re-oxidized even by low concentration of oxygen. The concentration of water and oxygen in the argon atmosphere was kept lower than 1.0 ppm during the tests by the argon purification system.

Figure 7-2 shows a schematic view of the experimental apparatus. A MgO crucible (40 mm in inner diameter, 75 mm in depth and 5 mm in thickness) containing LiCl or $CaCl_2$ was placed in the stainless steel vessel and heated to 923 K or 1123 K, respectively. The temperature was kept ± 2 K by a PID controller and occasionally checked with a type-K thermocouple covered with a MgO tube.

For the basic electrochemical measurement, a tantalum wire working electrode (1 mm in diameter and about 20 mm in immersed depth) was used. In the electrochemical reduction experiments, baskets of approximately 10 mm diameter made from tantalum mesh and tantalum wire were used to hold the small MOX pieces. In some cyclic voltammetry measurements, alumina cathode containers of the same dimension were used to minimize the change of the cathode surface area by the tantalum parts.

A platinum wire electrode was used as a counter electrode for the electrochemical measurement or as an anode for the electrochemical reduction experiments. The platinum wire of 1 mm diameter was formed into a coil of 4 mm in diameter and 20 mm in length. The upper end of the wire was connected to a tantalum wire to make the electrical connection. The effective length and the surface area of the platinum wire were about 200 mm and 6.3 cm^2, respectively. This platinum anode was then covered with a MgO shroud (6/10 mm in inner/outer diameters) to avoid the decrease of the current efficiency by minimizing the migration of evolving oxygen gas to the cathode.

In LiCl electrolyte, Bi-Li alloy was used as a reference electrode. About 0.5 g of Bi-35 mol % Li alloy was introduced in a MgO tube (4/6 mm in inner/outer diameters) with one end closed. According to the Bi-Li binary phase diagram, this alloy exists as a homogeneous liquid at a temperature higher than 673 K. A tantalum wire of 1 mm in diameter was inserted in the tube for the electrical connection. A small hole (0.7 mm in diameter) was made in the wall of the tube at the interface between the molten LiCl and Bi-Li alloy. This hole acts as a channel between inside and outside of

the MgO tube so that this electrode shows the potential of Li^+/Li redox equilibrium. Theoretically this potential is affected by the change of Li activity in the alloy due to the dissolution into LiCl, migration of Li metal produced at the cathode, and so on. Practically, however, this electrode showed stable potential during the experimental period because the migration of lithium through the hole was limited to very small amount. In $CaCl_2$ electrolyte, Ca-Pb alloy (37 mol % Ca) reference electrode was used. The Ca-Pb binary phase diagram shows that this alloy exists as a homogeneous liquid at a temperature of higher than 903 K. The structure of Ca-Pb reference electrode was identical to that of the Bi-Li electrode.

A potentio/galvanostat Model 263A from EG&G Princeton Applied Research and the software version 4.0 were used for both basic electrochemical measurements such as cyclic voltammetry and electrochemical reduction experiments at a constant cathode potential. In all the results in this report, cathodic current was expressed in minus direction.

7.2.2 Chemicals

LiCl and $CaCl_2$ of 99.9 % purity were purchased from Applied Physical Laboratory, U.S. It was used without any additional treatment before use since the amount of O_2 and H_2O impurities in them were extremely low. The concentration of O^{2-} in the molten salt electrolyte was adjusted by adding Li_2O of 99.9 % purity purchased from Johnson Matthey Co, or CaO of more than 99 % purity purchased from Rare Metallic Co., Japan. MgO of 99.9 % purity was used as the crucible and the electrode material. The purity of all the metals used as the electrode materials was higher than 99.9 %.

The MOX pellets of two different Pu/(U+Pu) ratios were used in this study. One had a diameter of 6 mm and Pu/(U+Pu) ratio of 9.45 wt % (MOX-a). The content of americium yielded by β^- decay from Pu^{241} in this material was 0.756 wt % of total amount of plutonium. Another MOX pellet (MOX-b) was a little larger (8 mm in diameter) and of lower plutonium content (Pu/(U+Pu) = 5.02 wt %). When these pellets were used in the electrochemical reduction tests, they were cut into slices of around 2 mm in thickness and loaded in the tantalum basket. The ceramograph of MOX-a pellet before use in the electrochemical reduction tests (Fig. 3) shows that the average grain size in this material was 5 - 10 μm.

7.2.3 Analytical methods

The molten LiCl and $CaCl_2$ samples were taken by dipping an alumina tube at

room temperature quickly into the crucible and by quenching a small amount of the salt on the surface of the tube. The salt samples were analyzed by ICP-MS for their composition. The reduction product samples were washed with methanol to remove the adhering chlorides and analyzed by SEM and energy dispersive X-ray analysis (EDX) for the microstructure and distribution of plutonium. When additional amount of sample was available, it was submitted to ICP-MS and gas-burette analysis for determination of its chemical composition and reduction ratio, respectively.

7.3 Results and Discussions

7.3.1 Determination of the desirable cathode potential range for electrochemical reduction of MOX by cyclic voltammetry

Figure 7-4 shows the cyclic voltammograms measured in the LiCl electrolyte without and with a MOX-a sample in the alumina cathode container. The difference between the cathodic current in these voltammograms, which is also shown in Fig. 7-4, corresponds to the current used in the reduction of the MOX. Although a small current for MOX reduction can be seen from about –0.45 V, the current mainly flows at lower than –0.60 V. It is well known that the reduction of lithium ($Li^+ + e^- = Li$) begins at lower than –0.70 V. Excess amount of lithium metal deposit covering the MOX surface may hamper the diffusion of oxygen ion from the cathode and disturb the progress of the reduction. In the following electrochemical reduction tests, therefore, the cathode potential was chosen in the range between –0.45 V and –0.70 V.

In the cyclic voltammograms measured in the $CaCl_2$ electrolyte with a tantalum wire working electrode (Fig. 7-5), it is observed that the cathodic current due to the reduction of calcium rises at much higher potential compared with the case in lithium chloride. This difference is caused by the existence of the reduced calcium of lower activity due to its rapid dissolution and its large solubility in the electrolyte. The dissolved calcium finally migrates to the anode and severely decreases the current efficiency in the electrochemical reduction process. Figure 7-6 shows the cyclic voltammograms measured in the calcium chloride without and with a MOX-a sample in the tantalum cathode basket. There is a clear difference in the cathodic scan of these two voltammograms at lower than –0.10 V, indicating the large current used in the reduction of the MOX. It is, however, difficult to specify the optimal cathode potential for MOX reduction, since the difference between two voltammograms makes just a straight line to the potential and does not give any particular information on desirable conditions for the reduction. Considering the influence of the reduced calcium metal, the cathode potential was chosen in the range between –0.10 V and –0.40 V in the

following electrochemical reduction tests.

7.3.2 Change of cathodic current during electrochemical reduction

Twelve electrochemical reduction tests in total, six in LiCl and six in $CaCl_2$, were carried out at various cathode potentials and oxide concentrations in the electrolyte. Major conditions and results of these tests are shown in Table 7-1 and Table 7-2, respectively. The concentrations of oxides (Li_2O in LiCl, CaO in $CaCl_2$) shown in this table are not chemically analyzed but calculated from the amount of the oxides added to the electrolytes. The expected reduced ratio in Table 7-2 can be more than 100 %, because it is calculated as the percentage of the electric charge passed during the electrochemical reduction test to the charge theoretically equivalent to the weight of the used MOX sample.

Figure 7-7 shows a typical change of the cathodic current during the electrochemical reduction tests in LiCl. The black line corresponds to Li-3 test, where –0.50 V vs. Bi-Li was applied to the MOX-a cathode. Though the reduction current increased slightly during the test, the overall trend was smooth. In Li-2 test where MOX-a was reduced at –0.65 V, on the other hand, the cathodic current showed more unstable behavior. Such variation of the cathodic current may come from interactive effects of the following three factors arising during the progress in the reduction of the MOX samples. The first is the improvement of the electric contact between the tantalum basket and the gradually reduced MOX surface. The second is disturbance in the diffusion of oxygen ions out from the cathode by the growth of the reduction product layer at the surface of the MOX. The last is exhaustion of MOX to be reduced in the cathode. According to the result shown in Fig. 7, the variation of the cathode potential does not give much difference in the cathodic current during the electrochemical reduction test. It is probably due to the fact that a large part of the cathodic current is consumed by the deoxidation of tantalum used for the cathode container and the electrical connection [11].

The change of the cathodic current during the electrochemical reduction tests in $CaCl_2$ is shown in Fig. 8. The cathodic current was larger at the cathode potential ranging from -0.25 V to -0.30 V than at -0.15 V. Because there is little difference in the cathodic current between -0.25 V and -0.30 V, the reduction current for the MOX is considered saturated within this potential range. The average cathodic current at –0.40 V of the cathode potential became much larger, certainly due to the increase of the reduction current of calcium. The frequent bursts of the cathodic current are considered to be caused by excess amount of oxygen gas generated at the surface of

the platinum anode, which decreased the effective anode surface area. Because of the high solubility of calcium metal in $CaCl_2$ at 1123 K, reduced calcium would disperse throughout in the electrolyte, severely decrease the current efficiency, and react with the insulating material in the apparatus. The cathode potential should, therefore, be kept higher than at least –0.40 V.

7.3.3 Evaluation of reduced ratio

(1) Evaluation by mass change of samples

The cathode products were washed with 20 - 30 ml of methanol, because they contained the solidified electrolytes and stuck in the tantalum baskets. Both LiCl and $CaCl_2$ were quickly dissolved in methanol and completely removed from the surface of the reduction products and the tantalum basket. Except for a few samples after the tests in LiCl, the surface of most cathode products was black probably due to oxidation by methanol. While all the cathode products from tests in LiCl electrolyte were easily removed, the products from $CaCl_2$ electrolyte were stuck strongly to the tantalum basket even after washing. The cathode products from Ca-1 and Ca-6 tests were successfully taken out from the basket, but the others were brittle and broken when removed leaving small portions of them in the baskets.

The weight of each reduction product after the washing and separation from the tantalum basket is shown in Table 7-2. By comparison between the weight of the reduction product and the theoretical value assuming 100 % reduction (i.e. the subtraction of the weight of oxygen from MOX sample weight), the reduction ratio of each sample can be evaluated.

The reduction ratio in the cathode products from the tests in LiCl ranged from 11.3 % to 53.3 %. For the tests carried out in LiCl, with the exception of Li-1 test, the evaluated cathodic current efficiency was around 10 % at a cathode potential of –0.50 V, and within a range of 35-50 % at –0.65 V, respectively. These low values are reasonable considering that a large portion of the cathodic current is consumed in the deoxidation of tantalum especially at higher cathode potential as shown in the cyclic voltammetry results (Fig. 7-4). It is uncertain why the cathodic current efficiency in Li-1 is estimated at over 100 %. The most probable reason is underestimation the product weight due to a loss of small portions in the sample handling.

In the electrochemical reduction tests carried out in $CaCl_2$, except for Ca-1 and Ca-6 tests, the reduction ratio evaluated from the mass change was evaluated more than 100 %. That is obviously due to the fact that those products were broken and small portions of them could not be recovered when they were removed from the

tantalum basket, as described above. In Ca-1 and Ca-6 tests, where unbroken cathode products were recovered, the evaluated cathodic current efficiency was about 40 % regardless of the cathode potential. This value is slightly lower than that in LiCl electrolyte, certainly due to the current losses through the reduction of calcium.

(2) Evaluation by gas-burette method

For two cathode products from the electrochemical reduction tests in LiCl, the reduction ratio was also estimated by gas-burette method [3]. A small piece of the cathode product was reacted with hydrochloric acid in a closed system, where hydrogen gas is generated by the following reactions.

$$U + 4HCl \rightarrow UCl_4 + 2H_2 \quad (7\text{-}5)$$

$$Pu + 3HCl \rightarrow PuCl_3 + 3/2H_2 \quad (7\text{-}6)$$

By measuring the volume of the evolved hydrogen gas, the amount of actinide elements in metallic state contained in the cathode product can be determined. In this study, the reduction ratio of uranium and plutonium are assumed to be equal. Finally, comparison between this value and the amount of the MOX loaded into the cathode gives the reduction ratio. The estimated reduction ratio by this method for the products of Li-2 and Li-7 tests are 46.2 % and 49.5 %, respectively (Table 7-2). These values are in good agreement with those evaluated from the mass change of the cathode, indicating that these two methods are both appropriate for reduction ratio estimation.

7.3.4 Behavior of actinide elements in electrochemical reduction

– Change of molten salt electrolyte composition

The change of the actinide concentration in the LiCl and $CaCl_2$ electrolytes during a series of electrochemical reduction tests was investigated by ICP-MS analysis. The results are plotted in Fig. 7-9. In all the tests shown in this figure, MOX-a samples are used, except for the last test in $CaCl_2$ where MOX-b sample was used. The cumulative weight of the MOX immersed in the electrolyte was taken as the abscissa for the plot.

The higher actinide concentration in the first sample taken from LiCl electrolyte is supposed to be due to contamination of the sample. It can be seen that the concentration of plutonium and americium significantly increases compared with that of uranium according with the progress of the tests. The amounts of plutonium and americium found in the LiCl electrolyte at the end of all the tests were evaluated to be

0.14 % and 2.6 %, respectively, in terms of the proportion to the total amount of each element in the MOX samples immersed in the electrolyte. It is also noted that their concentrations largely increased when Li_2O was added to the LiCl electrolyte. Since the MOX was not suspended in the electrolyte when Li_2O was added, the following behavior of plutonium and americium in the MOX under the electrochemical reduction is presumed.

- Since Li_2O concentration in the vicinity of the cathode is increased during the electrochemical reduction, soluble mixed oxide Li_2MO_3 (M : plutonium or americium) is formed and dissolves into the electrolyte.
- In the bulk LiCl electrolyte, where the Li_2O concentration is lower than that around the cathode, the mixed oxide dissociates to form MO_2 precipitate.
- When Li_2O is added to adjust its concentration in the LiCl electrolyte, a part of the precipitate forms the mixed oxide and dissolves into the electrolyte again.

The concentration of the actinides gradually increased also in $CaCl_2$ electrolyte. The large value in the uranium concentration and the high background in the plutonium concentration must be due to contamination of the samples. The proportion of the amount of plutonium or americium found in the $CaCl_2$ electrolyte to the total amount in the MOX samples is much larger than that of uranium. Because all the samples from $CaCl_2$ electrolyte were taken when each electrochemical reduction test was finished, the burst of the actinide concentration was not found as it was with LiCl electrolyte. After compensation for the background for plutonium concentration, the ratio between the amount of actinide found in the $CaCl_2$ electrolyte at the end of all the tests and that in the MOX samples before use was 0.37 % for plutonium and 5.2 % for americium, which are a little higher than those evaluated with LiCl electrolyte.

7.3.5 Behavior of actinide elements in electrochemical reduction

– Chemical composition of reduction products

The compositions of some electrochemical reduction products analyzed by ICP-MS are shown in Table 7-3. While the Pu/(U+Pu) ratio in the products of Li-1 and Li-6 tests were not essentially decreased during the tests, this ratio in the products of Ca-2, Ca-3 and Ca-5 tests were decreased by approximately 19 % in average. More noticeable difference in the electrochemical reduction behavior between with LiCl and with $CaCl_2$ electrolytes is the variation of Am/Pu ratio. Although the Am/Pu ratios in the products from LiCl electrolyte are not so much different from that in the MOX-a

sample, those ratios in the products from $CaCl_2$ electrolyte drastically decreased by about 81 % in average.

The amounts of the plutonium and americium decreased from the cathodes immersed into $CaCl_2$ are evaluated to be approximately 1.96×10^{-2} g and 1.08×10^{-3} g, respectively. It is much larger than those found in the $CaCl_2$ electrolyte which can be calculated to be about 5.58×10^{-4} g and 5.73×10^{-5} g, respectively, from the change of the concentrations shown in Figure 7-9. Such large differences show that most part of the plutonium and americium lost from the cathode were not accounted for. In the lithium reduction of the MOX pellet in LiCl, it is reported that plutonium and americium eluded the pellet and precipitated at the bottom of the crucible, and that the proportion of americium lost from the pellet to the initial loading was much higher compared with plutonium [13]. In the present study, it is likely that plutonium and americium once dissolved into $CaCl_2$ electrolyte and precipitated again during the electrochemical reduction in the same manner as observed in the lithium reduction.

Since many parameters such as the total duration of MOX immersion and the oxide concentration in the electrolytes were changed together with the electrochemical conditions during the present reduction studies, the influence of each parameter on the dissolution behavior of the actinide elements can not be evaluated separately. Although the dissolution of plutonium and americium from the cathode is not significant in LiCl electrolyte, considerable proportion of those elements eluded the reduction products in $CaCl_2$ electrolyte. Fundamental studies focused on the clarification on the mechanism of the actinide dissolution especially into $CaCl_2$ electrolyte are needed to understand the quantitative influence of the dissolution on the process performance and to adopt a proper measure for high actinide recovery rate.

7.3.6 SEM/EDX analysis of reduction products

Small samples taken from some of the reduction products were polished and submitted to the observation by optical microscope, Scanning Electron Microscope (SEM) and the Energy Dispersive X-ray (EDX) analysis.

(1) Products of electrochemical reduction in LiCl

Figure 7-10(a) and 7-10(b) show respectively the metallographs for the total section view and the SEM image of the surface region of the reduction product of Li-5 test at a cathode potential of –0.50 V. From these observations, it is clear that the sample is not reduced at all. This result is well related to the consideration that most part of the cathodic current is used for the deoxidization of tantalum at this cathode potential.

Figure 7-11 is the total section view of the reduction product from Li-2 test at a cathode potential of –0.65 V. It is seen that reduction proceeds from the surface of the MOX and the thickness of the reduced area reaches 25-30 % of the whole sample. SEM images of the border part between the reduced and non-reduced areas in the sample are shown in Fig. 7-12(a). They indicate that reduction starts from the grain boundary of the MOX and that the reduced area forms coral-like structure exactly in the same manner as described in the previous report [12]. However, the complete network of the reduced grain boundary may not be necessary for further progress of reduction, since there are isolated reduced sites even at the center of the MOX as shown in Fig. 7-12(b). When the reduced area along the surface and the internal reduced sites are added together, the above visual observation is quite consistent with the total reduction ratio of 43-46 %, which was evaluated by the mass change of the samples and by gas-burette method. Figure 7-13 shows SEM and back scattering electron (BSE) images of the central region of the same sample, where reduced and non-reduced parts coexist and the coral-like structure just begun to be formed. Pu/(U+Pu) ratio was compared between the reduced areas (point-A in the SEM image, brighter part in the BSE image) and the non-reduced areas (point-B in the SEM image, darker part in the BSE image) by EDX point analysis. The result is shown in Table 4. There is no difference between the plutonium content in the reduced and non-reduced areas. In the previous report, it has been mentioned that some part of plutonium in the reduction product obtained in LiCl electrolyte is excluded from the coral-like structure and makes Pu-rich spots outside this structure [12]. In the present study, however, neither decrease nor inhomogeneity of plutonium content in the reduction product was observed. The difference between the content of plutonium in the reduction product and in the initial MOX may be due to the insufficient accuracy in the quantitative data by EDX, but it is not essential to reduction behavior.

(2) Products of electrochemical reduction in $CaCl_2$

Figure 7-14(a) shows the metallograph for total section view of the reduction product from Ca-1 test where the MOX-a sample was reduced at –0.15 V. It indicates that reduction began from the surface and reached up to 15 – 20 % of the thickness. Metallograph for the close-up near the surface of the sample is shown in Fig. 7-14(b). In the completely reduced area (upper part in Fig. 7-14(b), the connection among the metal grains progressed and formed the structure of larger dimensions than in the inner area. It should be noted that the reduced and non-reduced areas are in close contact and that no dissociation is found between these areas. This result indicates that the

electrochemical reduction would be completed without any disturbance if the operation was continued. EDX point analysis was made at two points shown in the SEM image (Fig. 7-15) to determine the Pu/(U+Pu) ratio in the reduction product. The result is shown in Table 7-5. In the completely reduced region near the surface of the product (point-A in Fig. 7-15), the Pu/(U+Pu) ratio was a little lower than that in the inner region (point-B in Fig. 7-15) where this ratio is almost the same as that in the initial MOX. Although this difference could be attributed to the error in the EDX analysis, it is also likely that dissolution of the transuranium elements into the $CaCl_2$-CaO electrolyte, as described above, affects the composition of the surface region of the reduction product. Figure 7-16 represents the metallograph for the central region of the same sample. Considerable proportion of the MOX has been reduced from the grain-boundary. Although it looks similar behavior to that previously reported for electrochemical reduction in LiCl [12], the progress of the reduction in the central region starts much earlier in this case even without enough connection among the reduced sites. At present, it is difficult to distinguish the reduction in the central region was caused by the electrochemical reduction or by the chemical reaction with calcium metal generated by reduction of the electrolyte.

The total section views of the reduction product from Ca-4 (cathode potential of -0.25 V) and Ca-1 tests observed by the optical microscope are shown in Fig. 7-17. The metallic shine of the Ca-4 product obviously tells that whole product was completely reduced. Metallograph for the total section view is shown in Fig. 7-18. Since the reduced material cohered to the surface of the product, its density at the surface region has become quite high, while the considerable portion of hollow space was made inside. The bent shape of the product was certainly formed by its shrinkage due to the cohesion of the reduced material. Fragility of the reduction products recovered from $CaCl_2$ electrolyte, observed after the separation from the tantalum baskets, might be due to the large vacant space inside them as shown in Fig. 7-18.

Figure 7-19(a) shows the total section view of the reduction product from Ca-6 test, at a cathode potential of –0.35 V, observed by the optical microscope. Figure 7-19(b) shows the metallograph of the close-up view near the surface of the same product. It is distinctive that the surface region is selectively reduced and that the boundary between the reduced/non-reduced areas is more discontinuous than those in the other products. In the metallograph of the central region (Fig. 7-20), reduction of the MOX has begun, but the reduction ratio appears much lower than that in Ca-1 product (Fig. 7-16). This is considered to be caused by formation of surface barrier of the coherent reduced material that impedes the further progress of the reduction into

inner region of the MOX. The total section view by SEM (Fig. 7-21(a)) shows that the density of the reduction product is higher at the surface and central regions, than the intermediate region. A closer view of the near surface region (Fig. 7-21(b)) shows that the reduced material in the intermediated part has become detached as parallel lamellar structures. Decrease of the electrical conductivity due to the void in the lamellar structure, as well as the formation of the surface barrier, would explain the interruption of the reduction. The cause for such variation in the morphology of the reduction product should not be the difference in the cathode potential itself, but the excessive deposition of calcium metal on the cathode which brings very high reduction rate and consequently leads to the fast and localized outward shrinkage of the reduced material in the surface region of the product.

Table 7-6 shows the results of EDX point analysis of the reduction product from Ca-6. The analysis of the reduced part was made in the dense surface region. It is found that the averaged Pu/(U+Pu) ratio in the reduced part is about 14 % lower than that in the not-reduced region. This behavior shows a clear contrast with that observed in LiCl, where no change in the plutonium content in the cathode was found during the electrochemical reduction (Table 7-4). On the other hand, this EDX result is in accordance with the above-mentioned decrease of plutonium in the reduction products and the increase of plutonium concentration in the $CaCl_2$ electrolyte during the electrochemical reduction tests investigated by ICP-MS.

7.3.7 Favorable condition for electrochemical reduction of MOX

Based on the above experimental results, advantage of selection between LiCl and $CaCl_2$ as the electrolyte for the electrochemical reduction of the MOX is discussed in this section.

(1) Reduction potential, reduction rate and cathodic current efficiency

From the results from the CV measurement and the electrochemical reduction tests at constant cathode potential followed by SEM/EDX analysis, it was found that the MOX was reduced at -0.65 V vs. Bi-35 mol % Li reference electrode in LiCl. Under this condition, the reduced ratio evaluated both from the mass change between the reduction and by the gas-burette method was around 50 %. The cathodic current efficiency calculated from the reduced ratio was around 40 %.

In $CaCl_2$, on the other hand, the MOX was reduced in the whole range of the tested cathode potential (-0.15 V to -0.40 V), although the reduction was interrupted by formation of the surface barrier made of the reduced material at the lower cathode potential (-0.30 V). At –0.25 V, the MOX was completely reduced although the

product was brittle probably due to the internal porosity formed by shrinkage of the reduced material. In the tests where the unbroken cathode products were recovered, the cathodic current efficiency was evaluated 40 - 50 %.

From the viewpoint of the cathode potential range for the electrochemical reduction, the preferable condition is limited similarly either in LiCl or $CaCl_2$. Although the reduction rate seems a little higher in $CaCl_2$ according to the change of the reduction current during the electrochemical reduction tests, the advantage is not yet quantitatively clear. There is no obvious difference in the cathodic current efficiency between the both electrolytes.

(2) Dissolution of actinide elements into electrolyte

Dissolution of plutonium and americium into the electrolyte was found both in LiCl and in $CaCl_2$ electrolytes. The concentrations of these actinides at the end of the tests were higher in $CaCl_2$ than those found in LiCl electrolyte. The ICP-MS and EDX analyses for the reduction products also showed that the amounts of these elements lost from the cathodes were much more than those increased in $CaCl_2$, indicating the formation of the precipitates containing these actinides during the tests. From the viewpoint of process design for high recovery ratio, LiCl is obviously more favorable electrolyte.

(3) Operating temperature

Due to the high melting point of $CaCl_2$ (1045 K), the electrochemical reduction in $CaCl_2$ electrolyte should be operated at around 1123 K, which is much higher than 923 K required for LiCl. This is a disadvantageous point in terms of the material selection and the cost to design, fabricate and maintain the process equipment. Another problem arising from the high operation temperature is the formation of the surface barrier formed on the reduction product due to the progress of the connection among the reduced metal grains.

(4) Compatibility with the pyrometallurgical processes

Since the alkali and alkaline earth fission products are expected to dissolve into the electrolyte during the electrochemical reduction, the electrolyte should be consolidated as high level waste form. Development of the waste form for water-soluble chlorides is the serious problem for the pyrometallurgical processes. Although the operation temperature of the electrochemical reduction in LiCl electrolyte is higher than that in the pyrometallurgical process for the metallic fuel

(773 K), the similar waste treatment process with zeolite would be applicable. However, completely different waste treatment method should be developed for $CaCl_2$ electrolyte because of the much higher operating temperature.

Taking the above discussions from four viewpoints into consideration, LiCl is concluded to be advantageous as the electrolyte used in the electrochemical reduction of MOX at present.

7.4 Conclusions

The electrochemical reduction of UO_2-PuO_2 mixed oxides (MOX) was investigated in molten LiCl at 923 K and $CaCl_2$ at 1123 K to evaluate the behavior of the plutonium quantitatively and to define the favorable conditions for the electrochemical reduction of those materials.

In LiCl, it was found that the MOX was reduced at -0.65 V vs. Bi-35 mol % Li reference electrode by the CV measurement and the electrochemical reduction tests at constant cathode potential followed by SEM/EDX analysis. Under this condition, the reduced ratio evaluated both from the mass change between the reduction and by the gas-burette method was around 50 %. The cathodic current efficiency calculated from the reduced ratio was around 40 %.

In $CaCl_2$, on the other hand, the MOX was reduced in the whole range of the tested cathode potential (-0.15 V to -0.40 V), although the reduction was interrupted by formation of the surface barrier made of the reduced material at the lower cathode potential (-0.30 V). At –0.25 V, the MOX was completely reduced although the product was brittle probably due to the internal porosity formed by shrinkage of the reduced material. In the tests where the unbroken cathode products were recovered, the cathodic current efficiency was evaluated 40 - 50 %.

Dissolution of plutonium and americium into the electrolyte was found both in LiCl and in $CaCl_2$ electrolytes. The concentrations of these actinides at the end of the tests were higher in $CaCl_2$ than those found in LiCl electrolyte.

Taking the above experimental results and the compatibility with the pyrometallugical processes into consideration, LiCl was concluded to be more advantageous as the electrolyte used in the electrochemical reduction of MOX at present.

References

[1] T. Inoue, T. Yokoo and T. Nishimura, “Assessment of advanced technologies for the future nuclear fuel cycle,” *Proc. Int. Conf. on Future Nuclear Systems (Global’99)*, Jackson Hole, WY, Aug. 29-Spt. 3, 1999 (1999).

[2] T. Usami, M. Kurata, T. Inoue, H. E. Sims, S. A. Beetham and J. A. Jenkins, “Pyrochemical reduction of uranium dioxide and plutonium dioxide by lithium metal,” *J. Nucl. Mater.*, **300**, 15 (2002).

[3] T. Kato, T. Usami, M. Kurata, T. Inoue, H.E.Sims and J. A. Jenkins, “Development of Reduction Technology for Oxide Fuels – Lithium Reduction of a Simulated Spent Oxide Fuel – ,” CRIEPI Report T01003 (2001), *in Japanese*.

[4] T. Usami, T. Kato, M. Kurata, T. Inoue, H. E. Sims, S. A. Beetham and J. A. Jenkins, “Lithium reduction of americium dioxide to generate americium metal,” *J. Nucl., Mater.*, **304**, 50 (2002).

[5] A. Kawabe, T. Kato and M. Kurata, “Development of Reduction Technology for Oxide Fuels – Electrolysis of Li_2O in Molten LiCl – ,” CRIEPI Report T02041 (2003), *in Japanese*.

[6] T. H. Okabe, M. Nakamura, T. Oishi and K. Ono, "Electrochemical deoxidation of titanium", *Met. Trans. B*, **24**, 449-455 (1993).

[7] G. Z. Chen, D. J. Fray and T. W. Farthing, “Direct electrochemical reduction of titanium dioxide to titanium in molten calcium chloride”, *Nature*, **407**, 361-364 (2000).

[8] K. One and R. O. Suzuki, "A new concept for producing Ti sponge: Calciothermic reduction", *J. Metals*, **54**, 59-61 (2002).

[9] C. S. SEO, S. B. Park, B. H. Park, K. J. Jung, S. W. Park and S. H. Kim, “Electrochemical study on the reduction mechanism of uranium oxide in a LiCl-Li_2O molten salt”, *J. Nucl. Sci. Technol.*, **43**, 587 (2006).

[10] K. Gourishankar, L. Redey, M. Williamson and D. Graczyk, “Electrochemical reduction of oxides”, *Proc. 5th Topical Meeting on DOE Spent Nuclear Fuel and Fissile Material Management*, Charleston, SC, Sep. 17-20, 2002.

[11] Y. Sakamura, M. Kurata and T. Inoue, “Electrochemical Reduction of UO_2 in Molten $CaCl_2$ or LiCl,” *J. Electrochem. Soc.*, **153**, D31 (2006).

[12] M. Kurata, T. Inoue, J. Serp, M. Ougier and J. P. Glatz, “Electro-chemical reduction of MOX in LiCl,” *J. Nucl. Mater.*, **328**, 97 (2004).

[13] T. Usami, T. Kato, M. Kurata, T. Inoue, H. E. Sims and J. A. Jenkins, “Lithium reduction of a MOX pellet”, *J. Nucl. Sci. Tech.*, Supplement 3, 858 (2002).

Table 7-1 Major conditions of the electrochemical reduction tests

Run No.	electrolyte	oxide concentration *1 (wt %)	used MOX	amount of MOX (g)	catdhode potential *2	applied electric charge (C)	duration (h)
Li-1	LiCl	0.103	MOX-a	0.286	-0.5V vs Bi-Li	82	7.34
Li-2	LiCl	0.103	MOX-a	0.262	-0.65V vs Bi-Li	431	5.01
Li-3	LiCl	0.213	MOX-a	0.343	-0.5V vs Bi-Li	303	6.77
Li-4	LiCl	0.213	MOX-b	0.564	-0.5V vs Bi-Li	343	6.33
Li-5	LiCl	0.272	MOX-a	0.301	-0.65V vs Bi-Li	463	9.60
Li-6	LiCl	0.517	MOX-a	0.279	-0.65V vs Bi-Li	335	7.32
Ca-1	$CaCl_2$	0.196	MOX-a	0.293	-0.15V vs Ca-Pb	638	6.06
Ca-2	$CaCl_2$	0.196	MOX-a	0.296	-0.25V vs Ca-Pb	846	2.91
Ca-3	$CaCl_2$	0.196	MOX-a	0.298	-0.4V vs Ca-Pb	523	1.21
Ca-4	$CaCl_2$	0.501	MOX-a	0.351	-0.25V vs Ca-Pb	1480	8.27
Ca-5	$CaCl_2$	0.501	MOX-a	0.252	-0.3V vs Ca-Pb	1551	6.49
Ca-6	$CaCl_2$	1.013	MOX-b	0.231	-0.3V vs Ca-Pb	483	2.16

*1 calculated from the amount of oxides (Li_2O in LiCl, CaO in $CaCl_2$) added to the electrolyte

*2 Bi-35 mol % Li and Pb-37 mol % Ca reference electrodes were used in LiCl and $CaCl_2$, respectively.

Table 7-2 Major results of the electrochemical reduction tests

Run No.	amount of MOX (g)	cathode potential *1	applied electric charge (C)	weight of washed product (g)	reduced ratio evaluated from mass change (%)	reduced ratio evaluated by gas-burette (%)	expected reduced ratio (%)	cathodic current efficiency (%)
Li-1	0.286	-0.5V vs Bi-Li	82	0.277	26.8	-	20.1	134
Li-2	0.262	-0.65V vs Bi-Li	431	0.249	43.1	46.2	115	37
Li-3	0.343	-0.5V vs Bi-Li	303	0.338	11.3	-	61.8	18.3
Li-4	0.564	-0.5V vs Bi-Li	343	0.555	12.6	-	42.6	29.6
Li-5	0.301	-0.65V vs Bi-Li	463	0.282	53.3	49.5	108	49
Li-6	0.279	-0.65V vs Bi-Li	335	0.267	36.6	-	84.1	43.5
Ca-1	0.293	-0.15V vs Ca-Pb	638	0.274	55.5	-	152	36
Ca-2	0.296	-0.25V vs Ca-Pb	846	0.224	207	-	200	104
Ca-3	0.298	-0.4V vs Ca-Pb	523	0.234	181	-	123	148
Ca-4	0.351	-0.25V vs Ca-Pb	1480	0.285	158	-	295	54
Ca-5	0.252	-0.3V vs Ca-Pb	1551	0.153	332	-	431	77
Ca-6	0.231	-0.3V vs Ca-Pb	483	0.216	55.2	-	146	38

*1 Bi-35 mol % Li and Pb-37 mol % Ca reference electrodes were used in LiCl and $CaCl_2$, respectively.

Table 7-3 Composition of electrochemical reduction products analyzed by ICP-MS

Run No.	Li-1	Li-6	Ca-2	Ca-3	Ca-5
Concentration (μg/g-sample)					
U	8.42×10^5	8.99×10^5	1.04×10^6	9.29×10^5	6.62×10^5
Pu	1.03×10^5	9.25×10^4	8.37×10^4	7.58×10^4	5.69×10^4
Am	8.33×10^2	6.77×10^2	1.40×10^2	3.03×10^2	8.00×10^1
Ratio (wt%)					
Pu/(U+Pu) in reduction product	10.9	9.32	7.48	7.54	7.91
Pu/(U+Pu) in initial MOX			9.45		
Am/Pu in reduction product	0.811	0.732	0.167	0.400	0.140
Am/Pu in initial MOX			0.756		

Table 7-4 Pu/(U+Pu) ratio in Li-2 reduction product determined by EDX point analysis

		point-A reduced part	point-B not reduced part	initial MOX
U content	(wt %)	86.55	88.04	-
Pu content	(wt %)	11.85	11.3	-
Pu/(U+Pu)	(%)	12.0	11.4	9.45

Table 7-5 Pu/(U+Pu) ratio in Ca-1 reduction product determined by EDX point analysis

		point-A reduced part	point-B not reduced part	initial MOX
U content	(wt %)	90.24	89.84	-
Pu content	(wt %)	8.08	9.27	-
Pu/(U+Pu)	(%)	8.2	9.4	9.45

Table 7-6 Pu/(U+Pu) ratio in Ca-6 reduction product determined by EDX point analysis

		Reduced areas						Non-reduced areas			
		1	2	3	4	5	Average	1	2	3	Average
U content	(wt %)	94.1	92.1	95.0	93.3	90.5	-	92.3	93.0	92.7	-
Pu content	(wt %)	4.96	5.29	4.19	5.36	6.65	-	6.51	5.70	6.34	-
Pu/(U+Pu)	(%)	5.01	5.43	4.22	5.43	6.85	5.39	6.59	5.78	6.40	6.26

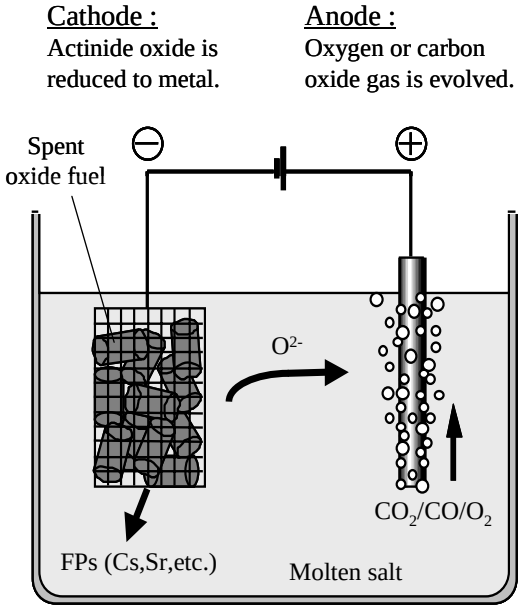

Fig. 7-1 Schematic diagram of the electrochemical reduction process

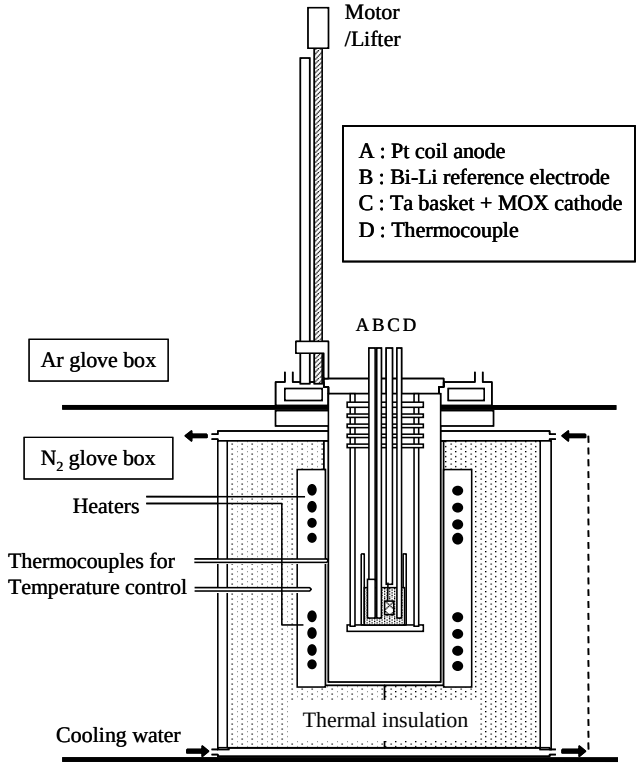

Fig. 7-2 Schematic view of the experimental apparatus

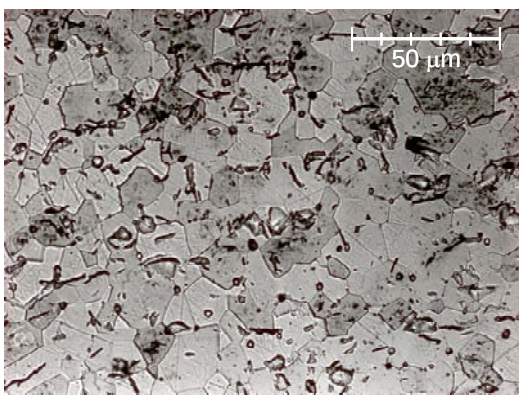

Fig. 7-3 Ceramograph of MOX-a pellet (Pu/(U+Pu) = 9.45 wt %) before electrochemical reduction

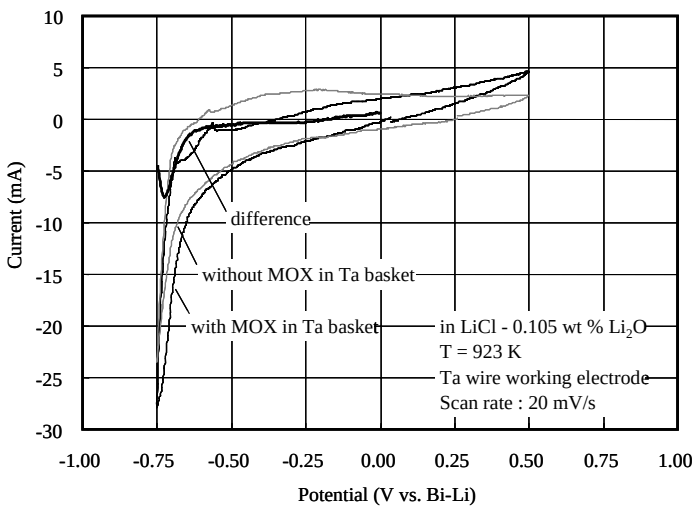

Fig. 7-4 Cyclic voltammograms measured in LiCl electrolyte with/without MOX in cathode

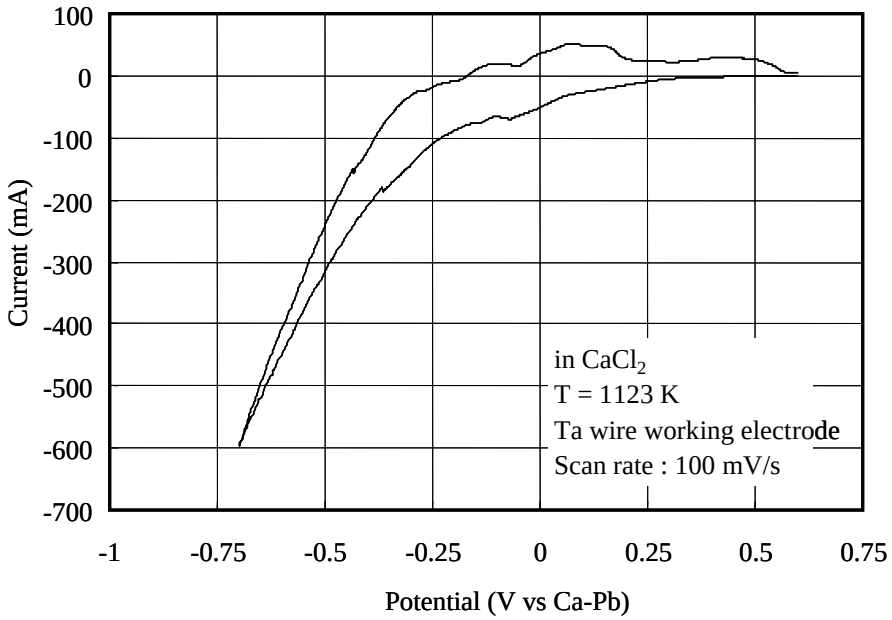

Fig. 7-5 Cyclic voltammograms measured in $CaCl_2$ electrolyte with tantalum wire electrode

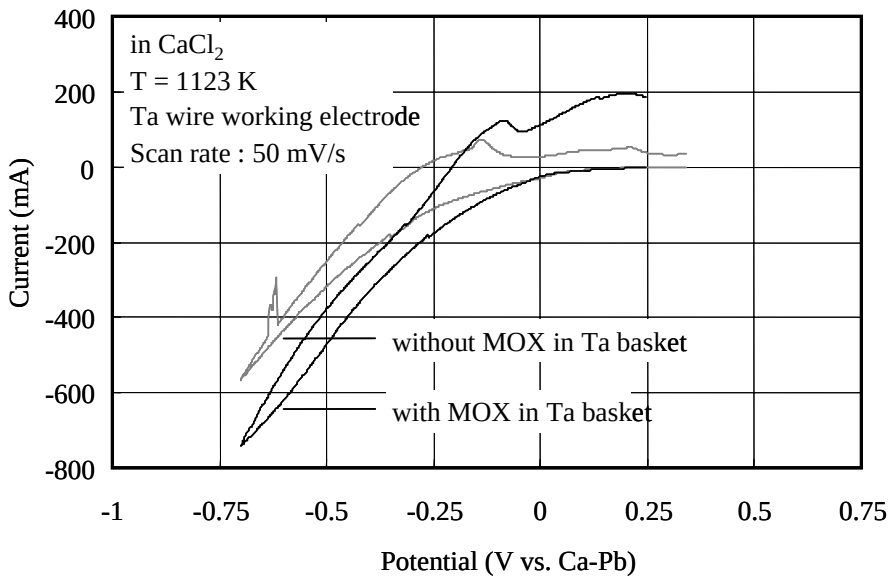

Fig. 7-6 Cyclic voltammograms measured in $CaCl_2$ electrolyte with/without MOX in cathode

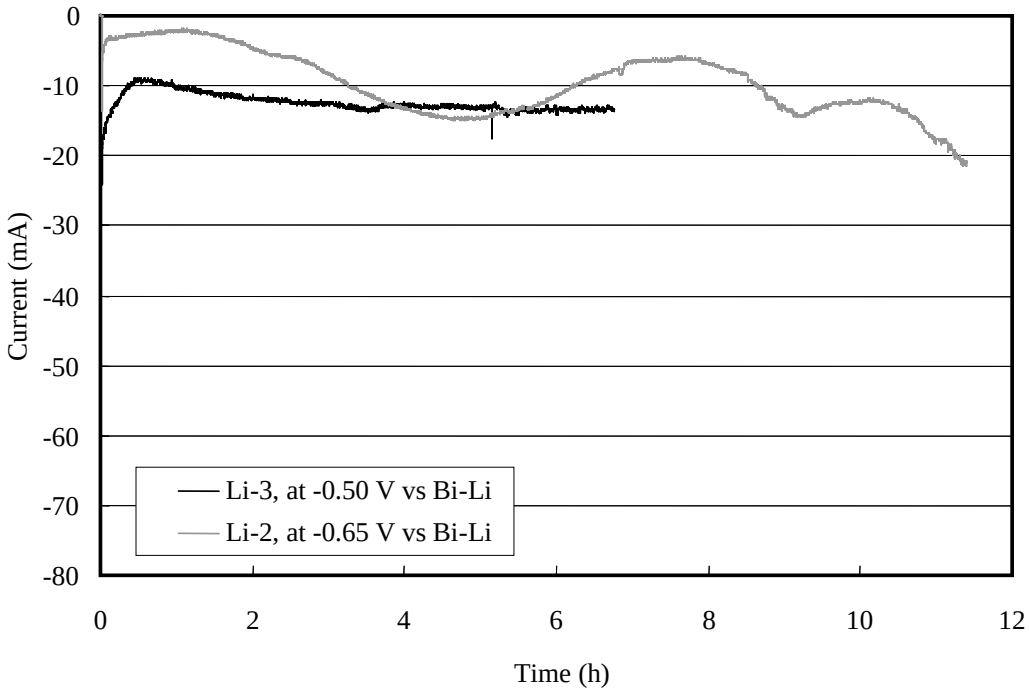

Fig. 7-7 Change of the cathodic current during the electrochemical reduction tests in LiCl

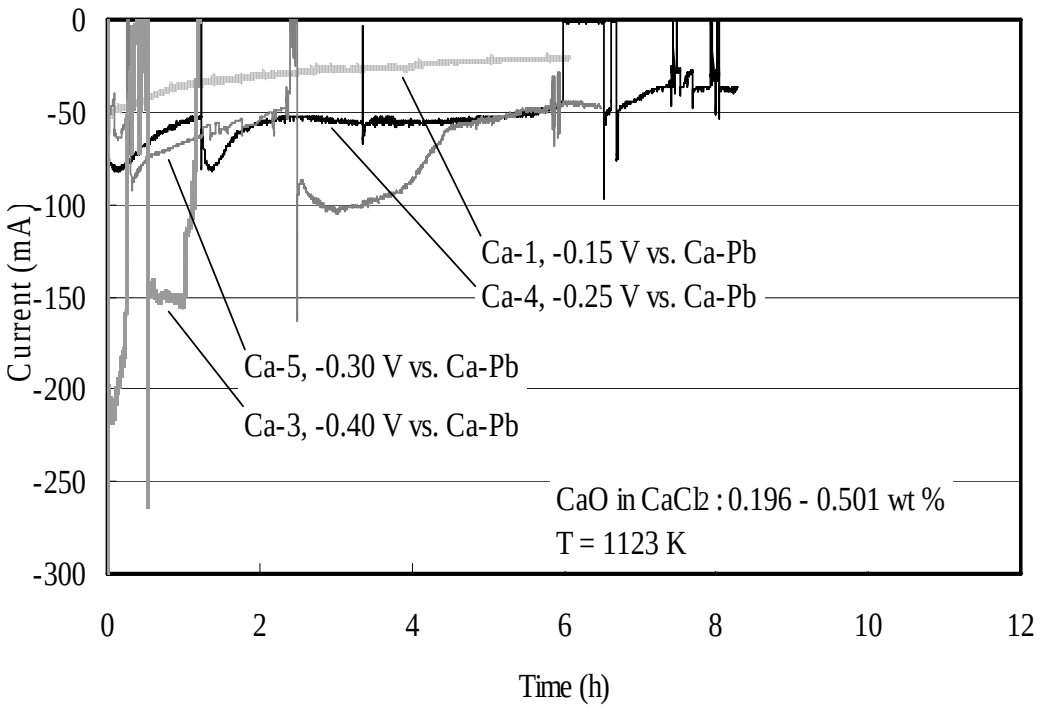

Fig. 7-8 Change of the cathodic current during the electrochemical reduction tests in $CaCl_2$

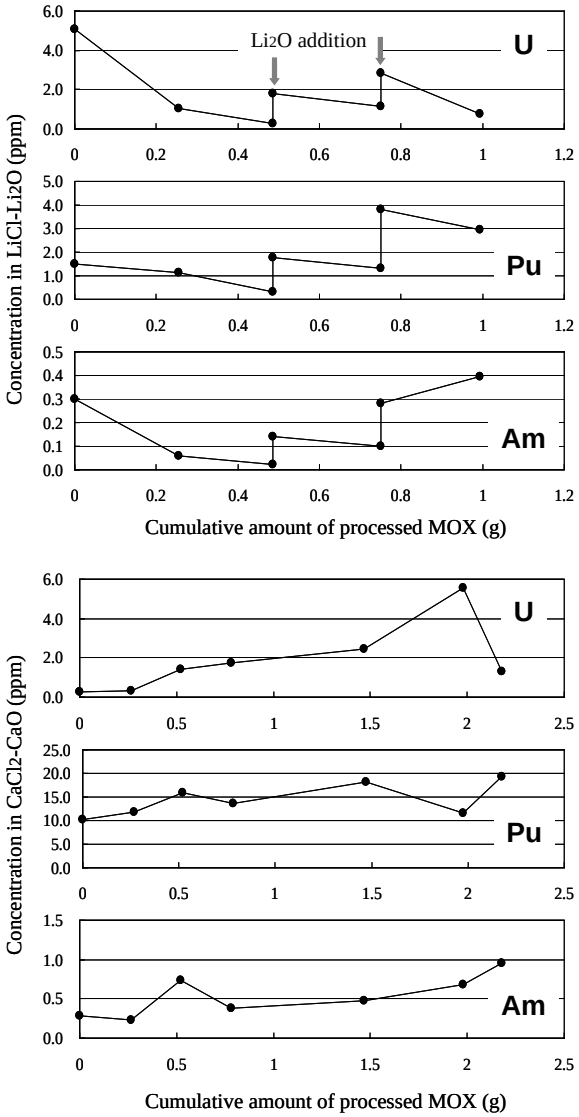

Fig. 7-9 Change of actinide concentration in LiCl and $CaCl_2$ electrolytes during electrochemical reduction tests

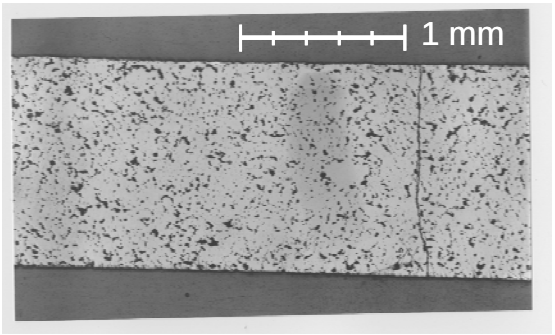

(a) Metallograph for the total section view

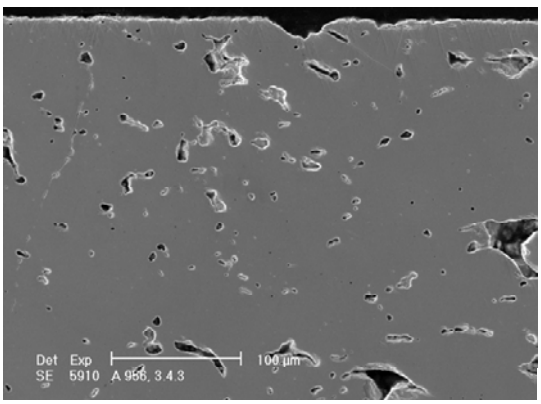

(b) SEM image of the surface region

Fig. 7-10 Section view of the reduction product from Li-5

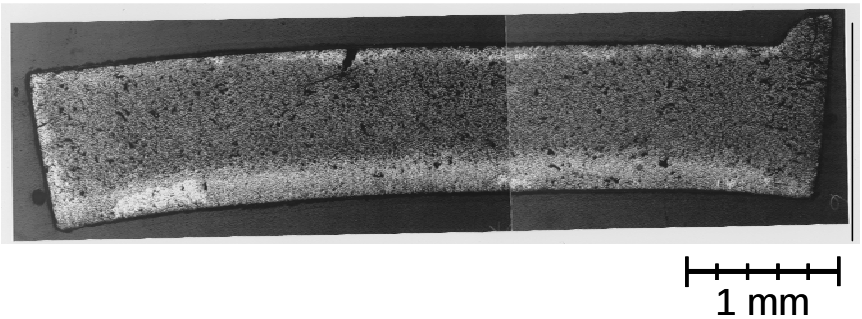

Fig. 7-11 Total section view of the reduction product from Li-2

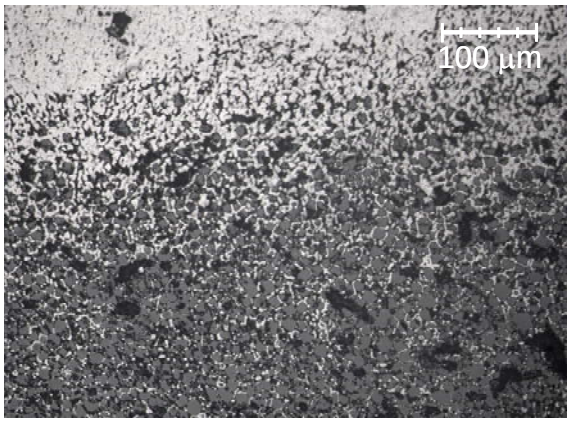

(a) The border part between reduced and not reduced areas

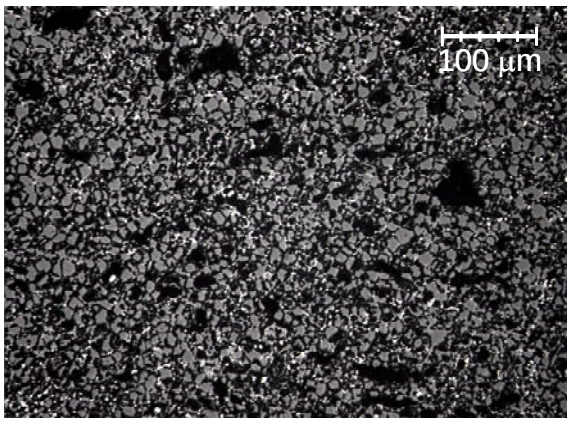

(b) Isolated reduced site at the center

Fig. 7-12 SEM images of the reduction product from Li-2

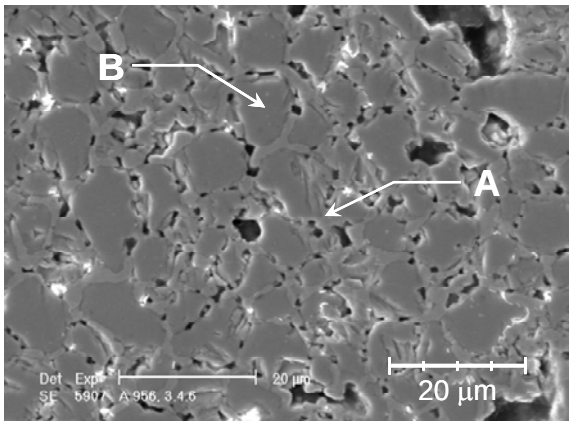

(a) SEM image

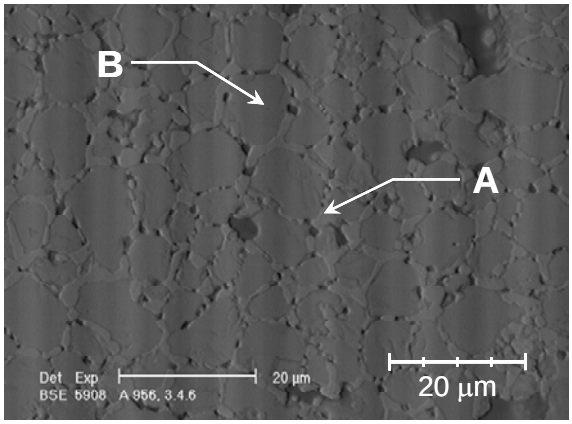

(b) BSE image

Fig. 7-13 SEM and BSE images of the central region of the reduction product from Li-2

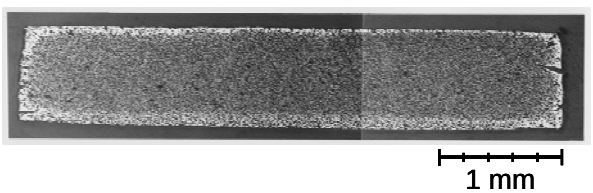

(a) Total section view

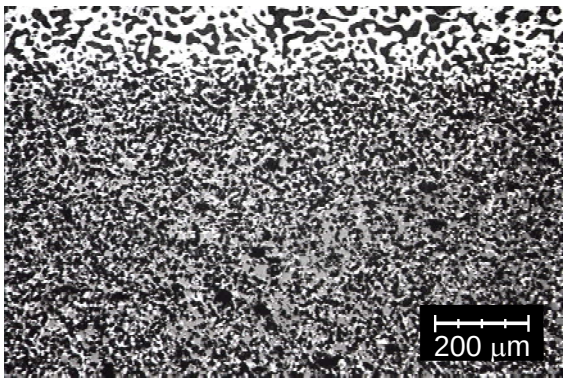

(b) Close-up view near the surface

Fig. 7-14 Metallographs for the section view of the reduction product from Ca-1

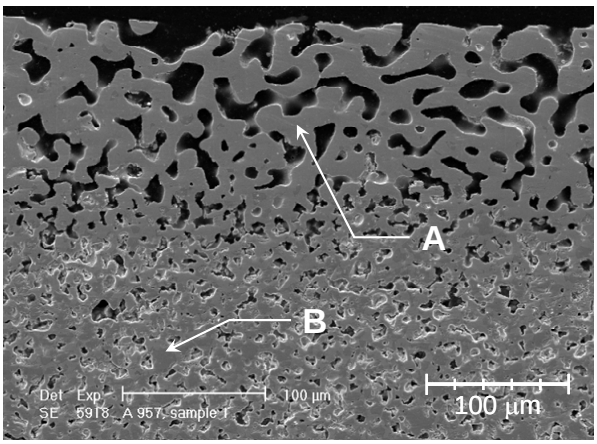

Fig. 7-15 SEM image of the reduction product from Ca-1

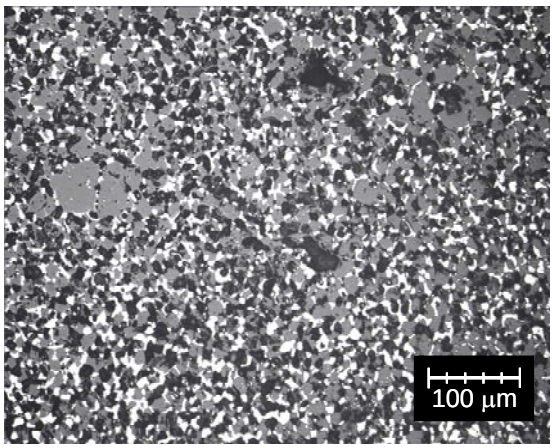

Fig. 7-16 Metallograph of the central region of the reduction product from Ca-1

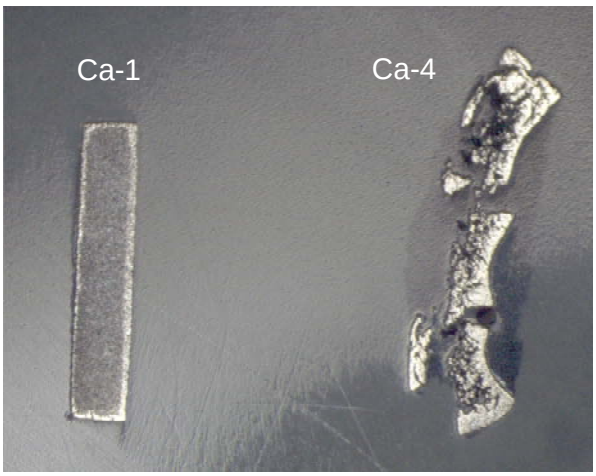

Fig. 7-17 Total section view of the reduction product from Ca-4 with optical microscope

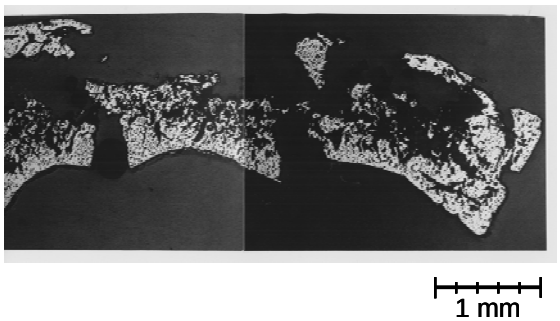

Fig. 7-18 Metallograph of the total section view of the reduction product from Ca-4

(a) Total section view with optical microscope

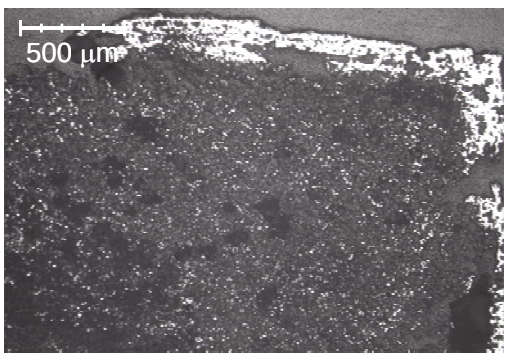

(b) Metallograph of the close-up view near the surface

Fig. 7-19 Section view of the reduction product from Ca-6

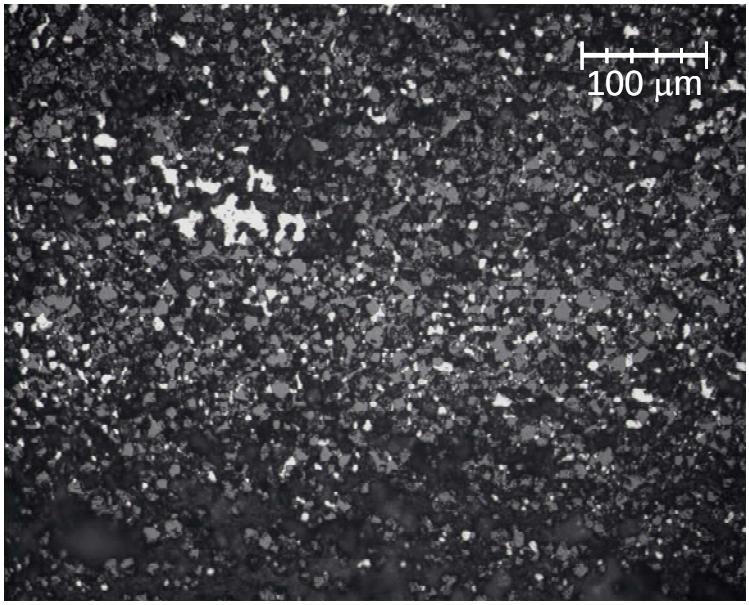

Fig. 7-20 Metallograph of the central region of the reduction product from Ca-6

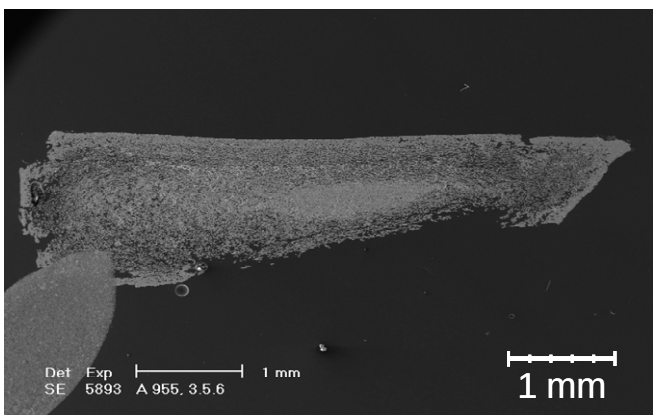

(a) Total section view

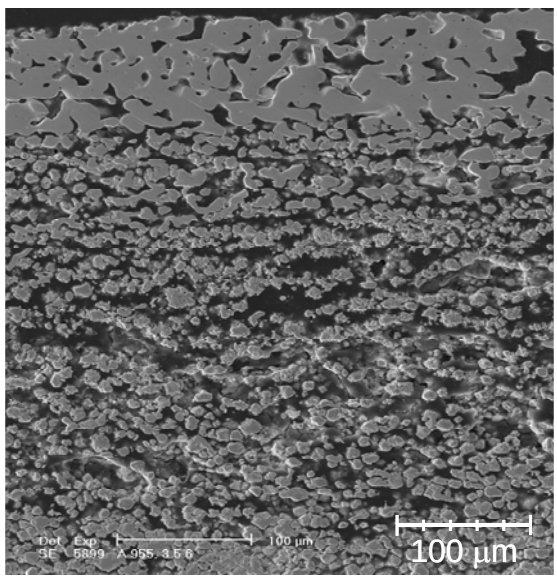

(b) Closer view of the near surface region

Fig. 7-21 SEM images of the reduction product from Ca-6

Chapter 8 Conclusions

The fundamental feasibility of the electrorefining and electroreduction processes, such as the recovery of the actinides at both the solid and liquid cadmium electrodes and conversion of UO_2 and MOX to metals, has been clarified. The basic electrochemical and thermodynamic data that govern the distribution equilibrium among the actinide and lanthanide elements in molten LiCl-KCl/liquid cadmium system have been obtained.

To establish the engineering and practical feasibility based on the technical and economical evaluation, however, it is needed to understand the quantitative relation between the operation conditions and the important performance such as processing rate, recovery rate and decontamination factors. In addition, it is necessary to predict the process performance in the electrorefining step by developing proper models in order to design the practical equipments and process flow sheet with satisfactory accuracy and reliability.

In this thesis, six studies were carried out to satisfy the above requirements. The results of these studies are summarized as follows.

In chapter 2, the diffusion coefficients of Ce(III) and Gd(III) in lithium chloride-potassium chloride eutectic melt were determined in the temperature range between 673 and 823 K by chronopotentiometry. In order to minimize the error in defining the surface area of the working electrode, the slope of the $\tau^{1/2}$-A plot was substituted into the Sand equation instead of their absolute values. The diffusion coefficients with the temperature dependence were :

$$\log D_{Ce} = -2.69\,(\pm 0.145) - \frac{1670\,(\pm 108)}{T} \qquad (D_{\mathrm{Ce}} : \mathrm{cm^2/s})$$

$$\log D_{Gd} = -2.78\,(\pm 0.128) - \frac{1670\,(\pm 94.3)}{T} \qquad (D_{\mathrm{Gd}} : \mathrm{cm^2/s})$$

The activation energies for diffusion and the diffusion coefficients of lanthanide ions in LiCl-KCl were discussed in connection with their ionic radii and stability of their complex ions.

In chapter 3, two kinds of electrochemical methods : (1) the electrotransport of uranium from a liquid cadmium layer, and (2) the electrochemical reduction of uranium from a molten salt electrolyte, were examined. Uranium was successfully recovered from both liquid cadmium and molten salt electrolyte. At a uranium

concentration lower than 0.1 wt%, recovery was difficult from either liquid cadmium or molten salt due to the polarization of the anode or contamination of the cathode product by rare earths. A diffusion layer model well explains the behavior of the electrotransport from the liquid cadmium anode. In electrochemical reduction from molten salt, direct chemical reduction occurred at the anode especially at a lower anode potential higher than the deposition potential of uranium.

In chapter 4, behavior of plutonium and americium at liquid cadmium cathode in molten LiCl-KCl electrolyte was studied.

Plutonium was collected into the no-stirred LCC without disturbance by solid phase formation at the surface. At plutonium concentration of 2.11 wt % in molten LiCl-KCl and cathodic current density of 41 mA/cm^2, the collection efficiency of plutonium was nearly 100 % and maximum plutonium loading into the LCC was 7.75 wt %. At the higher cathodic current densities, lithium metal was reduced and reacted with the ceramic LCC parts. The collection efficiency was decreased by $PuCd_6$ formation out of the LCC caused by those reactions.

The cathodic current density adequate for plutonium collection was proportional to the concentration of plutonium in the molten salt at the ratio of 22 mA/cm^2•wt %-Pu in the range of this study. At plutonium concentration of 5.0 wt % in molten salt, cathodic current density of 100 mA/cm^2 was attained without any trouble such as solid deposit growth or descent of cathode potential indicating reduction of lithium. The plutonium collection rate in a practical scale electrorefiner was estimated to be 324 grams per hour for one LCC based on the assumption that the collection rate is proportional to the plutonium concentration in the molten salt and the surface area of the LCC. This performance is considered high enough as an initial condition for design of the practical electrorefiner and pyrometallugical process.

It was considered that plutonium collected into the LCC after saturation formed intermetallic compound $PuCd_6$ and accumulated at the bottom of the LCC based on EPMA analysis of the LCC ingot.

In chapter 5, anodic behavior of U-Zr or U-Pu-Zr alloys during electrorefining in molten chloride electrolyte was modeled taking account of recent findings from the observation of anode residues after a number of electrorefining tests, such as formation of an intermediate region that has a composition corresponding to the δ phase.

Simulation of anodic dissolution of the U-Zr alloy during the engineering-scale electrorefining tests using the model showed that calculated

dissolution ratios of uranium and zirconium were in agreement with the experimental result when the alloy pin was chopped to as short as 5 mm assuming the progress of dissolution parallel to the exposed surface of the pins. Growth of the thick δ layer found in the anode residue sample was also explained by simulating the local anode behavior at lower anodic current density than the average value.

The laboratory-scale electrorefining tests with uncladded U-Pu-Zr ternary alloy were also simulated, and the characteristic change of anode potential during these tests was finely reproduced by fitting parameters for uranium activity in the porous zirconium layer.

Some exploratory calculations were conducted to investigate the effect of the current-controlling pattern and length of chopped alloy pins on the anodic dissolution rate and zirconium dissolution ratio. The results showed that the required period to attain a certain uranium dissolution ratio would be drastically increased with increase in pin length, and that the zirconium dissolved ratio would be largely increased when a higher anodic current density is applied to improve the electrorefining processing rate.

In chapter 6, applicability of square wave voltammetry (SWV) and normal pulse voltammetry (NPV) to on-line monitoring of actinide concentrations in molten LiCl-KCl was investigated using uranium, plutonium and neptunium for use in the pyrometallurgical processes.

For SWV of plutonium, the concentration dependence of the peak current was not linear at relatively high concentration, although SWV showed the advantage in high sensitivity and easy separation among the peaks in multi-component systems. The reduction currents for uranium and plutonium determined from the differentiated NPV data were proportional to their concentrations up to about 1.7 wt %. The fission product elements did not seem to affect the determined concentrations of uranium and plutonium because the reduction currents for these elements were not influenced by the addition of gadolinium which has the nearest standard electrode potential to those of the actinides among the fission product elements. It was found to be difficult to determine neptunium in the presence of plutonium due to the overlap of the output current waves. From those results, NPV was considered to be more promising for on-line monitoring in molten salt although the optimization of applied potential waveform would be necessary for use at the higher concentrations expected in the normal operation of the electrorefiner in the pyrometallurgical reprocessing.

In chapter 7, the electrochemical reduction of UO_2-PuO_2 mixed oxides (MOX)

was investigated in molten LiCl at 923 K and $CaCl_2$ at 1123 K to evaluate the behavior of the plutonium quantitatively and to define the favorable conditions for the electrochemical reduction of those materials.

In LiCl, it was found that the MOX was reduced at -0.65 V vs. Bi-35 mol % Li reference electrode by the CV measurement and the electrochemical reduction tests at constant cathode potential followed by SEM/EDX analysis. Under this condition, the reduced ratio evaluated both from the mass change between the reduction and by the gas-burette method was around 50 %. The cathodic current efficiency calculated from the reduced ratio was around 40 %.

In $CaCl_2$, on the other hand, the MOX was reduced in the whole range of the tested cathode potential (-0.15 V to -0.40 V), although the reduction was interrupted by formation of the surface barrier made of the reduced material at the lower cathode potential (-0.30 V). At –0.25 V, the MOX was completely reduced although the product was brittle probably due to the internal porosity formed by shrinkage of the reduced material. In the tests where the unbroken cathode products were recovered, the cathodic current efficiency was evaluated 40 - 50 %.

Dissolution of plutonium and americium into the electrolyte was found both in LiCl and in $CaCl_2$ electrolytes. The concentrations of these actinides at the end of the tests were higher in $CaCl_2$ than those found in LiCl electrolyte.

Taking the above experimental results and the compatibility with the pyrometallugical processes into consideration, LiCl was concluded to be more advantageous as the electrolyte used in the electrochemical reduction of MOX at present.

The relation among these activities and the operations in the electrorefining and electroreduction processes are shown in Fig. 8-1. Chapter 3 and chapter 4 give the information on the relation between the operation conditions and the performance of the uranium recovery with the solid cathode and the transuranium recovery with the liquid cadmium cathode, respectively. Chapter 5 provides the worthful tool for quantitative prediction of the influence of operation conditions of the anodic dissolution on its performance, based on the basic thermodynamic and kinetic properties of the major elements in the molten chloride/liquid cadmium system and also on the findings from the previous electrorefining experiments.

By contrast, chapter 2 contributes the improvement in the evaluation of the mass transfer rate in the total electrorefining process by establishing the reliable method for determination of the diffusion coefficients in the molten chloride. Chapter

6 offers the online monitoring method for the composition of the molten salt electrolyte, which makes the process control easier and bring out the best performance of the electrorefining step.

As shown in Fig. 8-1, the activities in this thesis exhaustively cover all the operations in the electrorefining step and constitute contribution to more quantitative understanding of the relation between the operation conditions and the performance of this process,

Concerning the electroreduction, the process development is at much earlier stage compared with the electrorefining. Then, quantification of the major process performance such as the reduced ratio and the current efficiency, and determination of the favorable electrochemical conditions for the complete reduction of the actinides are the most important issues to be clarified. Chapter 7 provides the fundamental information satisfying the above requirements through the parametric electroreduction experiments using U/Pu mixed oxides and various analytical methods.

From those results, the quantitative influences of the operation conditions, such as the electrode potential and the electrolyte composition, on the important performance of the electrorefining and electroreduction processes, like processing rate, recovery rate, decontamination factors and reduce ratio, have been made much clearer. Especially for the electrorefining process, quantitative analysis of behavior of the spent fuel anode has become possible by development of the multi-layer anode model. By using this model together with the previous diffusion layer model for the solid/liquid cathodes that was made before this thesis, the prediction of the performance in the electrorefining step will be conducted much easier and more accurate.

The results of this thesis, the understanding of the quantitative relation between the operation conditions and the electrorefining behavior, should be utilized in development of a computer code for analysis of electrorefining performance. This code will be significantly applied to the optimization of the operating conditions and the design of electrorefining equipments for practical use. To improve the precision in the calculation of anode behavior, remaining important subjects are exact estimation of the solubility of the actinides in molten salt electrolyte and the diffusion coefficients in the porous zirconium layer, observation of the irradiated fuels during anodic dissolution, and extension of the anode model to a three-dimensional system.

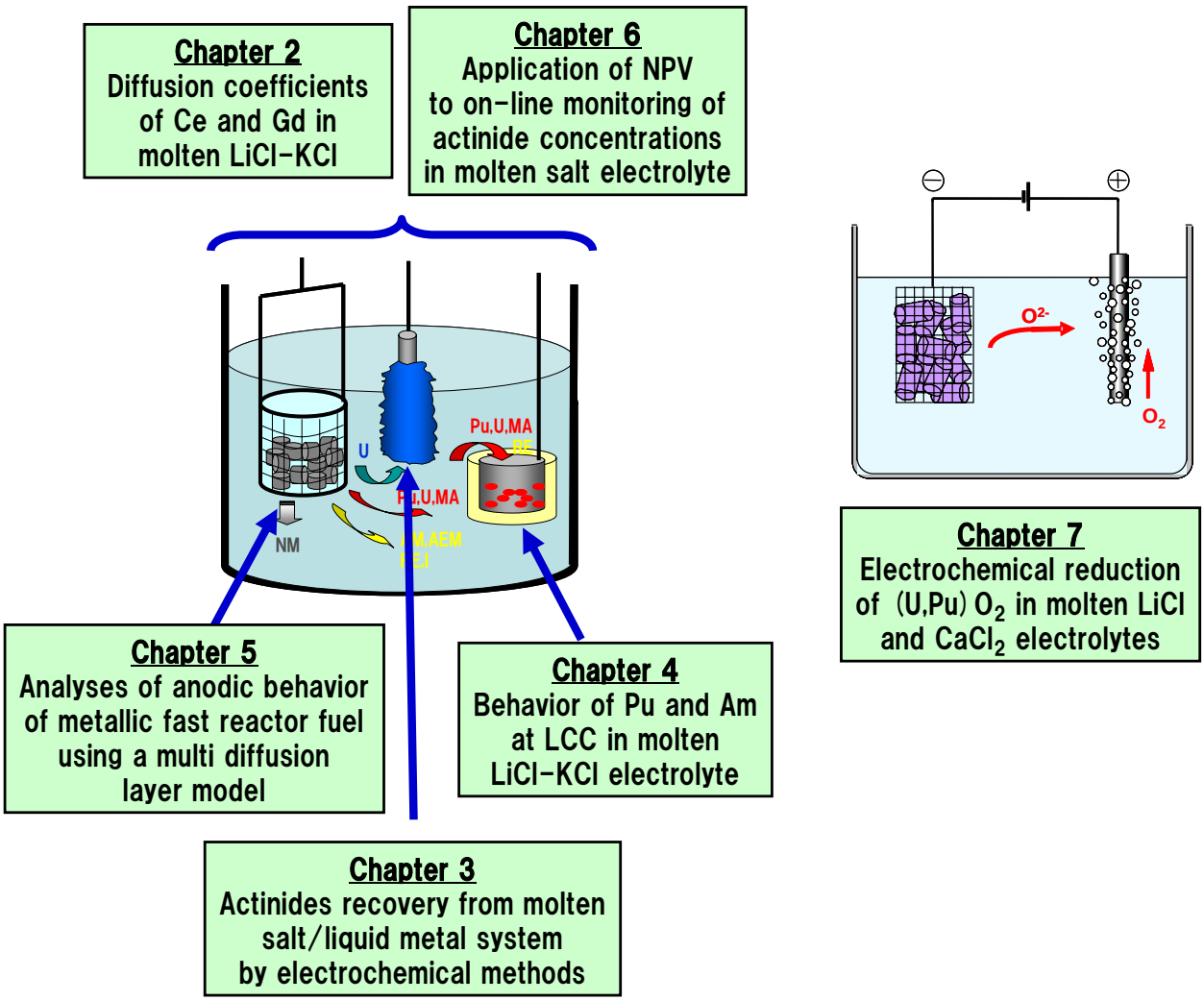

Fig. 8-1 Relation among the activities in this study and the operations in the electrorefining and electoreduction processes

Acknowledgement

First of all, I deeply appreciate Prof. Y. Ito of Doshisha Univ., who gave me suggestion and encouragement to take a degree, although over ten years have past thereafter.

I would like to thank Drs. M. Tokiwai, H. Tanaka, T. Inoue and T. Koyama of Central Research Institute of Electric Power Industry (CRIEPI) for their warm support to me for completion of this thesis.

I am grateful to Drs. Y. Suzuki, Y. Arai, O. Shirai and Mr. T. Iwai of Japan Atomic Energy Research Institute (JAERI, currently JAEA) for their comments and assists in the studies using transuraniums. I appreciate Drs. J.-P. Glatz, M. Murray-Farthing, T. Wiss, D. Cromboom and J. Somers of Institute of Transuranium Elements (ITU) for their support for the electroreduction experiments using MOX. I also like to express my thanks to Messrs. K. Shiozawa and T. Sasayama of JAERI, A. Rodorigues and M. Ougier of Institute of ITU, Mr. H. Nakamura of Toshiba Corporation for their experimental and analytical support.

Many thanks are due to my colleagues, Drs. T. Ogata, M. Kurata, T. Murakami and Messrs. Y. Sakamura, K. Kinoshita for the useful comments, discussions and their authentic expertise.

I would especially like to express my gratitude to Prof. H. Moriyama, who gave me the opportunity to write this thesis and also a lot of precious advice and encouragement. I also appreciate Prof. H. Yamana and Associate Prof. T. Sasaki for their suggestions to improve this thesis.

Finally, I would like to express special thank to my family, Chikako and Aya, who give me unlimited support and peace of mind at every moment I need it.

The experiments in chapter 3 were carried out under the joint program between the Toshiba Corporation and the Central Research Institute of Electric Power Industry (CRIEPI). The experiments in chapter 2 and 4 were carried out under the joint program "Fundamental study on molten salt electrorefining" between the Japan Atomic Energy Research Institute (JAERI) and CRIEPI. The experiments in chapter 7 were conducted under the joint research program between the Institute of Transuranium Elements (ITU) and CRIEPI.

Research activities by the author

Chapter 2

M. Iizuka, "Diffusion coefficients of cerium and gadlinium in molten LiCl-KCl", *J. Electrochem. Soc.*, **145**, 84-88 (1998).

Chapter 3

M. Iizuka, T. Koyama, N. Kondo, R. Fujita and H. Tanaka, "Actinides recovery from molten salt/liquid metal system by electrochemical methods", *J. Nucl. Mater.*, **247**, 183-190 (1997).

Chapter 4

M. Iizuka, K. Uozumi, T. Inoue, T. Iwai, O. Shirai and Y. Arai, "Behavior of plutonium and americium at liquid cadmium cathode in molten LiCl-KCl electrolyte", *J. Nucl. Mater.*, **299**, 32-42 (2001).

Chapter 5

M. Iizuka and H. Moriyama, "Analysis of anodic behavior of metallic fast reactor fuel using a multi diffusion layer model", *J. Nucl. Sci. Technol.*, *submitted*.

Chapter 6

M. Iizuka, T. Inoue, O. Shirai, T. Iwai and Y. Arai, "Application of normal pulse voltammetry to on-line monitoring of actinide concentrations in molten salt electrolyte", *J. Nucl. Mater.*, **297**, 43-51 (2001).

Chapter 7

M. Iizuka, T. Inoue, M. Ougier and J-P. Glatz, "Electrochemical reduction of $(U,Pu)O_2$ in molten LiCl and $CaCl_2$ electrolytes", *J. Nucl. Sci. Technol.*, **44**, 801-813 (2007).